

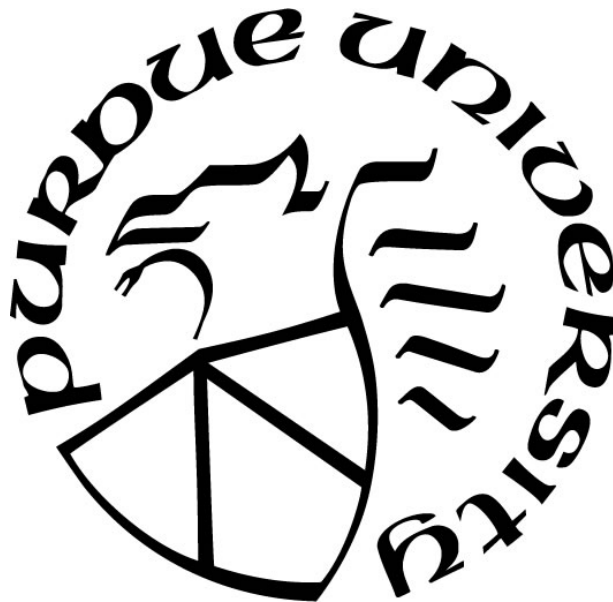
**MANGANESE-BASED THIN FILM CATHODES FOR ADVANCED
LITHIUM ION BATTERY**

by
Zhimin Qi

A Dissertation

*Submitted to the Faculty of Purdue University
In Partial Fulfillment of the Requirements for the degree of*

Doctor of Philosophy



School of Materials Engineering

West Lafayette, Indiana

December 2019

**THE PURDUE UNIVERSITY GRADUATE SCHOOL
STATEMENT OF COMMITTEE APPROVAL**

Dr. Haiyan Wang, Chair

Department of Materials Engineering

Dr. Xinghang Zhang

Department of Materials Engineering

Dr. R. Edwin García

Department of Materials Engineering

Dr. Kejie Zhao

Department of Mechanical Engineering

Approved by:

Dr. David Bahr

Head of the Graduate Program

This work is dedicated to my family's sacrifices and support.

ACKNOWLEDGMENTS

I would like to express my deepest thank to my research advisor, Dr. Haiyan Wang. Dr. Wang was always willing to help me to find the right research direction and provide insightful advices about conducting research during my Ph.D. period in her group. She is very passionate about research, which also inspire me to devote myself deeper into the world of science. Dr. Wang put significant effort in acquiring new research tools, which also gave me great experience on operating and maintaining various research equipment. Besides, she is also very knowledgeable in many cross-subject fields apart from materials science and engineering, which impressed and inspired me greatly. She treated her group members as a family, and she cares about our future. I'm honored to be able to work in her group. I really appreciate her help in both academic and personal life.

I would also like to thank my thesis committee members, Dr. R. Edwin García, Dr. Kejie Zhao, and Dr. Xinghang Zhang for their precious advice, great collaborations and help on my research. I really appreciate their willingness to be my thesis committee members and their valuable inputs on my prelim, data review and final defense.

I also want to thank all my colleagues in Dr. Haiyan Wang's Thin Film Functional Group, including the alumni (Dr. Clement Jacob, Dr. Meng Fan, Dr. Leigang Li, Dr. Jijie Huang) and the current members (Dr. Jie Jian, Dr. Han Wang, Dr. Xing Sun, Juncheng Liu, Xingyao Gao, Bruce Zhang, Xuejing Wang, Shikhar Misra, Zihao He, Matias Kalaswad, Robynne Paldi, Di Zhang, Xin Li Phuah, and Bethany Rutherford). I feel so grateful to have worked with so many great young researchers, who helped me a lot during my Ph.D. study.

I want to thank all my friends in the US, including Yuwei Zhang, Dr. Rong Xu, Dr. Jialiang Tang and many others, who also helped me a lot and gave me a wonderful life in the U.S.. Finally, I would like to thank my beloved family: my father and my mother. I could not have made through my Ph.D. study without their encouragement and support. I want to thank my dearest fiancé, Yaxuan Han, who supported me a lot throughout my entire Ph.D. study and I couldn't make this far without her support. I also felt very regret that I could not meet my grandparents the last time before they passed away during my Ph.D. study. They are greatly missed and are always the most important people in my life. I will do my best to live up to their legacies.

TABLE OF CONTENTS

LIST OF FIGURES	9
NOMENCLATURE	14
ABSTRACT.....	15
1. INTRODUCTION	17
1.1 Background.....	17
1.1.1 Preliminary consideration of materials selection of LIB system.....	19
1.1.2 Electrolyte for LIBs	20
1.1.2.1 Organic Liquid Electrolytes.....	20
1.1.2.2 Ionic Liquids.....	21
1.1.2.3 Solid Electrolyte	21
1.1.3 Electrodes for LIBs.....	21
1.1.4 Anode materials for LIBs	22
1.1.4.1 Graphite-intercalation mechanism.....	22
1.1.4.2 Silicon (Si)/ Tin (Sn)-Alloying mechanism.....	23
1.1.4.3 Metal oxides-conversion mechanism	23
1.1.5 Cathode materials for LIBs.....	24
1.1.5.1 Olivine	24
1.1.5.2 Spinel	26
1.1.5.3 Layered oxides.....	27
1.2 Thin film cathodes for lithium ion batteries	30
1.3 Briefs on modification approaches for thin film electrodes.....	32
1.4 Thin film electrodes modification.....	33
1.4.1 Nanostructure design (single phase).....	33
1.4.1.1 Nanostructure film growth (Bottom-up method).....	34
1.4.1.2 Hierarchical film growth on nanostructured substrates (Bottom-up method).....	40
1.4.1.3 Nanostructuring on planar electrode (Top-down method)	47
1.4.2 Nanocomposite design (two or more phases).....	51
1.4.2.1 Surface coating nanocomposite (Bottom-up method)	52
1.4.2.2 Co-grown nanocomposite (Bottom-up method).....	58
2. EXPERIMENTAL SECTION.....	63

2.1 Pulsed laser deposition (PLD)	63
2.2 Sputter	65
2.3 Microstructural characterization	66
2.3.1 X-ray Diffraction (XRD)	66
2.3.2 Scanning electron microscopy (SEM)	68
2.3.3 Transmission electron microscopy (TEM)	68
2.4 Cell assembly	71
2.5 Electrochemical characterization	72
2.5.1 Galvanostatic charging	72
2.5.2 Potentiostatic charging	73
2.5.3 Cyclic Voltammetry	73
2.5.4 Electrochemical impedance spectroscopy	73
2.5.5 Capacity	74
2.5.6 Power	74
2.5.7 Cycle life	74
2.5.8 Open circuit voltage (OCV)	75
3. $\text{LiNi}_{0.5}\text{Mn}_{0.3}\text{Co}_{0.2}\text{O}_2/\text{Au}$ NANOCOMPOSITE THIN FILM CATHODE WITH ENHANCED ELECTROCHEMICAL PROPERTIES	76
3.1 Overview	76
3.2 Introduction	76
3.3 Experimental	79
3.4 Results and Discussion	80
3.5 Conclusions	88
4. Li_2MnO_3 THIN FILMS WITH TILTED DOMAIN STRUCTURE AS CATHODE FOR LI- ION BATTERIES	89
4.1 Overview	89
4.2 Introduction	89
4.3 Experimental	92
4.4 Results and discussion	94
4.5 Conclusion	103

5. Li_2MnO_3 CATHODE THIN FILMS WITH TILTED AU NANOPILLARS AS EFFECTIVE CURRENT COLLECTORS FOR LI-ION BATTERY APPLICATION	104
5.1 Overview.....	104
5.2 Introduction.....	104
5.3 Experiments	106
5.4 Results and discussion	109
5.5 Conclusion	119
6. $\text{LiMn}_{0.5}\text{Ni}_{0.3}\text{Co}_{0.2}\text{O}_2$ THIN FILM CATHODE INTEGRATION ON NORMAL GLASS SLIDES BY PULSED LASER DEPOSITION	121
6.1 Overview.....	121
6.2 Introduction.....	121
6.3 Experimental.....	123
6.4 Results and discussion	124
6.5 Conclusion	129
7. Summary And Outlook.....	130
REFERENCES	134

LIST OF FIGURES

Figure 1.1 Ragone plot of (a) power density vs. power density of different energy storage methods [2] and (b) different types of batteries. [3]	17
Figure 1.2 Scheme of operation mechanism of lithium ion batteries. [12].....	18
Figure 1.3 Schematic energy plot of an aqueous electrolyte system. Φ_A and Φ_C are the work functions of anodes and cathodes. μ_A and μ_C are the electrochemical potential of anode and cathode. E_g is the energy gap of the electrolyte with thermodynamic stability. [13].....	20
Figure 1.4 Voltage vs. gravimetric capacity Ragone plot.....	22
Figure 1.5 Schematic representation showing that solvent molecules can attack ‘weak spot’ on graphite particle where there is no SEI protection and then cause crack. [30].....	23
Figure 1.6 Crystal structure of LiFePO_4 , obtained by using VESTA software.	25
Figure 1.7 Schemes indicating that (a) discontinuous, nonuniform carbon coating will introduce ‘dead point’ of electrons and (b) continuous, uniform carbon coating that will provide complete pathway of electrons. [40].....	25
Figure 1.8 Crystal structure of LiMn_2O_4 . [38].....	27
Figure 1.9 Crystal structure of LiCoO_2	28
Figure 1.10 Schematic representation of energy diagram vs density of states (DOS) for $\text{Li}_x(\text{Ni}_y\text{Mn}_z\text{Co}_{1-y-z})\text{O}_2$ when it is (a) completely discharged; (b) half charged; and (c) completely charged. [57]	29
Figure 1.11 Potential versus capacity plot of the mostly studied cathode materials using thin film techniques.	31
Figure 1.12 Flow chart of modification approaches for cathode electrodes using thin film techniques.	33
Figure 1.13 Schematic drawing of thin film modification approach that nanostructured thin film cathode is directly grown on planar substrates.	34
Figure 1.14 (a) Process of how the 3D porous multideck-cage structure is formed from 2D reticular structure with increased layers; (b) Rate performance of 3D porous multideck-cage structure at 8C, 16C, 24C, 32C,40C, 48C, and 56C; (c) Cycling performance for 200 cycles. ...	38
Figure 1.15 Schematic drawing of thin film modification approach that nanostructured thin film cathode is grown on pre-nanostructured substrates to achieve hierarchical nanostructured thin film cathodes.	40
Figure 1.16 (a) Schematic drawing of the finalized film microstructure; (b) SEM images of the film morphology before cycling; (c) SEM images of the film morphology after cycling for 30 cycles; (d) TEM micrograph of individual nanowire; (e) Cycling performance of nanostructured	

and planar LiMn_2O_4 thin films for 30 cycles; (f) Impedance versus frequency plot of the nanostructured and planar LiMn_2O_4 thin films after cycling.[61]	41
Figure 1.17 Schematic drawing of thin film modification approach that as-deposited thin film electrodes are nanostructured using laser technique.	47
Figure 1.18 SEM micrographs with different patterns of (a) holes, (b) line, (c) grating and (d) free-standing surface structures; (e) Cycling performance of LiMn_2O_4 thin films with different surface morphologies for 30 cycles at 0.5C.[128]	50
Figure 1.19 Schematic drawing of thin film modification approach of surface coating on planar or nanostructured thin film electrodes.	52
Figure 1.20 (a) Schematic drawing of the synthesis procedure of N-C@ VO_2 nanoflakes arrays; (b) Cyclic voltammetry of VO_2 nanoflakes arrays and N-C@ VO_2 nanoflakes arrays; (c) EIS measurements of VO_2 nanoflakes arrays and N-C@ VO_2 nanoflakes arrays; (d) Charge-discharge profile of VO_2 nanoflakes arrays and N-C@ VO_2 nanoflakes arrays at 0.2C; (e) Rate performance of VO_2 nanoflakes arrays and N-C@ VO_2 nanoflakes arrays at 0.2C, 1C, 3C, 10C, 15C, and 20C; (f) Cycling performance of VO_2 nanoflakes arrays and N-C@ VO_2 nanoflakes arrays for 500 cycles at 1C.[121].....	55
Figure 1.21 Schematic drawing of thin film modification approach that the secondary phase and matrix phase are co-deposited on substrates with different morphologies, where the two phases can be either mixed mechanically or treated using chemical method, and the morphology of the secondary phase can be tuned.	58
Figure 1.22 (a) Schematic drawing of composite NMC- Li_2MnO_3 thin film; (b) Schematic drawing of multilayered NMC- Li_2MnO_3 thin film; (c) TEM micrograph showing microstructure of composite NMC- Li_2MnO_3 thin film; (d) TEM micrograph showing microstructure of multilayered NMC- Li_2MnO_3 thin film; (e) Cycling performance of composite NMC- Li_2MnO_3 , multilayered NMC- Li_2MnO_3 , and pure NMC for 25 cycles; (f) Rate capability of composite NMC- Li_2MnO_3 , multilayered NMC- Li_2MnO_3 , and pure NMC.[163]	61
Figure 2.1 Schematic drawing of a general PLD system.[168]	63
Figure 2.2 Schematic drawing of three different thin film growth modes: (a) island mode, (b) layer-by-layer mode, and (c) mixed island-layer mode.	64
Figure 2.3 Laser-target interaction during formation of one pulse.[168]	65
Figure 2.4 Schematic drawing of a sputter system.[168].....	66
Figure 2.5 Schematic drawing showing fundamental mechanism of Bragg's law.....	67
Figure 2.6 Different types of signals can be generated from an incident electron beam.[169]....	68
Figure 2.7 Diagram of a common TEM system.[166].....	69
Figure 2.8 Two primary operation modes of TEM.[165]	71
Figure 3.1 Scheme proposing that Au added into the matrix of NMC exists in the form of particles.	78

Figure 3.2 X-ray diffraction of as-deposit film on (a) Au buffered Stainless Steel substrate with pole figure of NMC (0003) pole of (a1) Pure NMC, (a2) 2 at% Au added NMC and (a3) 6 at% Au added NMC; (b) *c*-cut Al₂O₃ substrate with different gold particle percentage introduced to the NMC matrix. 81

Figure 3.3 TEM images of 2 at. % Au NMC thin film on *c*-cut sapphire substrate: (a) low magnification plan-view and (a1) plan view SEM image of the film morphology; (b) low magnification cross-section showing the 3D nature of the Au nanoparticles being uniformly embedded into the NMC matrix and (b1) corresponding EDX mapping confirming the Au particles distribution; SAED pattern of NMC film from (c) Al₂O₃ [1120] and (d) Al₂O₃ [1010] zone axis..... 84

Figure 3.4 HAADF image of 2 at. % Au NMC film from (a) cross section of Al₂O₃ [1010] and (b) [1120] zone axis and (c) plan-view showing some Au substituted matrix region. 85

Figure 3.5 Electrochemical test of (a)(a1)(a2)(a3) cyclic voltammetry of different rate (20 μ V/s, 50 μ V/s, 75 μ V/s, 100 μ V/s and 200 μ V/s) for different Au concentration indicating addition of Au increase reversibility of the reaction by introducing extra peaks but excessive Au prevent redox reaction from occurring; (b)(b1)(b2)(b3) Cycling performance at 7.8 μ A/cm² for different Au concentration showing moderate amount of Au has the best cyclability; (c) Initial CV cycle of three samples with different Au concentration indicating that Au can alter the valence state of transition metal ions; (d) Rate measurement at current density of 7.8 μ A/cm², 15.6 μ A/cm², 39.0 μ A/cm², 78.0 μ A/cm², 117.2 μ A/cm² respectively showing better retention for 2 at% Au-NMC; (e) Nyquist plot of 2 at% Au-NMC and pure NMC at 3.7 V showing that addition of Au decreases the charge transfer resistance R_{ct} 87

Figure 4.1 Schematic drawing showing the different substrate growth configuration of conventional pulsed laser deposition and pulsed laser oblique angle deposition. 91

Figure 4.2 Out of plane X-ray profile of (a) oblique grow Li₂MnO₃ and (a1) (202) pole figure of Li₂MnO₃ on Al₂O₃ substrate; (b) non-tilt Li₂MnO₃ and (b1) (202) pole figure of Li₂MnO₃ on Al₂O₃ substrate, where comparison shows nearly identical crystallographic orientation of the different configuration. Out of plane X-ray profile of (c) oblique grow Li₂MnO₃ and (c1) SEM morphology scan of Li₂MnO₃ on Au-SS substrate; (d) non-tilt Li₂MnO₃ and (d1) SEM morphology scan of Li₂MnO₃ on Au-SS substrate, where it still exhibits same crystallographic orientation but largely different surface morphology. 94

Figure 4.3 Low magnification STEM images of (a) plan view perspective of and (b) cross sectional perspective of oblique grow Li₂MnO₃, the inset shows the corresponding SAED from Al₂O₃ [1010] zone axis. (c) high resolution TEM of pillar interface squared out in (b) and the cleavage plane is measured to be Li₂MnO₃ (131). (d) cross sectional perspective of non-tilt Li₂MnO₃ and the selected area diffraction pattern of non-tilt Li₂MnO₃ from Al₂O₃ [1010] zone axis is shown in the inset. 95

Figure 4.4 Cycling performance test of (a) oblique grow Li₂MnO₃ at 5 μ A/cm² for 100 cycles, the inset is the dQ/dV plot for the first three cycles; (b) non-tilt Li₂MnO₃ at 5 μ A/cm² for 3 cycles, the inset is the dQ/dV plot for the first three cycles. Cyclic voltammetry of (c) oblique grow Li₂MnO₃ with potential sweep rate of 20 μ V/s at 9th, 59th, and 79th cycles showing

homogenization through cycling; (d) non-tilt Li_2MnO_3 with potential sweep rate of $20 \mu\text{A/s}$ at 9^{th} exhibiting cathodic-type behavior on both sweep directions..... 97

Figure 4.5 (a) Cyclic voltammograms of oblique grow Li_2MnO_3 on different potential sweep rate of $10 \mu\text{V/s}$, $20 \mu\text{V/s}$, $50 \mu\text{V/s}$, $75 \mu\text{V/s}$, $100 \mu\text{V/s}$, and $200 \mu\text{V/s}$ with labeled major redox reactions “a”, “b”, “c”, and “d”; (b) C-rate performance test at current density of $5 \mu\text{A/cm}^2$, $10 \mu\text{A/cm}^2$, $20 \mu\text{A/cm}^2$, $40 \mu\text{A/cm}^2$, $80 \mu\text{A/cm}^2$ respectively with calculated columbic efficiency and estimated C-rate value; (c) fitted electrochemical impedance spectrum data of oblique grow Li_2MnO_3 with scheme indicating the equivalent circuit for the fitting..... 101

Figure 5.1 The schematic drawing of comparison between a) Li_2MnO_3 -Au particle and b) Li_2MnO_3 -Au pillar composite structures; and illustration of c) expected growth mechanism... 105

Figure 5.2 (a) Cross sectional TEM image of Li_2MnO_3 -Au composite on both Al_2O_3 substrate with (a1) HRTEM shows the d spacing of Au (111) and Li_2MnO_3 (001); (b) Plan-view TEM image indicates an aligned trend of the Au pillars inside Li_2MnO_3 ; (c) SAED pattern confirms the matching relationship Au and Li_2MnO_3 matrix from Al_2O_3 [1010] zone axis; (d)(d1)(d2) EDX mapping confirming the elemental distribution in the film. 109

Figure 5.3 (a) Cycling performance of Li_2MnO_3 -Au after 100 cycles; (b) Cyclic voltammograms of Li_2MnO_3 -Au with potential $20 \mu\text{V/s}$ sweep rate at 9^{th} , 59^{th} , and 79^{th} cycles; (c) C-rate performance test at current density of $5 \mu\text{A/cm}^2$, $10 \mu\text{A/cm}^2$, $20 \mu\text{A/cm}^2$, $40 \mu\text{A/cm}^2$, $80 \mu\text{A/cm}^2$ respectively with calculated columbic efficiency, and the corresponding estimated C-rate values are also labeled; (d) EIS measurement of the cell after cycling. 112

Figure 5.4 Psi obtained by ellipsometer at 50° , 60° and 70° with fitted data of (a) pure Li_2MnO_3 and (b) Li_2MnO_3 -Au pillars composite film; (c) Permittivity data measured through ellipsometer indicating the increased absorption of Li_2MnO_3 -Au and introduced anisotropy; (d) Tauc plot obtained through transmission measurement deciding the bandgap of Li_2MnO_3 and Li_2MnO_3 -Au pillar. 116

Figure 5.5 (a) Illustration of growth setup at higher tilt angle α_1 ; (b) thin film grown with thicker film and smaller tilt angle β_1 ; (c) HRSTEM showing Au pillar with small width; (d) illustration of growth setup at higher tilt angle α_2 ; (e) thin film grown with thinner film and larger tilt angle β_2 ; (f) HRSTEM showing Au pillar with increased width; (g) Permittivity curve of Li_2MnO_3 at higher tilt angle α_1 ; (h) permittivity curve of Li_2MnO_3 at t lower tilt angle α_2 118

Figure 6.1 Schematic drawing of the stack of cathode and current collector on glass substrates. 122

Figure 6.2 Scheme and photo for the two-electrode setup for electrochemical measurements.. 123

Figure 6.3 (a) Low-magnification SEM micrograph of as-deposited NMC/AZO/glass thin films; (b) high-magnification SEM micrograph of as-deposited NMC/AZO/glass thin films. 124

Figure 6.4 (a) Out-of-plane XRD pattern of as-deposited NMC/AZO/glass thin films and cycled NMC/AZO/glass thin films; (b) pole figure NMC(0003), (c) pole figure NMC(1014), (d) pole figure AZO(0002), and (e) pole figure AZO(1014) of as-deposited thin films. 125

Figure 6.5 (a) Charge-discharge curve of the first cycle of NMC/AZO/glass with inset showing the dQ/dV plot of that; (b) five consecutive CV cycles of NMC/AZO/glass thin films at potential

sweep rate of 50 $\mu\text{V/s}$; (c) cycling behavior of NMC/AZO/glass thin films for 10 cycles; (d) CV measurements of NMC/AZO/glass after cycles at different sweep rate of 20 $\mu\text{V/s}$, 50 $\mu\text{V/s}$, 75 $\mu\text{V/s}$, 100 $\mu\text{V/s}$, 200 $\mu\text{V/s}$, and 400 $\mu\text{V/s}$ 127

Figure 6.6 (a) pole figure NMC(0003), (b) pole figure NMC(1014), (c) pole figure AZO(0002), and (d) pole figure AZO(1014) of as-deposited thin films; (e) low-magnification SEM micrograph of cycled NMC/AZO/glass thin films; (f) high-magnification SEM micrograph of cycled NMC/AZO/glass thin films. 128

Figure 7.1 Peukert plot of representative thin film cathode electrodes modified with approach A1,A2,B,C1, and C2. 132

NOMENCLATURE

PLD	Pulsed Laser Deposition
PVD	Physical Vapor Deposition
SEM	Scanning Electron Microscopy
TEM	Transmission Electron Microscopy
HRTEM	High Resolution Transmission Electron Microscopy
STEM	Scanning Transmission Electron Microscopy
XRD	X-ray Diffraction
SAED	Selected Area Electron Diffraction
EDX	Energy Dispersive X-ray spectroscopy
ADF	Annular Dark-field Imaging
EELS	Electron Energy Loss Spectroscopy
FWHM	Full Width Half Maximum
FFT	Fast Fourier Transformation
HADDF	High Angle Annular Dark Field Imaging
CV	Cyclic Voltammetry

ABSTRACT

Author: Qi, Zhimin. PhD

Institution: Purdue University

Degree Received: December 2019

Title: Manganese-Based Thin Film Cathodes for Advanced Lithium Ion Battery

Committee Chair: Haiyan Wang

Lithium ion batteries have been regarded as one of the most promising and intriguing energy storage devices in modern society since 1990s. A lithium ion battery contains three main components, cathode, anode, and electrolyte, and the performance of battery depends on each component and the compatibility between them. Electrolyte acts as a lithium ions conduction medium and two electrodes contribute mainly to the electrochemical performance. Generally, cathode is the limiting factor in terms of capacity and cell potential, which attracts significant research interests in this field. Different from conventional slurry thick film cathodes with additional electrochemically inactive additives, binder-free thin film cathode has become a promising candidate for advanced high-performance lithium ion batteries towards applications such as all-solid-state battery, portable electronics, and microelectronics. However, these electrodes generally require modifications to improve the performance due to intrinsically slow kinetics of cathode materials.

In this thesis work, pulsed laser deposition has been applied to design thin film cathode electrodes with advanced nanostructures and improved electrochemical performance. Both single-phase nanostructure designs and multi-phase nanocomposite designs are explored. In terms of materials, the thesis focuses on manganese based layered oxides because of their high electrochemical performance. In Chapter 3 of the nanocomposite cathode work, well dispersed Au nanoparticles were introduced into highly textured $\text{LiNi}_{0.5}\text{Mn}_{0.3}\text{Co}_{0.2}\text{O}_2$ (NMC532) matrix to

act as localized current collectors and decrease the charge transfer resistance. To further develop this design, in Chapter 4, tilted Au pillars were incorporated into Li_2MnO_3 with more effective conductive Au distribution using simple one-step oblique angle pulsed laser deposition. In Chapter 5, the same methodology was also applied to grow 3D Li_2MnO_3 with tilted and isolated columnar morphology, which largely increase the lithium ion intercalation and the resulted rate capability. Finally, in Chapter 6, direct cathode integration of NMC532 was attempted on glass substrates for potential industrial applications.

1. INTRODUCTION

1.1 Background

Energy consumption has been relying on fossil fuels for thousand years, which is having a severe impact on world economics and ecology. Thus, searching for a new alternative energy source that is environment friendly and of high sustainability, is of great importance. With years of dedication in research of energy storage devices, three main types of energy storage methods, namely, fuel cells, batteries, capacitors, enjoy the most attention from scientists around the world. Though the performance of these methods fits in different applications, batteries are still the most interested method owing to the combined high energy density and power density compared to the other two.[1]

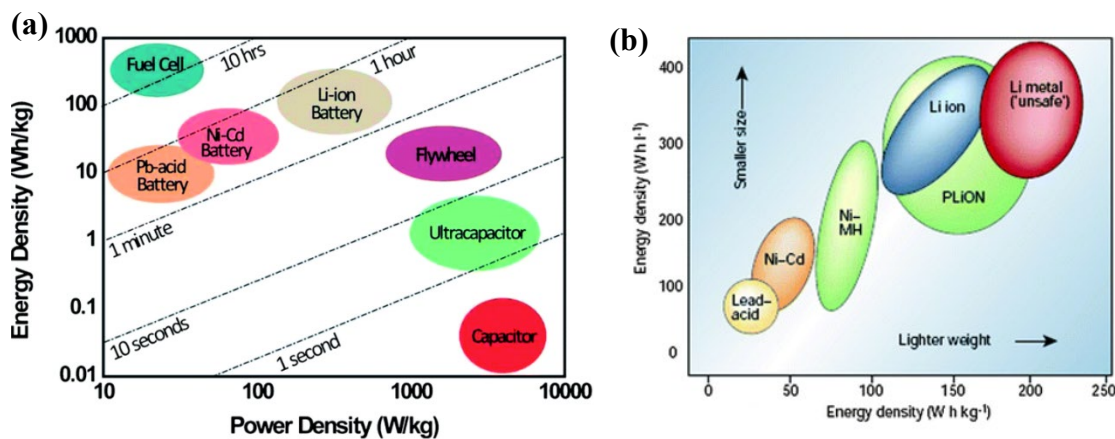


Figure 1.1 Ragone plot of (a) power density vs. power density of different energy storage methods [2] and (b) different types of batteries. [3]

Among all battery technologies, lithium batteries are one of the most successful energy storage method in current society due to the fact that, especially when compared to conventional lead/cadmium based batteries, lithium is the lightest element, environmentally friendly, and also the most electropositive element, which means lighter batteries with very high capacity.[4]–[6]

Even though lithium batteries have been commercialized since 1970s and great effort has been devoted by researchers to build better lithium batteries, it still experiences safety issue and instability caused by dendrite growth and heat generation.[7]–[9] Thus, later effort has been made to develop batteries with lithium ions as the source.[10], [11]

Lithium ion batteries (LIB) are promising because of their high voltage, high power densities, high energy densities, and stable cycling performance. The goal of the research community is to develop a low-cost, safe, rechargeable battery with high voltage, capacity, great rate capability, and long cycle life. A general LIB consists of cathode current collector, cathode material, porous separator, anode material, anode current collector and electrolyte. The basic operation mechanism is shown in Figure 1.2. Lithium ion is stored in the interstitial sites of host materials, and they will be extracted from the cathode side upon charging, passing through the separator through electrolyte and inserted into the anode side. The discharge process acts reversely on lithium ions. The performance of lithium ion batteries is thus affected by cathode, anode, electrolyte and separator.

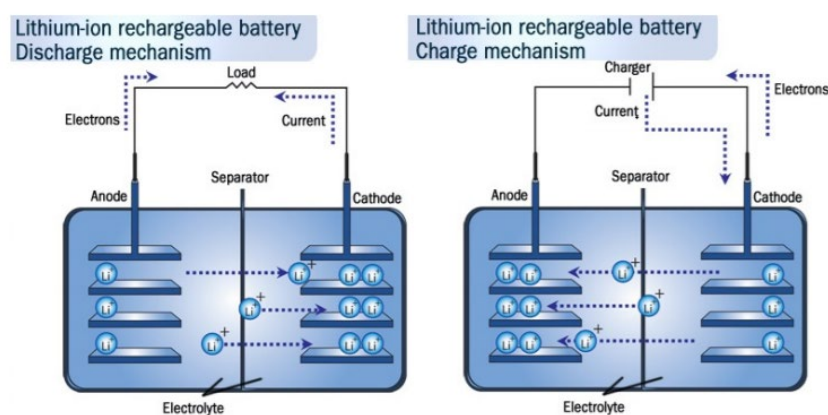


Figure 1.2 Scheme of operation mechanism of lithium ion batteries. [12]

In this section, the materials selections for LIB are reviewed for electrolyte, anode and cathode with the focus on various cathode materials.

1.1.1 Pre-consideration of materials selection for LIB system

To design a working battery system, certain requirements must be met regarding selection of cathode, anode, and electrolyte. The primary selection rule is shown schematically in Figure 1.3, which can be summarized as that the electrochemical potential of cathode and anode should fall between Highest Occupied Molecular Orbital (HOMO) and Lowest Unoccupied Molecular Orbital (LUMO) window. Precisely, if the electrochemical potential of cathode is lower than the HOMO level, electron will move from electrolyte to cathode because cathode can provide available energy state lower than HOMO under this situation. In other word, the electrolyte will be oxidized. Similarly, electrolyte will be reduced when the electrochemical potential of anode is higher than the LUMO level.[6], [13] This phenomenon is not favorable because the electrolyte is expected be stable during the cycling process.[6] On the other hand, an oxidation/reduction passivation layer will form on the electrodes when redox reaction occurs at the electrolyte/electrode interface, which is usually called solid electrolyte interphase (SEI).[14] SEI layer on anode will bring up the LUMO energy level and that on cathode will decrease the HOMO energy level until the electrochemical potential of cathode and anode fall in the LUMO-HOMO window and no further redox reaction will happen. This interphase layer will impact heavily on the electrochemical performance of the battery and will be explained in the following section.

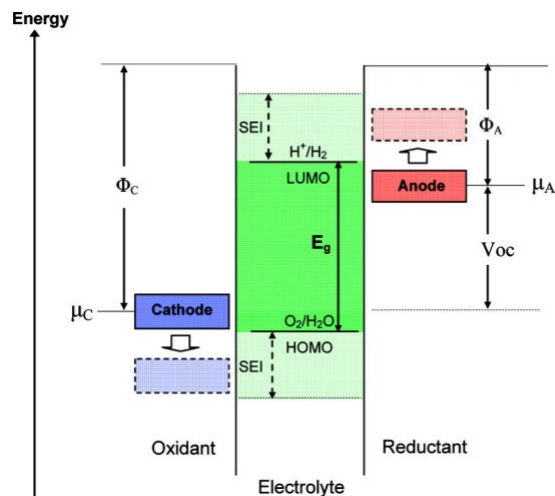


Figure 1.3 Schematic energy plot of an aqueous electrolyte system. Φ_A and Φ_C are the work functions of anodes and cathodes. μ_A and μ_C are the electrochemical potential of anode and cathode. E_g is the energy gap of the electrolyte with thermodynamic stability. [13]

1.1.2 Electrolyte for LIBs

Various types of electrolytes have been studied over the years, where aqueous based solvents can't be applied because they will electrolyze under the operation voltage of a normal LIB system.[14] Choices of electrolyte varies on applications as well as the electrolyte/electrode compatibility.[13] For example, the chemical reaction between electrolyte and electrodes could possibly cause electrode dissolution,[15] cycling of electrolyte material.[16] Besides, the passivation layer formed on electrode surface due to small electrochemical window of electrolyte cause detrimental effect including such as Li plating.

1.1.2.1 Organic Liquid Electrolytes

Most organic liquid electrolyte use carbonates or carbonates blends. Among different types of lithium salts, LiPF_6 is considered as the most balanced salt that is commonly used in combination

with selected organic solvents. However, it still experience bad thermal stability and intolerant to moisture.[17]–[19]

1.1.2.2 Ionic Liquids

Room Temperature Ionic Liquids (RTILs) show excellent performance as electrolyte for LIB system usually with low melting temperature smaller than 100 °C. [6], [13], [20]–[23] However, most ILs can only be compatible and applied to specific electrode material system.

1.1.2.3 Solid Electrolyte

Solid electrolytes mainly include solid polymer electrolytes and inorganic solid electrolytes. Solid polymer electrolyte has advantages in sustaining intact electrode/electrolyte interface upon cycling. However, the conductivity is too low to be promising. Inorganic solid electrolyte, on the other hand, is usually conductive ceramics or glasses[24] with high ionic conductivity but suffers interface delamination in the meantime.[25], [26]

1.1.3 Electrodes for LIBs

Both anode and cathode, work as host of lithium ions, shown in Figure 1.2, lithium ions will be reversibly inserted to and extracted from cathode and anode, thus some pre-consideration can be made about the requirement of a successful electrode material: 1) The electrode materials should hold as many lithium ions as possible per unit volume and weight, thus it will provide high volumetric capacity or specific capacity. 2) The structure of the electrode materials should be stable upon cycling, e.g. no fatigue, collapse, crack, delamination, etc. 3) The electrode should provide both good electric and ionic conductivity so that it could be operated under high current density and gives high power capability. 4) Electrochemical potential μ_A and μ_C of electrodes

should fall inside the LUMO-HOMO window gap of electrolyte, or the passivation layer formed due to electrolyte decomposition should be chemically, thermally, and mechanically stable. 5) Different between μ_A and μ_c should be large so that big operation potential and energy density can be obtained for the battery. Figure 2.1 shows the voltage vs. gravimetric capacity of cathode and anode materials, which clearly shows us that cathode materials are the limiting factors in terms of both voltage and specific capacity.

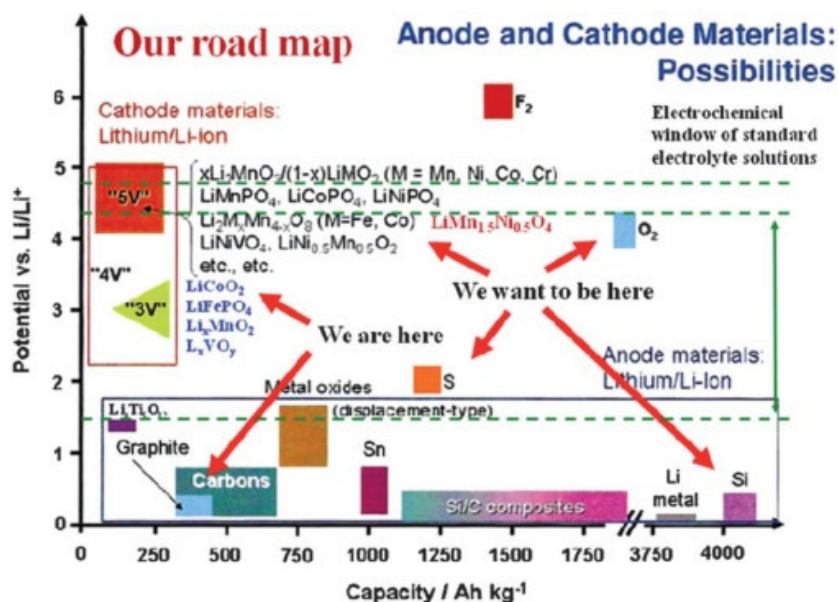
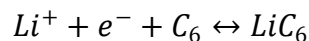


Figure 1.4 Voltage vs. gravimetric capacity Ragone plot.

1.1.4 Anode materials for LIBs

1.1.4.1 Graphite-intercalation mechanism

Graphite is one of the most successful commercialized anode materials in the market. Graphite has advantage of high capacity, low voltage (vs. Li^+/Li^0) and cost, it has a theoretical capacity 372 mAh/g and its reaction with lithium ions is shown below:



However, graphite is mechanically weak. Exfoliation and cracking can be caused by insertion and reduction of solvent molecules into graphite. Figure 2.2 demonstrates that mechanical failure can occur in graphite particles where no passivation layer is formed.[27]–[29]

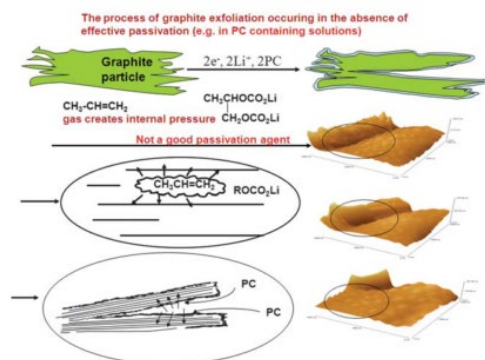


Figure 1.5 Schematic representation showing that solvent molecules can attack ‘weak spot’ on graphite particle where there is no SEI protection and then cause crack. [30]

1.1.4.2 Silicon (Si)/ Tin (Sn)-Alloying mechanism

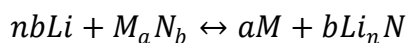
The chemistry of both Si and Sn anode with lithium ions can be expressed as below:[30], [31]



Si has a very high theoretical capacity of 3579 mAh/g. Nonetheless, it suffers from significant volume change accompanying lithiation as well as low lithium diffusivity. To solve this issue, dimension reduction techniques are usually applied. Sn, on the other hand, has lower theoretical capacity of 990 mAh/g but higher atomic mobility than Si, rendering higher lithium diffusivity. Therefore, Sn-Si composites are usually considered as better options.

1.1.4.3 Metal oxides-conversion mechanism

The chemistry of a general conversion anode could be expressed as:[32]



These materials have high versatility but suffer high polarization and high overpotential because most of the type are metal oxides, which can cause irreversibly capacity. [33] Though reducing the dimension to nanoscale and introducing conductive additives can help reduce the polarization, the intrinsic issue from the materials properties can't be completely solved.

1.1.5 Cathode materials for LIBs

It is indicated in Figure 1.4 that the limiting factor of performance in modern LIBs market is the cathode material. Effort has been made to develop various types of cathode materials since 1980s and all the mainstreamed cathode materials are of intercalation type of materials, which can be further classified into three types in terms of crystal structure and lithium diffusion dimension, i.e. olivine types of LiMPO_4 (where $M = \text{Fe, Mn, etc.}$) with one dimension of lithium diffusion path, layered transition metal oxides (LiMO_2 , where $M = \text{Co, Mn, Ni}$) with two dimensions lithium diffusion path, and spinel structure of LiMn_2O_4 with three dimensions lithium diffusion path.[34] Though there are cathode materials which belong to different reaction mechanism other than intercalation, e.g. conversion reaction, the voltage for these materials is usually very low.

1.1.5.1 Olivine

LiFePO_4 is the first material of olivine phase that was discovered by Padhi *et al.* in 1997,[35] it has a theoretical capacity of 170 mAh/g, a typical redox reaction occurring around 3.4 V, and no major capacity fade for more than several hundred cycles.[36] It is also environmentally friendly, inexpensive and non-toxic. The crystal structure is illustrated in Figure 1.6, where lithium ion situates in the channel formed by edge-sharing LiO_6 octahedra along the *b*-axis. This material experiences intrinsic low electrical conductivity ($\sigma_e < 10^{-9}$ S/cm) and low lithium ion diffusivity

($D \approx 10^{-14} \text{ cm}^2/\text{s}$) due to one dimension diffusion nature,[37] which means the theoretical capacity can only be achieved under very low current density. Therefore, composite of LiFePO_4 with conductive additives such as carbon is usually used to increase electrical conductivity.[38], [39] As it is shown in Figure 1.7, carbon coating on LiFePO_4 is proved to successfully improved the rate capability of the material. In addition, high quality and uniform coating of carbon can further improve the cathode performance. As for lithium ion diffusivity, the reduction of cathode material dimension is proved to be effective due to shorter Li^+ diffusion paths.[40], [41] It is also suggested that carbon coating may also contribute to the decrease of Li^+ diffusion paths because the pyrolytic carbon will suppress particle growth and lead to fine particles.[42]

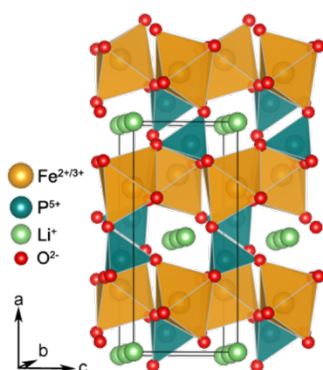


Figure 1.6 Crystal structure of LiFePO_4 , obtained by using VESTA software.

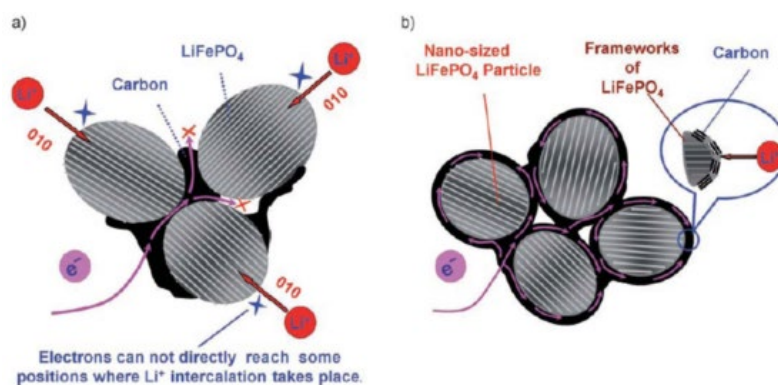


Figure 1.7 Schemes indicating that (a) discontinuous, nonuniform carbon coating will introduce ‘dead point’ of electrons and (b) continuous, uniform carbon coating that will provide complete pathway of electrons. [40]

1.1.5.2 Spinel

Spinel cathode, typically LiMn_2O_4 , has a theoretical capacity of 148 mAh/g. It was first proposed by Thackeray *et al.* in 1983.[43] LiMn_2O_4 has many advantages as a cathode material such as very cheap and abundant Manganese element. It has a $\text{A[B]}_2\text{O}_4$ spinel type cubic structure with space group as $Fd3m$, and Mn ions form a three-dimensional framework of MnO_6 octahedra where Mn ions take place half of the octahedral interstitial sites. Further, lithium ions sit at tetrahedral sites. LiMn_2O_4 has two redox pairs at 4 V and 3V, where the 3V region is usually avoided because the lithium insertion at this stage will cause the onset of phase transformation to rock salt $\text{Li}_2\text{Mn}_2\text{O}_4$, which subsequently introduces Mn^{3+} . This ion can introduce Jahn-Teller effect, which not only reduces the crystal symmetry to tetragonal but also induces large volume change that causes structural failure. Dissolution of Mn ions, especially with commonly used liquid organic solvent with LiPF_6 salt, could occur due to the disproportionation of surface Mn^{3+} ions:



This issue can be resolved by protective coating layers such as Al_2O_3 ,[44] MgO ,[45] AlF_3 ,[46] etc. In addition, capacity fade could happen at the 4V plateau as well, the mechanism however seems unsettled, possible explanations such as Mn dissolution,[47] multiphases coexisting in high voltage region,[48] effect of Jahn-Teller distortion around 3V,[49], [50] accumulation of lithium ions at particle surfaces,[51] have all been reported. Dopant such as Co is used to decrease the amount of Mn^{3+} ,[52] and surface coating for restraining particles[53] are both reported potential solutions but they also exhibit side effects such as capacity decrease

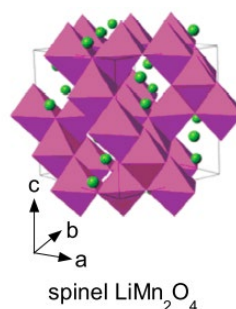


Figure 1.8 Crystal structure of LiMn_2O_4 . [38]

1.1.5.3 Layered oxides

In 1980, LiCoO_2 was first recognized as a cathode material with high energy density by Goodenough.[54] It has a theoretical capacity of 272 mAh/g and a layered $\alpha\text{-NaFeO}_2$ structure where Co and Li ions occupy the octahedral sites in alternating layers formed by oxygen close-packed planes (O3 stacking), which forms lithium layers sandwiched in between MO_6 layers, providing lithium ions the two dimensional diffusivity, as it is shown in Figure 1.10. LiCoO_2 mainly suffers from 1) Jahn-Teller effect during discharge when x in Li_xCoO_2 is smaller than 0.5, which leads to charge delocalization of Co ions. It will cause phase transformation to monoclinic crystal structure and partial oxidation of O^{2-} ; 2) Dissolution of Co ions which leads to formation of oxygen and cause safety issues, especially at high temperature.[37] Another similar material, LiNiO_2 , barely raises interests among researchers due to difficult synthesis of highly ordered layered structure and its instability upon cycling. However, $\text{LiNi}_{1-y}\text{Co}_y\text{O}_2$, overcomes main issues that bother both LiCoO_2 and LiNiO_2 . It is proved that addition of Co will impede Ni ions from migrating into the lithium layer and avoid permanent capacity loss.[36] However, the cost of the battery increases quickly as more Co is added into $\text{LiNi}_{1-y}\text{Co}_y\text{O}_2$. Therefore, it is natural to find the step substituting Ni, Co with other ions that are inexpensive and can contribute to the performance in the meantime.

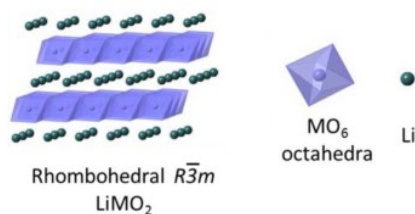


Figure 1.9 Crystal structure of LiCoO₂.

Among all other mixing cation oxides, Li(Ni_yMn_zCo_{1-y-z})O₂ (NMC) was first proposed by Liu *et al.* in 1999.[55] It has similar crystal structure and theoretical capacity as LiCoO₂, but it provides better thermal stability, higher redox voltage, and higher reversible capacity. In this composition, Co³⁺ ions function as reduction of cation mixing of Ni²⁺ ions in the lithium layer as well as electrochemically active element in high voltage region, Ni²⁺ ions enhance the layer properties as well as provides electrochemically activity in low voltage region, and Mn⁴⁺ ions are mainly used to reduce the cost of the material.[36] Energy vs. DOS is shown in Figure 1.11, which indicates 1) Large conductivity variation during charge and discharge 2) intrinsic voltage limit for this material.[13] Apart from these, NMC also experience low conductivity and ionic diffusivity that exhibits an unsatisfactory rate capability, which can be solved by reducing the dimension of material.[56]

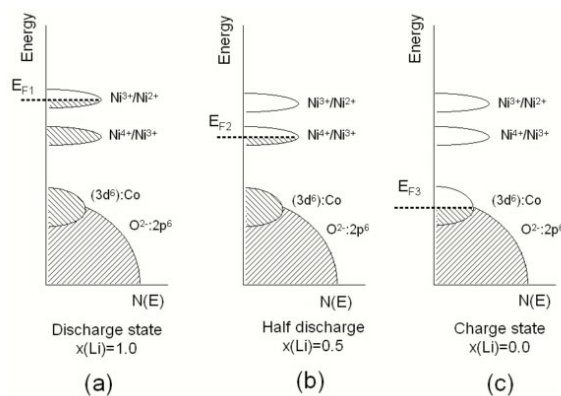


Figure 1.10 Schematic representation of energy diagram vs density of states (DOS) for $\text{Li}_x(\text{Ni}_y\text{Mn}_z\text{Co}_{1-y-z})\text{O}_2$ when it is (a) completely discharged; (b) half charged; and (c) completely charged. [57]

Later, Thackeray proposed a composite cathode material of layered NMC and layered Li_2MnO_3 , which can be generally expressed as $x\text{Li}_2\text{MnO}_3 \cdot (1-x)\text{Li}(\text{Ni}_y\text{Mn}_z\text{Co}_{1-y-z})\text{O}_2$, also called Li-rich cathodes. It has a high capacity larger than 300 mAh/g (voltage window 2.0V – 4.8V), good capacity retention, and good thermal stability. Li_2MnO_3 serves in this composite as a structure stabilizer because it is generally not electrochemically active. Its structure remains on debate whether NMC and Li_2MnO_3 form a solid solution with Li and Mn forming an alternative ordering manner[57] or those two phases form local domains that only retain short-range order[58]. Despite the excellent capacity, it also has three major concerns: 1) large initial capacity loss due to removal of Li_2O at the end of first charge cycle; 2) energy fade due to voltage/capacity fade caused by phase transformation during cycling; 3) low conductivity due to the highly insulating Li_2MnO_3 . Similar to spinel LiMn_2O_4 and olivine LiFePO_4 , protective coating layer and conductive carbon layer are proposed to prevent side reaction and increase conductivity, reduction of material dimension can also compensate the low conductivity of Li_2MnO_3 , doping can tailor the chemistry of material, and composite method can combine the advantages of different phases.[34]

1.2 Thin film cathodes for lithium ion batteries

The previous sections have introduced the different types of cathode materials, and extensive research has been performed to them in slurry electrodes form, which contain inactive materials that decreases the energy density of the cells. To overcome the issues brought by the inactive materials in the cathodes, binder-free thin film cathodes emerged, reported by Bates *et al.* in 1993 using RF magnetron sputtering.[59] This approach can eliminate the weight of inactive materials, which effectively increase the energy loading in the cell. Furthermore, the binder-free cathodes can avoid the usage of toxic solvent N-Methyl-2-pyrrolidone (NMP) during the electrodes processing. In terms of the cathode film thickness, it has been reported generally between several nanometers to a few micrometers for thin film cathodes in order to decrease the charge diffusion length, which makes the pristine cathode materials functional even without conductive additives and enables high power applications. Thin film cathodes can also be easily adopted for all-solid-state batteries where no flammable liquid electrolyte is used, and enables dedicated applications such as implanted medical devices, flexible and portable electronics, smart cards, etc. Additionally, thin film cathodes also take advantages that they are free of inactive additives and can be designed to achieve different microstructures or crystalline structures by various thin film techniques, and are easier to explore than slurry cathodes.[60]

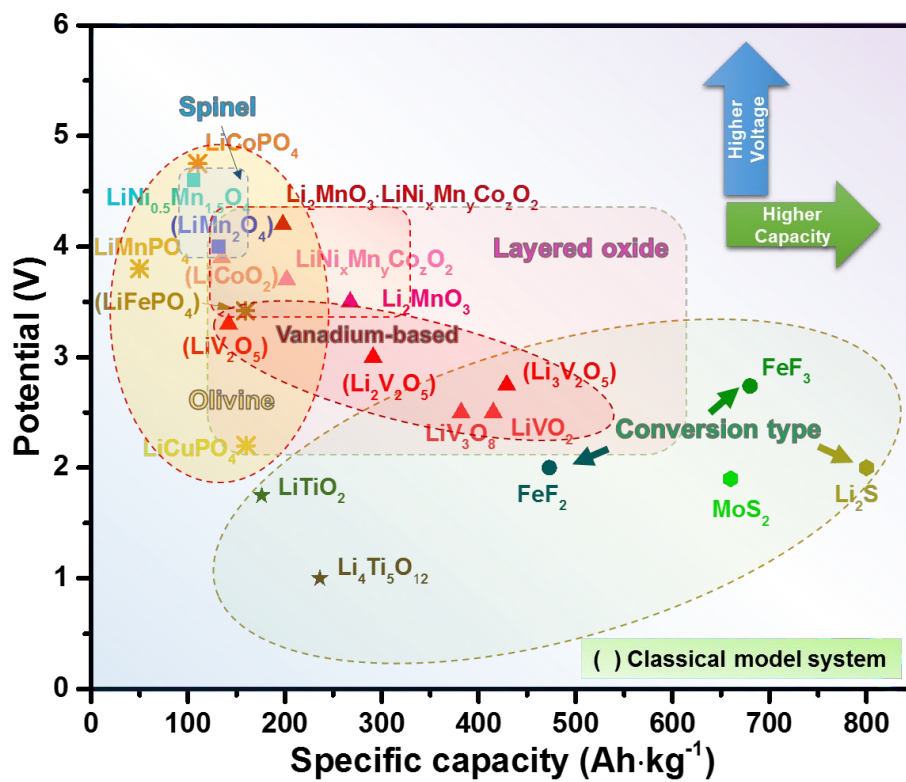


Figure 1.11 Potential versus capacity plot of the mostly studied cathode materials using thin film techniques.

The potential versus specific capacity plot in Figure 1.12 summarizes the reported thin film cathode materials up-to-date. As shown, most of the studied systems are model cathodes from different structure classes (i.e., olivine-LiFePO₄, layered-LiCoO₂/V₂O₅, and spinel-LiMn₂O₄). It's worth noting that several low potential materials are also plotted and are considered as cathode materials due to their applications in certain 2V batteries. In addition, layered oxides should be the more suitable choices for ideal cathode materials as they have higher voltage and higher specific capacity.[37] In the following sections, introduce several representative examples

using different modification methods to demonstrate the thin film modification approaches and progress.

1.3 Overview on modification approaches for thin film electrodes

Thin film cathode modification techniques can be categorized into two major groups, i.e., single-phase nanostructured cathodes and multi-phase nanocomposites cathodes. The principal thin film techniques to achieve the abovementioned modifications include but are not limited to: sol-gel method,[61], [62] hydrothermal synthesis,[63] co-precipitation,[64] template-assisted synthesis,[65] electrostatic spray deposition (EDS),[66] atomic layer deposition,[67] laser processing,[68] chemical vapor deposition,[69] physical vapor deposition,[70] plasma-assisted synthesis,[71] etc. The detailed methodologies, shown in Figure 1.13, can be further divided as follows: **A1**: to design nanostructured thin film cathodes on planar substrates with different morphologies to increase surface area; **A2**: to design hierarchical nanostructured films on pre-nanostructured substrates where the surface areas can be further increased than the simple nanostructured thin films on planar substrates; **B**: to apply laser structuring technique for post-treatment on grown thin film cathodes to achieve advanced nanostructures for larger surface area and better performance; **C1**: to apply surface coatings on the grown thin film cathodes, which can also be combined with nanostructured thin film electrodes; **C2**: to achieve co-grown nanocomposite thin film cathodes for property compensation where the morphology of the secondary phase can be controlled for various designed performance.

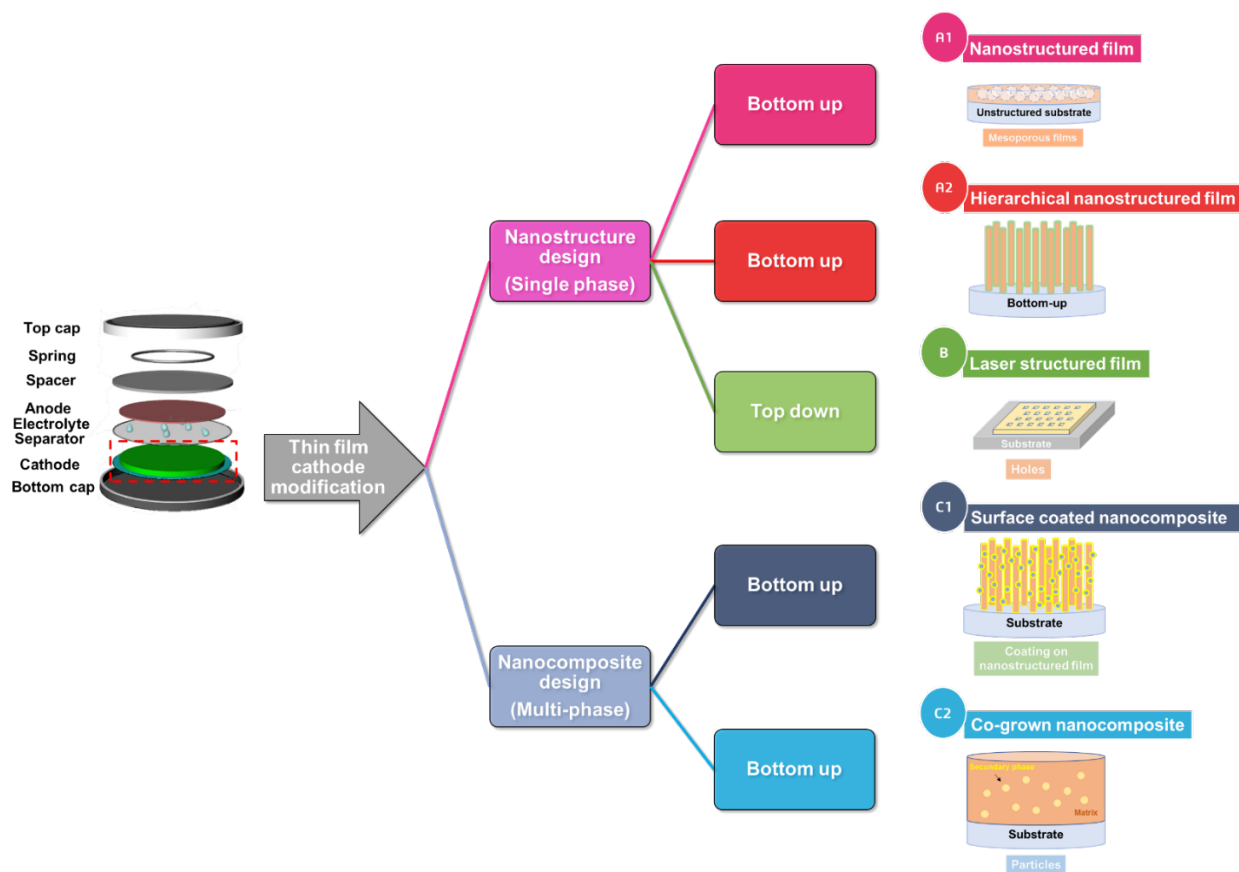


Figure 1.12 Flow chart of modification approaches for cathode electrodes using thin film techniques.

1.4 Thin film electrodes modification

1.4.1 Nanostructure design (single phase)

Despite the advantages of the additive-free thin film cathodes mentioned above,[25] the thin film cathodes have limited energy loading due to constraint electrodes footprint.[72] In order to solve this issue, it's necessary to increase the surface area of electrodes and harvest from 3D structures instead of planar 2D structures, which can increase the loading of active materials as well as the kinetics of electrodes.[73] Different modification approaches to achieve such a goal are introduced and discussed below.

1.4.1.1 Nanostructured thin film electrodes (Bottom-up method)

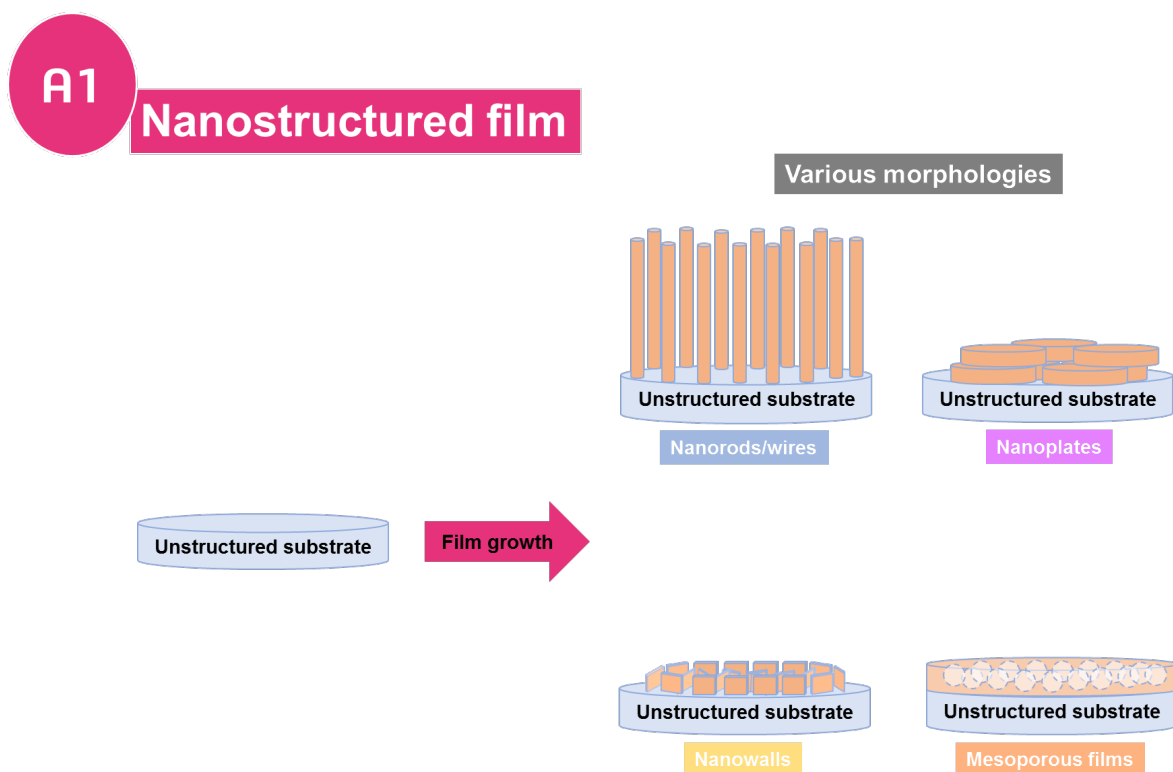


Figure 1.13 Schematic drawing of thin film modification approach that nanostructured thin film cathode is directly grown on planar substrates.

This method refers to cathode thin films with nanostructure design, also known as 3D cathode electrodes, on flat surface substrates. The schematic drawing is presented in Figure 1.14.

Regarding this approach, the electrochemical performance can be tuned mainly through the different morphologies of the nanostructured designs.

Physical vapor deposition Nanorod/needle-like morphology thin films of olivine-type LiFePO_4 was reported by Sun *et al.*[74] using an oblique angle pulsed laser deposition (OAPLD) technique, which is simply to create a non-zero source-to-substrate angle and introduce a shadowing effect to form the isolated nanorod morphology. The method presented slight improvement of performance compared to planar films. [75] Using the same OAPLD technique, Li_2MnO_3 thin films, a highly insulating material,[34] with tilted columnar morphology has been

processed and significantly improved electrochemical performance was demonstrated.[76] The film with thickness of 150 nm was grown on Au buffered stainless steel substrate, which gives 267.46 mAh g⁻¹ initial capacity (99.5 μAh cm⁻² μm⁻¹) and 80% capacity retention (equals to 2×10⁻¹% capacity loss per cycle) at 0.4C for 100 cycles, as well as a satisfying rate performance with 147.84 mAh g⁻¹ (55 μAh cm⁻² μm⁻¹) at 9.3C. The electrochemical performance improves, and a higher amount of active material loading was demonstrated when compared with other reports.[77]–[79] This work proves pulsed laser deposition can a facile one-step method for advanced film morphologies and complicated film compositions designs.

Wet-chemical synthesis LiCoO₂ was explored by Xia *et al.*[80] using a two-step hydrothermal synthesis. This approach first grew self-supported Co₃O₄ nanowire arrays on Au substrates and then applied hydrothermal lithiation to achieve the lithiated LiCoO₂ under two different temperatures, which are layered LiCoO₂ under high temperature and spinel LiCoO₂ under low temperature (HT-LCO and LT-LCO). The synthesized HT-LCO exhibits a hierarchical architecture where the nanowires consist of small head-to-head connected LCO nanorods. This advanced structure shows a large areal capacity of 270 μAh cm⁻² and gravimetric capacity of 135 mAh g⁻¹. Furthermore, HT-LCO also retains its morphology after cycling test and keeps 90% capacity retention for 50 cycles (equivalent to 2×10⁻¹% capacity loss per cycle) at 0.1C. As to rate performance, it can deliver about 103 mAh g⁻¹ at 10C, which is about 76% of that at 0.1C. This two-step hydrothermal synthesis method proposes a facile technique for 3D cathode materials that are difficult to be directly synthesized. However, the chemical lithiation process could be problematic due to the potentially time-consuming and incomplete phase transformation process. In this regards, V₂O₅ cathodes could be better choices due to the simplicity of

synthesizing the nonlithiated phases, and many studies of growing V_2O_5 nanowires/nanorods thin film electrodes have been reported.[81]–[83]

Mesoporous film morphologies are widely explored as it is one of the most effective film morphologies with improved surface area and can be applied on different material systems with various thin film techniques.

Electrostatic spray deposition is a widely applied technique for porous thin films as it is suitable to grow films with porous nature. During the synthesis, the precursor droplets arrive at the substrates when still wet and lead to simultaneous spread of droplets and evaporation of solvent, forming porous structures.[84] Furthermore, the morphologies can still be tuned by altering synthesis parameters and it can be applied on multiple cathode systems.[85]–[88]

Spinel-type Shui *et al.*[89] synthesized and compared sponge-like porous, fractal-like porous, and dense $LiMn_2O_4$ thin films on Pt foils, which turned out the mesoporous sponge-like films with highest surface area demonstrated the best performance with 120 mAh g^{-1} at 0.5C and 62.4 mAh g^{-1} at 10C. Lafont *et al.*[90] also studied $LiNi_{0.5}Mn_{1.5}O_4$ and further explored the effect of solvent towards film morphologies and grain coarsening under annealing.

Layered-type Koike *et al.*[91] compared the porous spinel LT-LCO and layered HT-LCO and reached similar conclusion to Xia's report[80]. The layered HT-LCO has better electrochemical performance with capacity of 140 mAh g^{-1} at rate of 1C and 93% capacity retention for 100 cycles (equals to $9 \times 10^{-2}\%$ capacity loss per cycle) at 1C. Wang *et al.*[92] reported 3D porous V_2O_5 nanoparticles with “multi-deck cage” morphology on stainless steel substrates. As seen in Figure 1.15(a), confirmed by EDS, the 2D reticular structure, 2D-3D mixed structure, and 3D porous multi-deck cage structure were obtained sequentially merely by increasing the deposition time. This structure exhibits an excellent rate performance shown in Figure 1.15(b), i.e., the

gravimetric capacity of the film is 142 mAh g^{-1} at 0.5C and 86.7 mAh g^{-1} at 56C under voltage window between 2.5V - 4.0V (corresponding to 1 Li intercalation). With respect to cycling performance, the film shows no virtual capacity loss for 200 cycles. The group also explored 3D porous $\text{Fe}_{0.1}\text{V}_2\text{O}_{5.15}$ thin films using ESD with enhanced cyclability, suggesting the potential of obtaining complicated film compositions with controlled morphologies for cathodes using EDS.

Template-assisted synthesis Recently, a templated sol-gel method was applied to synthesize mesoporous LiFePO_4 thin films on Pt/Si substrates.[93] Mosa *et al.* mixed polyisobutylene-block-poly(ethylene oxide) (PBI-*b*-PEO) amphiphilic block copolymer with LiFePO_4 sol-gel precursors solution, which was later transferred onto substrates using dip coating to produce composite films, after which the copolymers were removed by thermal treatment to achieve the desired porous film morphology. The assembled cells show excellent electrochemical performance with a volumetric capacity of $40 \text{ } \mu\text{Ah cm}^{-2} \text{ } \mu\text{m}^{-1}$ (gravimetric capacity of 159 mAh g^{-1}) at 1.5C and $38.5 \text{ } \mu\text{Ah cm}^{-2} \text{ } \mu\text{m}^{-1}$ at 7.5C . The cells can be cycled at 1.5C with an initial gravimetric capacity of $159.43 \text{ mAh g}^{-1}$ and $9 \times 10^{-4}\%$ capacity loss per cycle, as well as a high average coulombic efficiency of 99.5% . Furthermore, the films experienced minor structural degradation despite that LiFePO_4 went through relatively large volume change during cycling,[94] which is because the nanostructure is internally connected among pores, providing good structure stability.[95] Park *et al.*[96] also used templated synthesis method on LiMn_2O_4 thin films with enhanced performance. However, the improvement is not as significant as Mosa's report on LiFePO_4 .[93] Despite different physical properties of different cathodes, the performance could also be from the different templates used. Regarding LiFePO_4 , PBI-*b*-PEO precursors were mixed with LiFePO_4 precursors first at atomic level then PBI-*b*-PEO/ LiFePO_4 composite films were deposited, whereas LiMn_2O_4 thin films were coated on arranged insoluble

polystyrene (PS) microspheres on substrates. This indicates that synthesis methods with reactions at a finer scale should lead to better performance, for example, electrodes synthesized using sol-gel method are expected to have better electrochemical performance than that by solid-state reactions.[97]

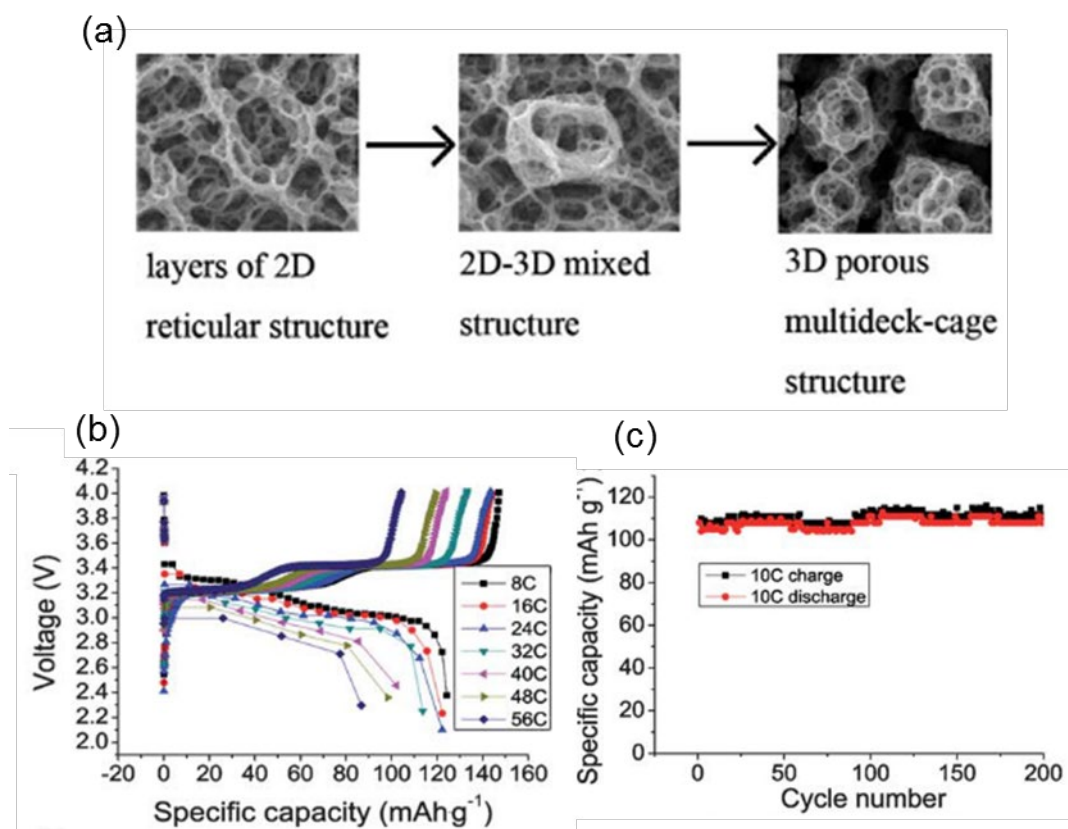


Figure 1.14 (a) Process of how the 3D porous multideck-cage structure is formed from 2D reticular structure with increased layers; (b) Rate performance of 3D porous multideck-cage structure at 8C, 16C, 24C, 32C, 40C, 48C, and 56C; (c) Cycling performance for 200 cycles.

Electrodeposition Other than porous film morphologies and nanorod/pillar morphologies, several other novel film morphologies were also explored. Yu *et al.*[98] applied a sol-gel combined anodic electrodeposition methods and grew mica-like V₂O₅ thin films. The electrodes exhibit excellent cyclic performance with the first-cycle capacity of 620 mAh g⁻¹ (vs Ag/AgCl) about 4.8×10⁻¹% capacity loss per cycle for 50 cycles at 4.6C, and the morphology sustains. Xia

et al.[99] applied a similar combined method for mesoporous LiMn_2O_4 nanowall arrays. They first deposited Mn_3O_4 seeds onto Au substrates using cathodic deposition techniques, then achieved desired LiMn_2O_4 composition through chemical lithiation. It shows a 131.8 mAh g^{-1} gravimetric capacity at 1C and 97.1 mAh g^{-1} at 20C, and the cycling performance is satisfying with only $4 \times 10^{-2}\%$ capacity loss per cycle for 200 cycles. This advanced 3D morphology exhibits better structural stability and electrochemical performance than the previously discussed mesoporous LiMn_2O_4 thin films due to more stable building blocks.

Despite various synthesis techniques or film morphologies, in general, synthesis methods that engage atomic level reactions can lead to finer structures and better performances, and, morphologies with interconnected network are usually superior in structural stability. In addition, not specified above, post-deposition thermal treatment is generally required for better electrochemical performance as it ensures crystallinity and films adhesion with substrates.

1.4.1.2 Hierarchical film growth on nanostructured substrates (Bottom-up method)

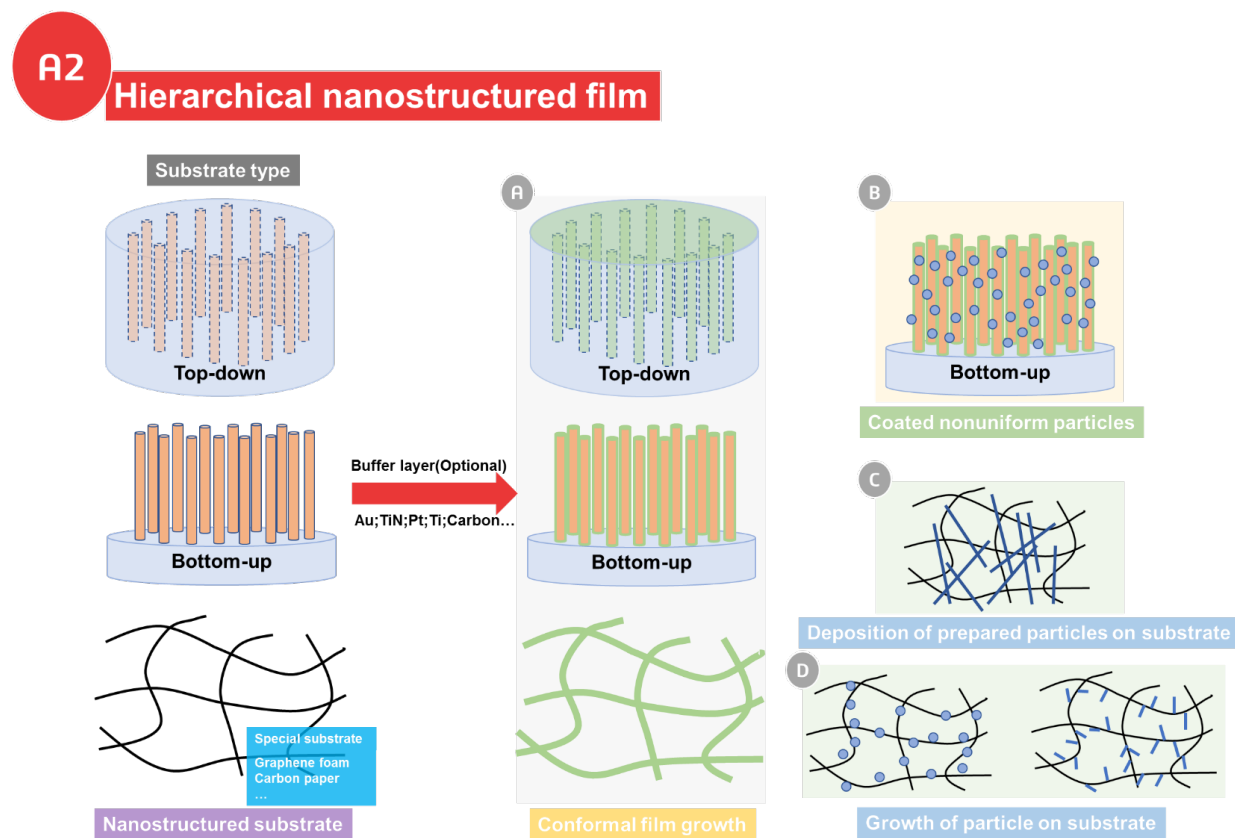


Figure 1.15 Schematic drawing of thin film modification approach that nanostructured thin film cathode is grown on pre-nanostructured substrates to achieve hierarchical nanostructured thin film cathodes.

Slightly different from the abovementioned section “nanostructured films design”, this section refers to film depositions on substrates with nanostructured surfaces. As it is summarized in Figure 1.16, the substrates can be classified as post-structured substrates (patterned substrates) and as-prepared substrates (conductive paper/foam), and post-structured substrates can be further divided into “top-down” and “bottom-up” modified flat surface substrates. In addition to nanostructured substrates, thin films can be deposited onto the substrate’s surfaces through either conformal film depositions or nanostructured film depositions, where the latter are also referred to hierarchical film architecture design. These methods usually grant more design possibilities

and often provide better electrochemical performance due to better utilization of the limited substrates footprints with more sophisticated structures.

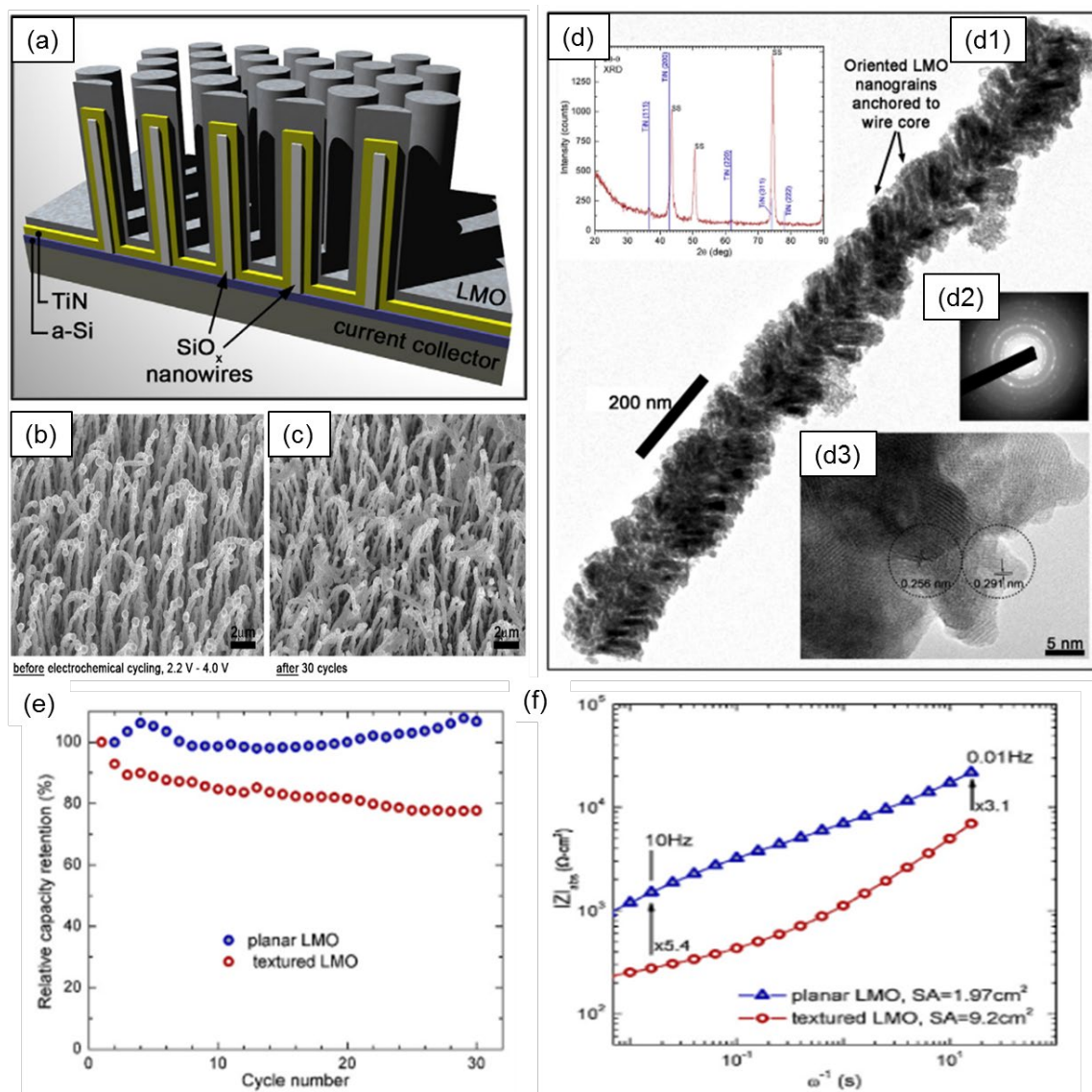


Figure 1.16 (a) Schematic drawing of the finalized film microstructure; (b) SEM images of the film morphology before cycling; (c) SEM images of the film morphology after cycling for 30 cycles; (d) TEM micrograph of individual nanowire; (e) Cycling performance of nanostructured and planar LiMn₂O₄ thin films for 30 cycles; (f) Impedance versus frequency plot of the nanostructured and planar LiMn₂O₄ thin films after cycling.[61]

Plasma-assisted synthesis Bettge *et al.*[100] applied plasma-assisted Vapor-Liquid-Solid (VLS) methods[101] and achieved hierarchical LiMn₂O₄ thin film electrodes. In this work, an

amorphous layer of Si was first grown on planar stainless-steel (SS) substrates using DC magnetron sputtering, then the plasma-assisted VLS was realized to allow the growth of aperiodic SiO₂ nanowires. The nanowires were then coated with metallic TiN as current collectors followed by LiMn₂O₄ coatings using magnetron sputtering, during which the sample stage was periodically tilted to improve film continuity. The schematic drawing of the final film structures is illustrated in Figure 1.17(a). It was reported that the films contained the free-standing nanowires morphology and were well-preserved after cycling, as indicated in Figure 1.17(b) and Figure 1.17(c). The detailed nanostructure of an individual nanowire is shown in figure 1.17(d). It confirmed that the LiMn₂O₄ thin films consist of nanocrystalline grains that are about 5 nm in size and orient around 45° with respect to the longitudinal axis of the nanowire due to the shadowing effect introduced by the oblique angle deposition. Such a morphology exhibited the nanoscale roughness with further increased surface areas (about 5 times than planar morphology), thus showing better electrochemical performance compared to planar films. However, as seen in Figure 1.17(e), the planar film exhibits better cyclability, which maybe attributed to: 1) the detachment of nanowires or LiMn₂O₄ grains due to the interspaced nature of nanowires and grains; 2) the Mn cations dissolution due to increased surface exposure to electrolyte.[102] Despite the undesirable cyclability, the films show obvious decrease in charge transfer resistance due to the shortened particle dimensions as evidenced by EIS results in Figure 6(f). This work is a very comprehensive demonstration of a standard design approach especially with the readily available growth of Si nanowires on almost any substrate surfaces. However, silicon is not conductive and requires additional conductive coatings. In order to solve this issue, plasma assisted synthesis was also applied to achieve carbon-based nanostructures.[103]

Mask-assisted synthesis Shaijumon *et al.*[104] grew Al nanorods directly on Al foils using pulsed-potential electrodeposition with the assistance of anodic aluminum oxide (AAO) membranes,[105] and LiCoO₂ coating was obtained by thermal decomposition of spray-coated LiCoO₂ sol-gel precursors. This method is facile for different cathode systems as Al is a suitable current collector for positive electrodes, however, the density and distribution of the Al nanorods heavily depend on the mask quality.

Template-assisted synthesis Liu *et al.*[65] used engineered tobacco mosaic virus (TMV) as template for 3D LiFePO₄ cathodes with Ni and Ti buffer layers as current collector. TMV is a type of cylindrical particles with high aspect ratio and can be grafted onto metal surfaces through self-assembly. Yim *et al.*[106] achieved 3D hemisphere-structured LiSn_{0.0125}Mn_{1.975}O₄ using PS beads as a template. A suspension of polystyrene nanoparticles was spin-coated on SiO₂/Si substrates, which were then coated with Ti and Pt coatings and lastly LiSn_{0.0125}Mn_{1.975}O₄ was deposited using RF sputtering. The films exhibited an increased specific capacity and rate performance, but slightly decreased capacity retention due to lack of robustness by hemisphere microstructures when compared to planar films. Template-assisted synthesis enjoys advantages regarding versatile film morphologies and different material systems. However, similar to the case of the mask-assisted synthesis, the performances are heavily dependent to the templates and should be designed wisely.

Chemical etching Mattelaer *et al.*[107] derived patterned silicon micropillars using a top-down chemical etching technique for 3D vanadium oxide thin film cathodes with TiN and Pt as current collectors. Both amorphous and crystalline VO₂ and V₂O₅ thin films were then conformally deposited on substrates using ALD and their electrochemical performances were both improved compared to planar geometry. Besides, chemical etching can also achieve

different surface morphologies[108] with further enhanced electrochemical performance.

However, the thickness of films is usually not uniform throughout the surfaces due to shadowing effect.[90] Therefore, techniques that can achieve conformal coatings are essential for excellent electrochemical performance, and ALD is currently the most fitted technique in this direction.[67], [109], [110] Although coating of randomly distributed particles can easily fix this issue, the loading of active materials are greatly reduced.[108]

Lithography Gerasopoulos *et al.*[111] combined top-down and bottom-up methods to achieve 3D V₂O₅ electrodes. First, Au micropillars were grown on silicon substrates using microplating and lithography. Then, a uniform layer of TMV nanorods was coated on Au micropillar surfaces through self-assembly.[65] Next, a uniform layer of Ni was coated on the TMV rods from an electroless plating bath followed by another layer of conformal V₂O₅ through ALD. The results were compared between the only nanostructured V₂O₅ and hierarchical V₂O₅, and the latter one has much higher capacity and rate performance due to further increased surface areas. This indicates that, by combining multiple thin film modification approaches, the design can enjoy structural versatilities for property design and the increased surface area can further enhance electrochemical performance as well as the loading of active materials.

The above discussion has covered the design of nanostructured surface on planar substrates and their effects on battery performance. Different from those substrates, some porous conductive substrates, e.g. nickel foams, graphene foams, carbon papers, etc., can be directly synthesized to build hierarchical 3D electrodes or self-supported flexible electrodes.[112] Among these substrates, the carbon-based substrates are the most studied due to the extremely lightweight and ability to deform.

Deposited particles Due to the porous nature of these substrates, as-grown cathode particles can be directly deposited on using very simple deposition techniques.[113] Gittleson *et al.*[114] used spin-spray layer-by-layer deposition of V_2O_5 nanowires on porous Celgard separators for transparent energy storage. Seng *et al.* [115] mixed multi-wall carbon nanotubes (MWCNTs) with ultra-long V_2O_5 nanowires and formed self-supported flexible films using simple membrane filtration techniques. Zhang *et al.*[116] mixed reduced graphene oxide (rGO) nanosheets with ultralong V_2O_5 nanowires under hydrothermal treatment to form flexible films, where the rGO substrates not only increase the electronic conductivity of the films but also suppress the irreversible phase transition of V_2O_5 under wide voltage range (1.0 -4.0 V).

Grafted particles Despite the simple synthesis procedures, this type of thin films requires large particles to be seated between the empty space of the porous substrates, which can lead to unsatisfying cycling performance as the weak material-to-substrate adhesion and limited loading of active materials. Therefore, particles can be grafted onto substrate surface through coating techniques to avoid this issue. Sathiyaraj *et al.*[117] functionalized carbon nanotubes (CNTs) with concentrated nitric acid to introduce function groups, and grafted V_2O_5 onto the surface through chemical reactions between functional groups. The obtained films have loading of 2 mg cm^{-2} and show 5% capacity drop for 25 cycles tested at 0.5C between 1.5V-4.0V. Chen *et al.*[118] synthesized MWCNT sponges using chemical vapor deposition and V_2O_5 was coated as a conformal amorphous layer by ALD. It shows about 7.5% capacity drop for 25 cycles at 0.2C but with much higher specific capacity than Sathiyaraj's report.[117] This work largely improved the loading of active materials with the high-density CNTs in the sponge, and the core-shell morphology can also prevail in the issue of low mechanical strength and electrical conductivity of amorphous V_2O_5 .[119] Brown *et al.*[120] used a scalable one-step pulsed electrodeposition

technique and grew amorphous V_2O_5 on carbon nanofiber membranes (CNFs), which also demonstrated improved electrochemical performance.[115]

Other cathode material systems were also explored. Chen *et al.*[121] grew a layer of densely anchored VO_2 nanoflakes on carbon cloth substrates with hydrothermal technique, which gives an initial capacity of 289 mAh g^{-1} at 0.2C and 126 mAh g^{-1} at 20C. $LiFePO_4$ nanoparticles was coated on Graphene foams(GFs) by Li *et al.*[122] using hydrothermal method, providing 164 mAh g^{-1} at 0.2C and 114 mAh g^{-1} at 50C. The work further demonstrated flexible all-solid-state battery application with good electrochemical performance under repeated mechanical deformations. Besides, $LiFePO_4$ nanosheets/GFs cathodes synthesized by the same hydrothermal method show slightly better rate performance than that of $LiFePO_4$ nanoparticles/GFs, which is expected as the hierarchical nanosheets structure has higher surface areas.[123]

In conclusion, film depositions on nanostructured substrates (hierarchical nanostructured films) is a more advanced modification approach for thin film cathodes when compared to only nanostructured films. Particle coated nanostructured substrates can have more designable variables such as particle morphologies, particle sizes, particle densities, particle distribution, etc., which on the other hand require more delicate control of synthesis parameters. As to conformal coating, the critical issue comes whether a uniform layer of coating can be achieved, most of which is accomplished by atomic layer deposition or other wet-chemical based methods.[110], [124]–[126]

1.4.1.3 Nanostructuring on planar electrode (Top-down method)

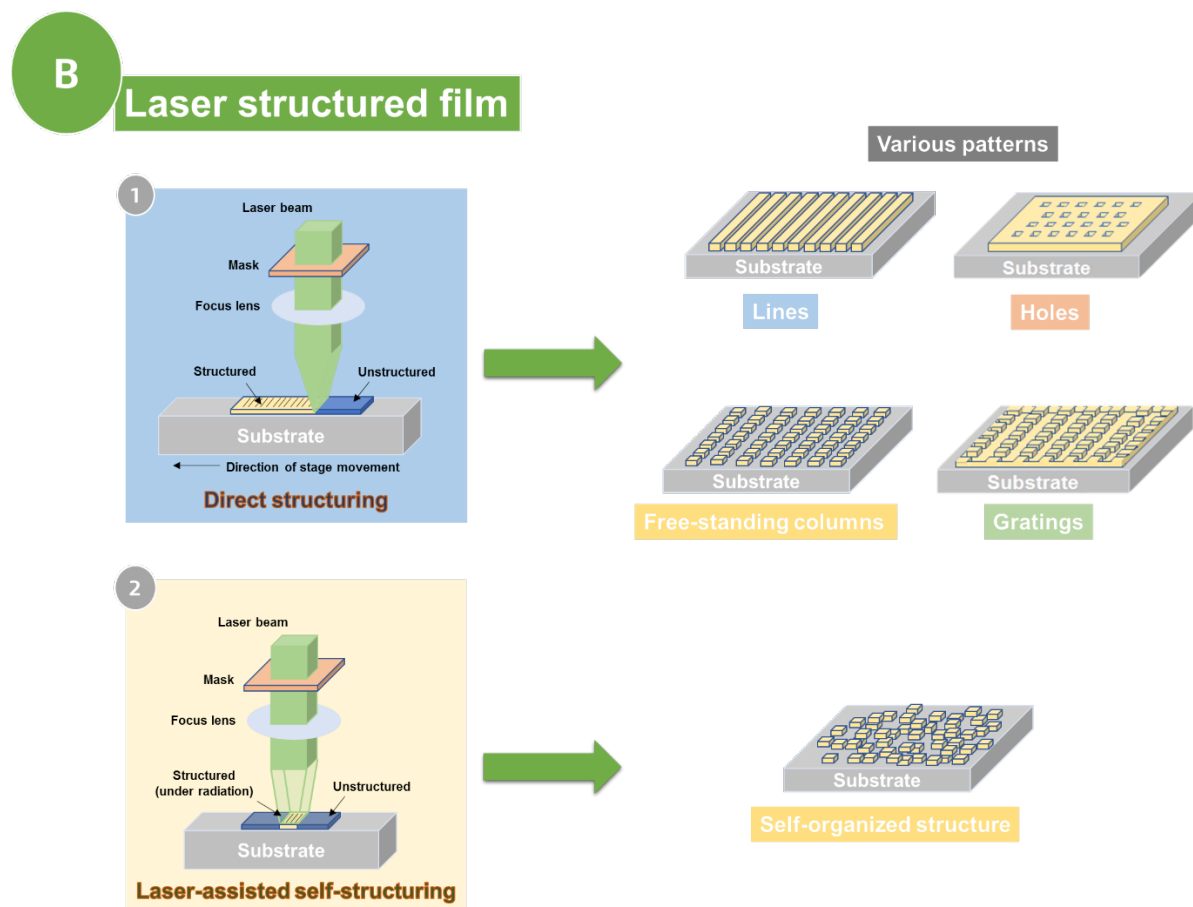


Figure 1.17 Schematic drawing of thin film modification approach that as-deposited thin film electrodes are nanostructured using laser technique.

The above sections introduced a series of modification approaches involving various thin film techniques such as wet-chemistry, vapor deposition, and catalytical growth, etc. Though the abovementioned approaches grant high tunability, desirable structures normally require a complicated synthesis route and post-annealing is often time-consuming. Therefore, these advanced 3D electrodes are not cost-effective enough to be industrialized at this stage, not to mention that most of the work introduced above involves mainly model cathode materials, indicating its early-stage development.

Compared to the above methods, the laser-based cathode processing technique is a relatively new modification approach that can achieve designable 3D nanostructures on electrodes and can accomplish annealing process in large scale and short time.[68] This approach can also be classified as top-down method as it is a post-treatment and requires as-prepared electrodes. The basic operating principle to realize 3D electrode using laser processing techniques can be classified as two types, which are shown in Figure 1.18: 1) Direct structuring: a beam of laser is focused on the film surface and the stage will move in a programmable fashion. Different morphologies can be obtained by different combination of laser mode (pulsed or continuous) and stage movement (direction and speed); 2) Laser-assisted self-structuring: laser beam is shone on the film surfaces and the active materials will be ablated followed by subsequently re-deposition on the film surface to form a structured morphology.

Layered type Most of the current works have been focused on direct structuring due to its programmable characteristics. Kohler *et al*[127] used excimer source laser on RF magnetron sputtered LiCoO₂ thin films and obtained two different conical surfaces by changing laser operation modes. The surface structures show 5 to 10 times larger surface area than the as-deposited films. Laser annealing can be performed for only 13.2 s in ambient air at 700 °C to obtain HT-LCO phase with improved crystallinity and increased grain size. Laser sources with different wavelengths affect differently on electrochemical performance as different ablation rates result in different cone heights. This work demonstrated that the surface area can be largely increased by laser structuring, and microstructures, as well as electrochemical performance, can be tuned by laser operation parameters.

Spinel type Different film morphologies obtained through direct laser structuring were studied and compared. Pröll *et al*. [128] used LiMn₂O₄ thin film cathodes on stainless steel obtained by

RF magnetron sputtering. The wettability of electrolyte and electrochemical performance between different surface morphologies were compared. The four different types of surface morphologies are shown in Figure 1.19(a)-(d), and all the nanostructured surfaces show an increased wettability with electrolyte. The cycling performance can be seen in Figure 1.19(e), the grating structure (Figure 1.19(d)) shows the highest initial capacity of 120 mAh g^{-1} at 0.5C but decays to only 20 mAh g^{-1} at 30^{th} cycle. The line structure (Figure 1.19(b)) shows the best cycling performance while not the highest capacity, which is possibly due to the stable structure but smaller surface area when compared to the grating structure. Despite the improved electrochemical performance, the author claims the laser processed film contains a 30% loss inactive materials due to the laser ablation, which could be a significant issue to active materials loading.

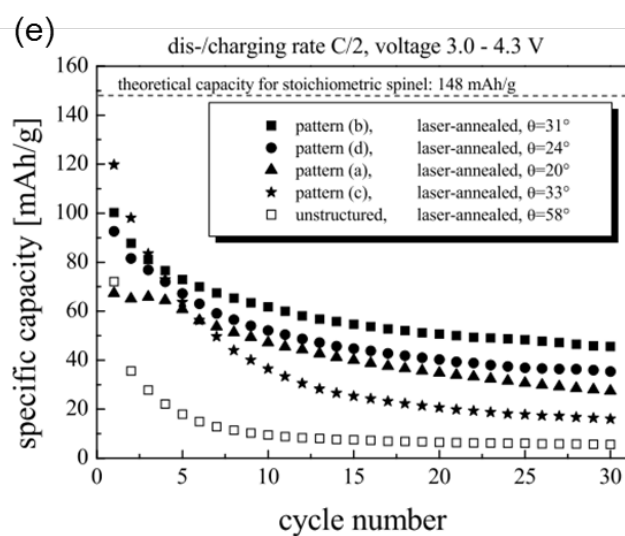
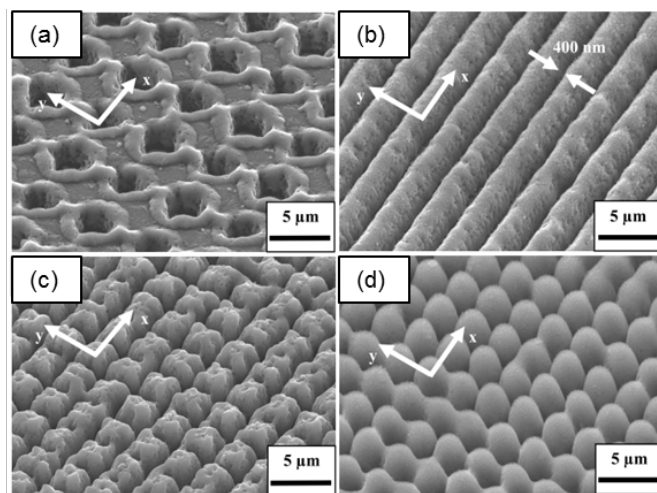


Figure 1.18 SEM micrographs with different patterns of (a) holes, (b) line, (c) grating and (d) free-standing surface structures; (e) Cycling performance of LiMn_2O_4 thin films with different surface morphologies for 30 cycles at 0.5C.[128]

Pröll *et al.*[129] further optimized processing parameters for laser structuring and annealing, which lowered the active material loss to below 0.13%. However, this study shows different results from the previous report. The free-standing morphology in this study has better rate performance and cyclability compared to line structure, while the two has a similar initial capacity. It was explored that the combination of laser structuring as well as laser annealing produced a hierarchical nanoscale and microscale structures which was not discussed in the

previous report.[128] The post-mortem analysis shows that line structure exhibits film delamination and cracking, causing bad cycling performance. Furthermore, this result seems to be contradictory to his previous report as well.[128] Further efforts are needed in this area to reach consensus in the field.

The obvious difference of laser-assisted self-structuring from the direct laser structuring is its free redeposition of the ablated materials on top of the pristine surface structures. Kohler *et al.* studied electrochemical performance self-organized LiCoO₂ thin film and formation mechanism of conical surfaces.[130] The film demonstrated a similar conical structure with slightly higher randomness compared to directly structured surface, and an increase in electrochemical performance as well as cycling stability. Further, as stated above, the formation of such conical structures was proved to consist of different domains with different chemical compositions, thicknesses, and crystallinities, which are related to in-situ grain growth from laser radiation and ex-situ grain growth from redeposition of ablated particles. By applying the same principle, Hudaya *et al.*[131] successfully obtained 3D HT-LCO with largely enhanced rate capability.

In short, laser structuring can be a scalable and cost-effective process, and the nanostructures can be tuned by different laser sources (excimer lasers, ns fiber lasers, and fs-lasers) and operation details.[132] However, not much work is performed in the thin film electrodes field despite that there is an obvious need in thin film cathode field to achieve scalable capability.

1.4.2 Nanocomposite design (two or more phases)

The above sections have summarized the improvement of the electrochemical performance of single-phase thin film cathodes via nanostructure designs, with a basic principle, i.e., to design nanostructures with high surface area that are mechanically stable. However, such designs can have certain inevitable issues, for example, the highly reactive surface states can favor

undesirable side reactions at the electrode-electrolyte interfaces.[86], [104], [117], [133] Besides, the nanostructured materials can still experience intrinsic property issues such as low conductivity, bad chemical stability, etc. due to the limitations of selected active materials. Therefore, the concept of nanocomposite can be introduced to overcome these issues by introducing a second phase (or more) that is high in conductivity or chemical stability.[134] This is an important modification approach as it provides flexible nanostructured design approaches.

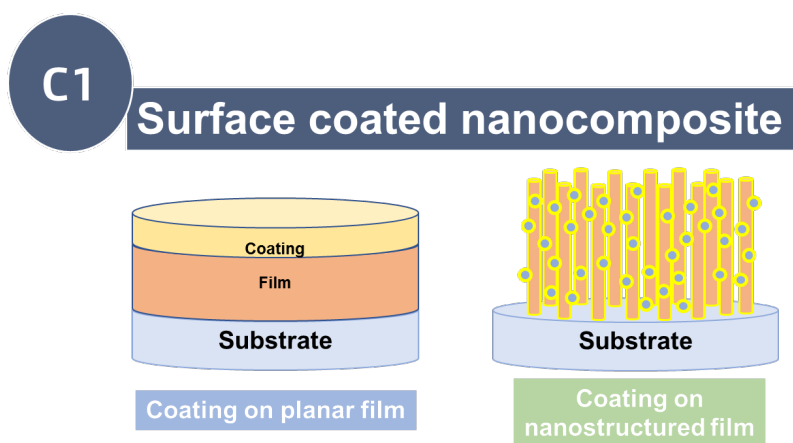


Figure 1.19 Schematic drawing of thin film modification approach of surface coating on planar or nanostructured thin film electrodes.

1.4.2.1 Surface coating nanocomposite (Bottom-up method)

Nanocomposite modification types can be simply classified into two groups, i.e., introducing the second phase on top of the matrix phase, that is, surface coating. The schematic drawing of different surface coating modification types can be divided into 1) surface coating on planar films and 2) surface coating on nanostructured films.

Physical protection layers Due to the well-known transition metal dissolution and electrolyte oxidation issues of LiMn_2O_4 , [47], [48] this material usually requires surface coatings as physical protective layers.[135] Mattelaer *et al.*[60] studied the outcome of ultrathin amorphous coating of Al_2O_3 and TiO_2 by ALD on Pt/TiN/SiO₂/Si substrates. Upon overcharging (> 4.4V) at low

cycle rate (0.5C), both Al_2O_3 and TiO_2 are useful in suppressing electrolyte oxidation, while TiO_2 has slightly better suppression but also needs to go through an activation process before it can act as a protective layer. However, the rate performance of Al_2O_3 coated LiMn_2O_4 deteriorates very fast with increasing C-rate, even worse than uncoated LiMn_2O_4 , whereas TiO_2 coated LiMn_2O_4 shows an improved rate capability than uncoated LiMn_2O_4 . This behavior is also observed morphologically, where the surface of cycled Al_2O_3 coated LiMn_2O_4 roughens more dramatically than that of TiO_2 coated LiMn_2O_4 , which is because the dielectric Al_2O_3 coating only defers the SEI formation but TiO_2 suppresses the SEI formation as well as contributes to lithium ion conductivity. In the meantime, Teranishi *et al.*[136] obtained similar yet more comprehensive conclusions using LiCoO_2 electrodes with dielectric BaTiO_3 (BTO) coating. Fully covered planar BTO coating and dot BTO partially coated on LCO electrodes were compared. The planar BTO shows similar results with Mattelaer's case,[60] but the dot BTO coating shows highly enhanced rate performance, which is explained by Teranishi *et al.* that the BTO-LCO-electrolyte triple junction generates negative charges by the enhanced electric dipole moment at the junction, which attracts Li^+ ions. This work makes a great demonstration on how thin film systems are helpful in analyzing working mechanisms of complicated nanostructured/nanocomposite electrodes without hindering effects from binders or conductive additives.

Besides electrochemically inactive coatings, researchers also applied solid-state electrolyte materials directly as coatings, such as LiPON [137] and Li_3PO_4 [138], to improve the electrochemical performance of thin film cathodes.

Better conductive media Surface coating techniques are usually applied together with 3D nanostructured electrodes for further improvement in performance as advanced electrodes.

Olivine LiFePO_4 cathodes are known for sluggish kinetics due to the one-dimensional lithium conduction paths and low electrical conductivity of the crystal structure,[35] surface coatings are commonly applied as better electron/ion-conducting media.[38], [139] Carbon coating was applied to tobacco mosaic virus (TMV) template-assisted LiFePO_4 nanoforest with Ti and Ni as current collectors.[65] $\text{LiFePO}_4@C$ nanoforest cathode shows much better rate performance and cycling stability with nearly 100% columbic efficiency and pertained morphology after 450 cycles. Similar structures can also be achieved through other synthesis approaches such as laser structuring on carbon-coated planar films[131] or simple PVD technique using composite targets.[140]

Instead of the most commonly applied carbon coatings,[42] N-doped carbon (N-C) coating can be used as an advanced coating material because N element was proven to be able to promote electron transfer and lower the energy barrier of lithium penetration in LIB applications.[141]–[143] A continuous layer of cross-linked $\text{LiFePO}_4@N-C$ particles with nanopores was uniformly decorated on the carbon cloth surface by Pan *et al.*,[144] which improves the gravimetric capacity, rate performance, cycling performance with decreased polarization and charge transfer resistance when compared to LiFePO_4/C slurry electrode.

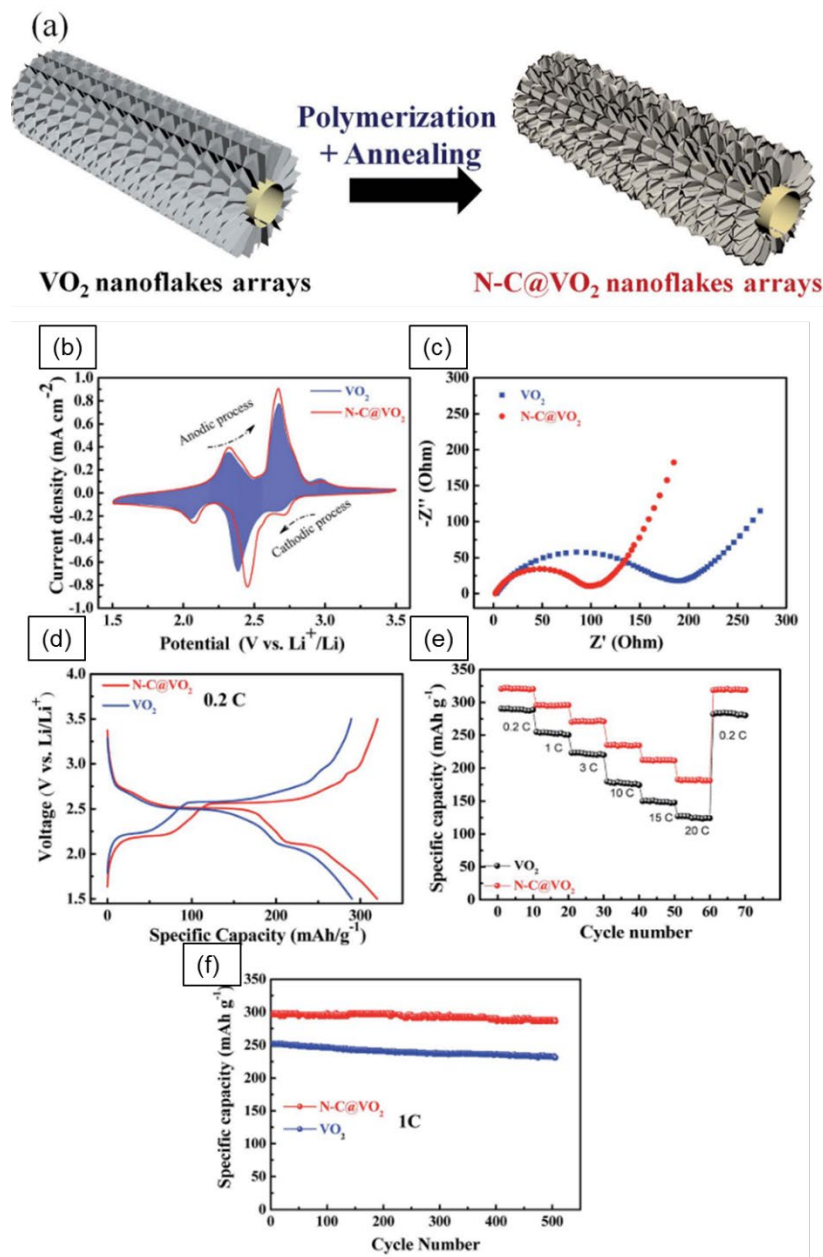


Figure 1.20 (a) Schematic drawing of the synthesis procedure of N-C@VO₂ nanoflakes arrays; (b) Cyclic voltammetry of VO₂ nanoflakes arrays and N-C@VO₂ nanoflakes arrays; (c) EIS measurements of VO₂ nanoflakes arrays and N-C@VO₂ nanoflakes arrays; (d) Charge-discharge profile of VO₂ nanoflakes arrays and N-C@VO₂ nanoflakes arrays at 0.2C; (e) Rate performance of VO₂ nanoflakes arrays and N-C@VO₂ nanoflakes arrays at 0.2C, 1C, 3C, 10C, 15C, and 20C; (f) Cycling performance of VO₂ nanoflakes arrays and N-C@VO₂ nanoflakes arrays for 500 cycles at 1C.[121]

Similar to LiFePO_4 , VO_2 also experiences low electrical conductivity. N-C coating was deposited on VO_2 nanoflakes by Chen *et al.*[121]. As shown in Figure 1.21(a), the VO_2 nanoflakes were first anchored on carbon cloth through hydrothermal synthesis, and the N-C coating about 3 nm in thickness was subsequently coated by self-polymerization. The electrochemical performance comparison is shown from Figure 1.21(b)- (f). Figure 1.21(b) shows that $\text{VO}_2@\text{N-C}$ has better electrochemical reactivity and smaller polarization due to a better conductive network of N-C coating compared to pure VO_2 nanoflakes, which is also confirmed by the EIS results in Figure 1.21(c). The charge-discharge profile in Figure 1.21(d) of $\text{VO}_2@\text{N-C}$ and VO_2 at 0.2C shows that $\text{VO}_2@\text{N-C}$ has higher discharge capacity of 325 mAh g^{-1} at 0.2C, decreased polarization, as shown in the rate test results in Figure 1.21(e). Furthermore, $\text{VO}_2@\text{N-C}$ showed good cycling performance with about $9.4 \times 10^{-3}\%$ capacity loss per cycle at 1C for 500 cycles.

Different from carbon-based coatings, Xia *et al.*[145] explored hydrogen molybdenum bronze (HMB), a n-type semiconductor with both high ionic conductivity ($10^{-3} - 10^{-2} \text{ S m}^{-1}$) and electrical conductivity ($10^3 - 10^5 \text{ S m}^{-1}$), as coating material to improve film kinetics. VO_2 nanoflakes arrays were obtained on Graphene foams (GFs) using hydrothermal synthesis and a layer of 15 nm thick HMB shell was coated on the nanoflakes, which largely improves the capacity and rate performance compared to similar the VO_2 nanoflakes on carbon cloth mentioned above.[121] It exhibits a specific capacity of 415 mAh g^{-1} (0.2C) and 219 mAh g^{-1} (30C) with satisfying cycling performance at very high current densities (about $9.1 \times 10^{-3}\%$ capacity loss per cycle at 30C for 500 cycles).

HF scavengers Except for conductive coating functionality, surface coating can also act as HF scavengers[146] in liquid electrolytes involved batteries as the inevitable trace amount of

moisture in the batteries can react with electrolyte and generate HF to further attack active cathode materials and cause permanent performance decay.[147] It is worth noting that the role of surface coatings is similar to physical protective layers, but in this scenario the side reaction specifically refers to the HF attack that only occurs in specific battery systems. Liu *et al.*[148] coated an amorphous layer of Li_3PO_4 on amorphous FePO_4 by ALD on CNTs. The author observed the increased structural stability of Li_3PO_4 coated cathodes as it acts as HF scavenger for suppressing the SEI formation. In addition, Al_2O_3 was coated on FeF_2 with inverse opal Ni 3D scaffold substrates using ALD, which further confirms that combinations between 3D nanostructures and surface coating can maintain good kinetics and suppress side reactions due to large surface areas.[149]

Surface coating approach is an effective method to modify thin film cathodes, and it can be combined with nanostructured cathodes to further improve the performance. Roughly, the surface coating can act differently such as conductivity promoter,[65], [121], [144], [145] protective layer,[60] HF scavenger in liquid cells, [146]–[149] or surface chemistry modifier (the last example was not introduced above).[150] Furthermore, the surface coating morphology can be either rough particle coating, core-shell coating or ultrathin coating with different pros and cons.[150]

1.4.2.2 Co-grown nanocomposite (Bottom-up method)

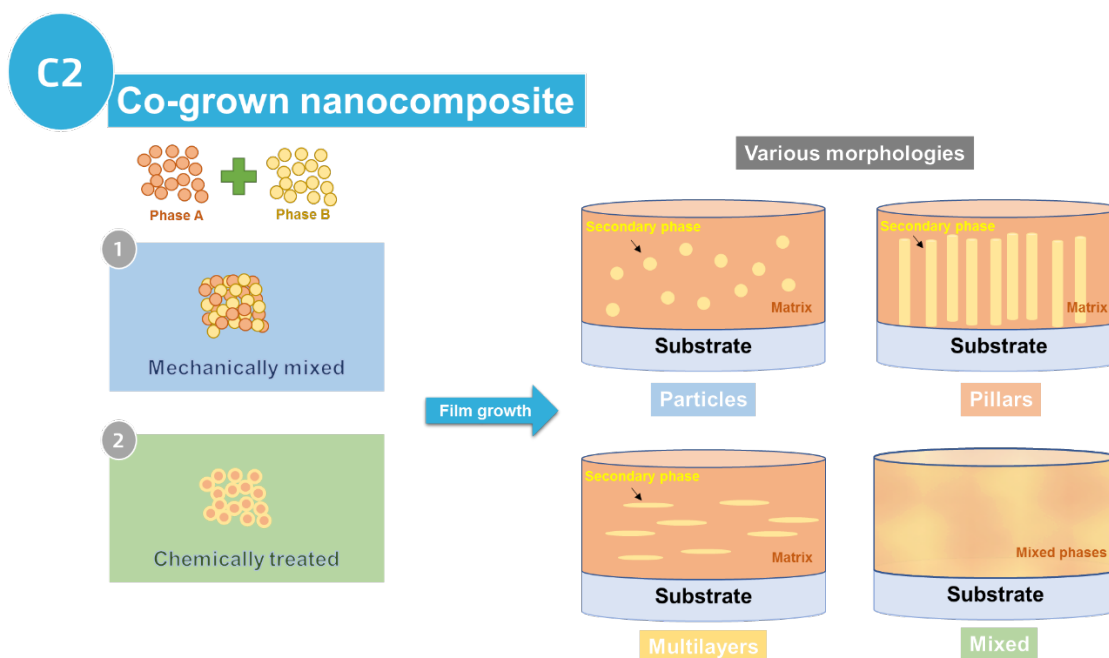


Figure 1.21 Schematic drawing of thin film modification approach that the secondary phase and matrix phase are co-deposited on substrates with different morphologies, where the two phases can be either mixed mechanically or treated using chemical method, and the morphology of the secondary phase can be tuned.

Apart from surface coatings, nanocomposite approaches can also be designed from the bulk perspective of thin film cathodes. The co-grown nanocomposites can be regarded as a mimic of thick film slurry electrodes with co-deposition of two different phases and the morphology of the secondary phase is tunable in the matrix phase. The most representative modification examples are schemed in Figure 11. In short, the two phases can be mixed either mechanically or chemically, which can then be co-grown on substrates with alterable morphologies such as particles, multilayers, nanopillars, or mixed domains.

Carbon conductive additives As it is introduced above, thin film electrodes generally experience slow kinetics as most cathode materials are oxides with sluggish kinetics, and the attempt of introducing conductive materials into cathode thin films can be traced back to early

2000s. LiFePO_4 , as model system with sluggish kinetics, was studied by Chiu.[151] He mechanically mixed LiFePO_4 precursors with carbon sources and made LiFePO_4/C composite targets. The LiFePO_4/C composite films were deposited by RF magnetron sputtering on Si(100) and stainless steel substrates under optimized growth parameters, which show increased capacity and decreased resistance compared to pure LiFePO_4 . Afterwards, Chiu *et al.*[152] further applied a layer of Ti buffer and proved it be able to enhance crystallization, grain growth, and increase film-to-substrate adhesion. Further, Lu *et al.*[153] and Zhou *et al.*[154] explored the effect of carbon amount in the cathode matrix. Despite the different conclusions in detail,[97] they arrived at a general trend that the specific capacity will be lowered but the kinetics of the electrodes will be improved with increase of carbon amount. Further, a minimum amount of carbon, is required to reach desirable electrochemical performance but overdosed carbon can start to deteriorate the performance. Besides, the selection of carbon sources can also make a difference in performance.

Metal conductive additives Conductive materials other than carbon were also studied. Lu *et al.*[155] used Ag as the second conductive phase. Different from the mechanically mixed carbon source and LiFePO_4 , Ag was chemically coated on LiFePO_4 particles via colloidal process before mixed and pressed into a composite target, where the composite film was then deposited on Pt/Ti/ SiO_2 /Si substrates using PLD. The $\text{LiFePO}_4/\text{Ag}$ composite films demonstrate much higher volumetric capacity, better rate performance and increased cycling stability with much lower weight percent of Ag compared to LiFePO_4/C films. This behavior can be possibly explained by the more uniform mixture between active materials and conductive materials through chemical coating at atomic level compared to simple mechanical mixing.[97] In addition to Ag, Au and mixed metals were also studied for LiFePO_4 ,[156] and the mixed metal can not only increase

kinetics but also prevent the active materials from unfavorable side reactions for specific cathode systems.[157]

All the above works lack the discussion from the morphological perspective of the nanocomposites, that is, no direct evidence such as TEM images were presented to confirm how the secondary phase is distributed in the matrix phase, which could lead to inaccurate conclusions. For example, Eftekhari claims that cobalt oxide exists as surface coating on LiMn_2O_4 through mixed-metal co-deposition process[157] because the capacity fade was suppressed and surface coating was proved to be effective in this sense.[150] However, this suppression could also be from the change of Mn valence states due to interdiffusion of cobalt oxide phase with different morphologies.[47] This lacking perspective is critical as it can provide design insights and helps study working mechanisms.

Metal conductive additives PLD, known as an easy stoichiometry control technique,[123], [158]–[161] combined with careful TEM studies examining the microstructures of thin film cathodes have been proven effective in studying fundamental mechanisms of cathode materials and improving electrochemical performance.[76], [162]–[164] Inspired by $\text{LiFePO}_4/\text{Ag}$ composite example, $\text{LiNi}_{0.5}\text{Mn}_{0.3}\text{Co}_{0.2}\text{O}_2(\text{NMC532})/\text{Au}$ nanocomposite thin films with different Au concentration was deposited on Au buffered stainless steel substrates.[164] The results show that moderate amount of Au addition can improve the electrochemical reversibility and Au particles act as local current collectors in the electrode and shortens the lithium/electron diffusion pathways. The details can be found in Chapter 3. In addition, metal-oxides nanocomposite $\text{Li}_2\text{MnO}_3/\text{Au}$ with Au existing as tilted pillars instead of particles, which shows improved kinetics and the tilted pillars renders anisotropic optical properties. The details can be found in Chapter 5.

Properties compensators The secondary phase can not only enhance conductivity, but also act as a structural stabilizer, cost reducer, or simply any role to compensate for the downside of matrix materials. Shi *et al.*[165] designed a very simple composite structure of pure phase LiV_3O_8 , but with nanocrystalline phases dispersed in amorphous matrix. Amorphous LiV_3O_8 has larger lithium diffusion coefficient, giving higher capacity and rate performance, whereas crystalline LiV_3O_8 has better capacity retention. This simple nanocomposite design combined both the advantages of amorphous and crystalline LiV_3O_8 and the properties can be further tuned by the ratio and distribution of the two phases. Yu *et al.*[166] followed similar design principle and achieved nanocrystalline $\text{Li}_4\text{Ti}_5\text{O}_{12}$ (LTO)/ TiO_2 (TO) nanocomposite. LTO contains a stable structure upon cycling while TO has better rate performance. The nanocrystalline composite provides high density of grain boundaries and electrolyte available channels for high capacity and good cycle stability.

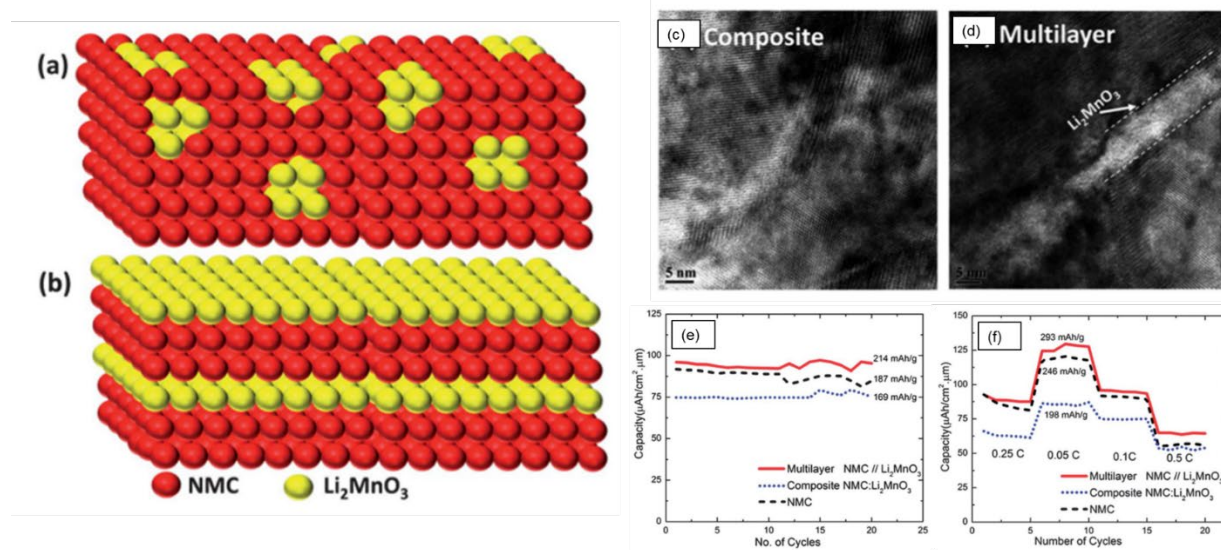


Figure 1.22 (a) Schematic drawing of composite NMC- Li_2MnO_3 thin film; (b) Schematic drawing of multilayered NMC- Li_2MnO_3 thin film; (c) TEM micrograph showing microstructure of composite NMC- Li_2MnO_3 thin film; (d) TEM micrograph showing microstructure of multilayered NMC- Li_2MnO_3 thin film; (e) Cycling performance of composite NMC- Li_2MnO_3 , multilayered NMC- Li_2MnO_3 , and pure NMC for 25 cycles; (f) Rate capability of composite NMC- Li_2MnO_3 , multilayered NMC- Li_2MnO_3 , and pure NMC.[163]

The composite Li rich cathode has very large voltage window, high reversible capacity, and decreased cost due to the introduced secondary structural stabilizing phase (Li_2MnO_3), but how Li_2MnO_3 takes role in the composite remains debating.[34] Clement *et al.* studied the performance between traditional Li rich mixed-phase composite cathode and multilayered nanocomposite where the Li_2MnO_3 exists in NMC matrix with multilayer morphology,[163] which is schemed in Figure 13 (a)-(b). The multilayer composite has the isolated nanosized Li_2MnO_3 multilayer domains whereas the mixed-phase composite has uniformly mixed two materials, as indicated in Figure 13 (c)-(d), which allows higher capacity and better rate performance (Figure 13(f)) as the lithium diffusion behavior and pathways are more affected by NMC, that is, more conductive. In the meantime, the nanosized domains still stabilize the structure with better cycling performance shown in Figure 13(e). The work demonstrates the tunability of electrochemical performance with different morphology of the secondary phase and the additives-free thin films can provide new insight for nanocomposite design.[167]

In short, nanocomposite design is also a promising solution to improve the film kinetics like single phase nanostructure design. Additionally, with the correct selection of the secondary phase, this method can help compensate the downside of the nanostructured electrodes such as highly reactive electrode-electrolyte interfaces. However, there is lack of work regarding the morphological study of co-grown nanocomposites, which can provide insights on designing advanced thin film cathode materials.

2. EXPERIMENTAL SECTION

2.1 Pulsed laser deposition (PLD)

Pulsed laser deposition (PLD) belongs to the physical vapor deposition which applies Ultraviolet (UV) light to hit target materials. The highly spatial coherent laser enables condensed and directional irradiation that has high energy densities. The PLD technique has advantages such as 1) easy complex stoichiometry control as it can easily reproduce the stoichiometry in the target materials; 2) almost all metals and ceramics can be grown as thin films using PLD techniques due to the versatile target preparation process.

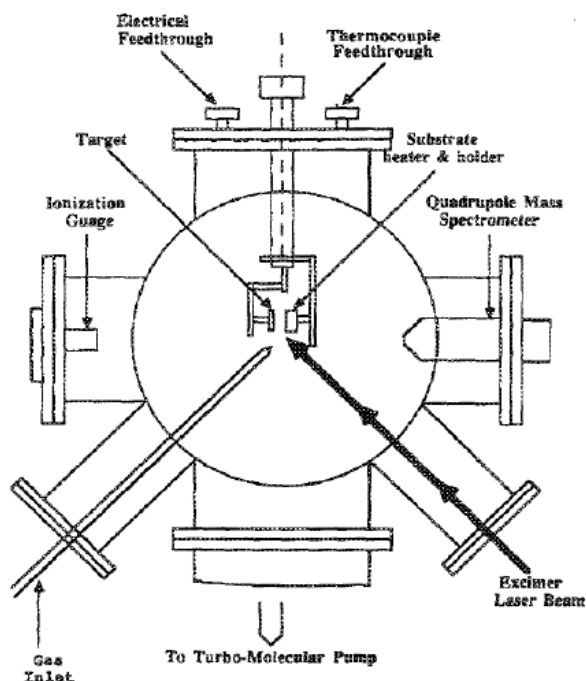


Figure 2.1 Schematic drawing of a general PLD system.[168]

The typical setup of the PLD system contains several critical parts including a multi-target holder, a substrate holder, and a turbo pump system able to reach high vacuum. The illustrated setup is shown in Figure 2.1. For a general deposition, the substrate is loaded onto the holder, the chamber is

pumped to vacuum by turbo pump, the substrate is then heated and stabilized to the desired temperature, the chamber can then either be kept at vacuum or filled under gas atmosphere. The laser is then passed through the window through a set of optical lenses and focused on the target surface. It's also important to introduce the detailed process of a thin film deposition to understand the mechanism of the growth. During the process, the laser radiation is first hitting the surface of the target. The electromagnetic energy of the laser is absorbed by the target materials and then transferred to electronic excitation. Then, the energy will be further transferred into thermal and kinetic energy, which causes the melt and vaporization of surface target materials and later formation of “plume”, which consists of different energized species such as atoms, molecules, ions, electrons, etc. At last the species will travel toward the substrate surface and stack to form thin films. Several typical types of growth models include 3D island-type growth, 2D layer-by-layer growth, and mixed layer/island growth, which is shown in Figure 2.2. The different growth quality of films can be related to temperature, background pressure, substrate-to-target distance, laser parameters, target properties, substrate properties, and laser-target interactions.

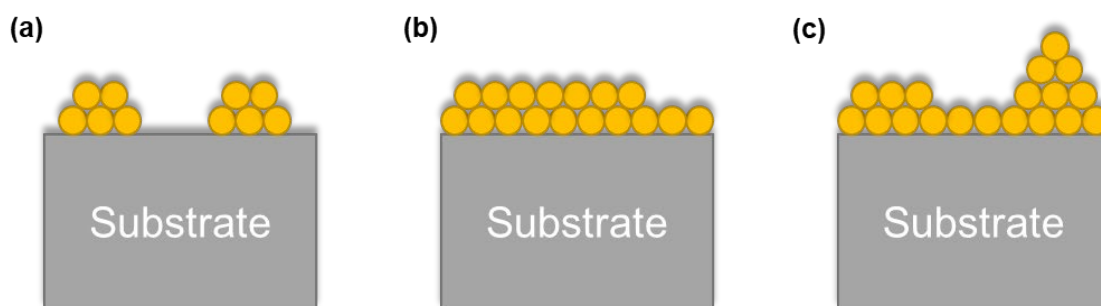


Figure 2.2 Schematic drawing of three different thin film growth modes: (a) island mode, (b) layer-by-layer mode, and (c) mixed island-layer mode.

Based on the mechanism proposed by J. Narayan and R.K. Singh in 1990,[168] the target-laser interaction can be summarized into three steps, which are shown in Figure 2.3: 1) interactions between laser and target that causes evaporation of surface materials; 2) interactions between

evaporated materials and laser that causes plasma formation; 3) anisotropic expansion of plume and deposition of films. For all the films mentioned in later sections, the depositions are achieved using Lambda Physik Compex Pro 205, $\lambda=248\text{nm}$). Different targets were prepared for different thin film depositions. The temperatures used for depositions were between $550\text{ }^{\circ}\text{C}$ to $750\text{ }^{\circ}\text{C}$. The oxygen partial pressure for different depositions were between 10 mTorr to 50 mTorr. The substrate-to-target distance for all depositions was 4.5 cm. The laser fluence was adjusted between 5 to 12 J/cm^2 . Information about the target making process and more detailed experiment can be found in later sections.

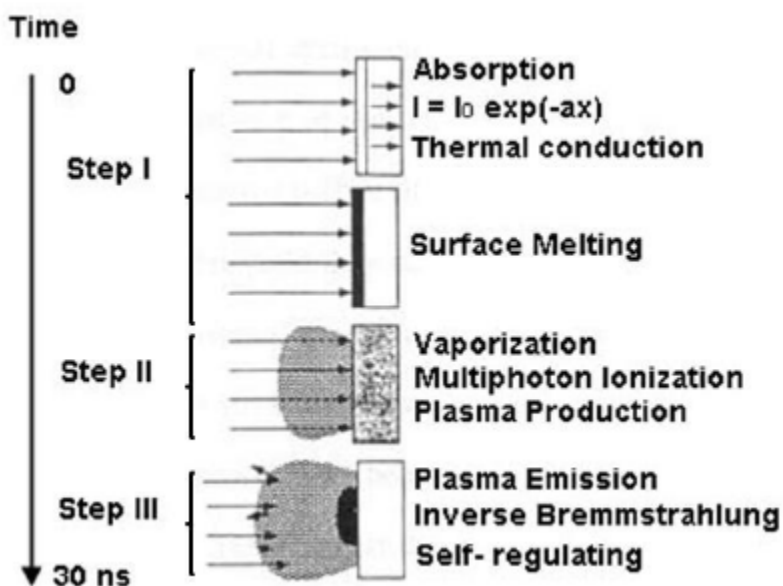


Figure 2.3 Laser-target interaction during formation of one pulse.[168]

2.2 Sputter

Sputter is another type of PVD technique that enjoys great interest especially in industrial fields, and the schematic drawing of a common sputter system is shown in Figure 2.4. During the deposition, a high negative bias is applied at the cathode, and it will ionize the ambient gas

molecules. The positive ionized gas ions are then attracted to the biased target materials and further trigger a cascade collision of ions and electrons. The bombardment of gas ions introduces sputtered target particles and then be deposited to the substrates. In most sputter systems, the magnetron setup is applied where permanent magnets are placed behind the target to create a magnetic field to help the species move along a helical path near target, which can largely improve the ionization yield of the system.[168] In our work, the DC sputter was applied for growth of Au buffer layers on stainless steel substrates, and more details will be discussed in later corresponding sections.

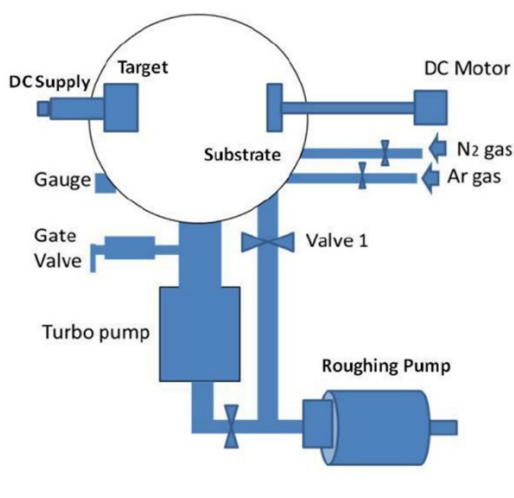


Figure 2.4 Schematic drawing of a sputter system.[168]

2.3 Microstructural characterization

2.3.1 X-ray Diffraction (XRD)

X-ray diffraction is a widely applied technique for crystal structure investigation, which is usually applied for phase identification, lattice parameters determination, texture properties measurement, average grain size estimation, internal strain calculation, etc. of samples. For the most commonly used XRD setup, the X-ray is generated from a cathode tube using Cu source

target. The X-ray is then radiated at the sample with a specific angle and be collected by the detector. By Bragg's law, the obtained XRD pattern will only have characteristic peaks at certain angles, which correlates source properties and materials properties,

$$n\lambda = 2d \sin \theta$$

where n represents an integer, λ represents the characteristic wavelength of the X-ray source, d represents the d spacing of the materials to be measured, and θ represents the angle incident X-ray radiation forms with sample surface. The illustration of Bragg's law is shown in Figure 2.5.

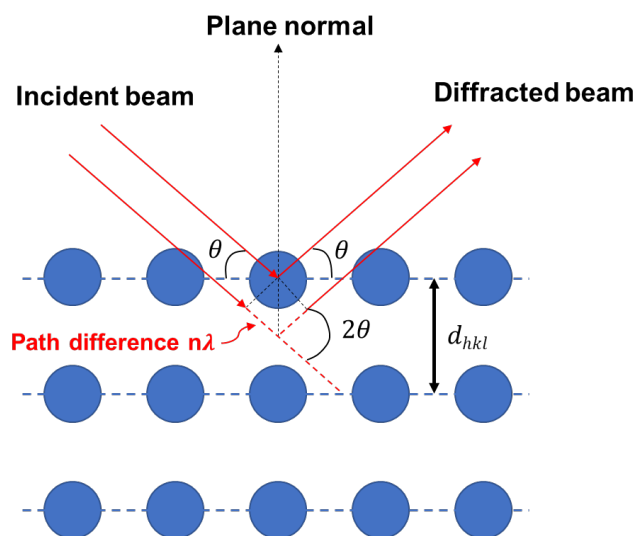


Figure 2.5 Schematic drawing showing fundamental mechanism of Bragg's law.

In this work, the XRD was primarily applied for phase identification, crystal lattice parameter measurement, and texture properties evaluation. The PANalytical Empyrean 2 system is used for all measurements where the X-ray source is Cu, and more details can be found in appropriate sections.

2.3.2 Scanning electron microscopy (SEM)

Scanning electron microscopy (SEM) is a commonly applied technique for microstructure characterization. For a SEM, the high energy ion beam reacts with the surface of specimen and produce various signals such as secondary electrons, backscattered electrons, characteristic X-rays, etc., which is shown in Figure 2.6.[169] Different information can be obtained from different signals, for example, secondary electrons (SE) provide majorly morphological and topological information of a sample, whereas backscattered electrons (BSE) mainly provide compositional contrast. Further, characteristic X-rays can help identify compositional information including elements identification and distribution. In this work, FEI NOVA nanoSEM field emission SEM was used for all SEM imaging, which was mainly used for surface morphology confirmation of thin film cathodes.

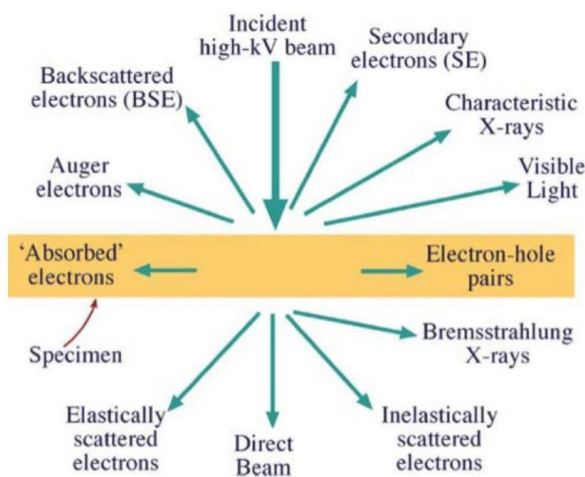


Figure 2.6 Different types of signals can be generated from an incident electron beam.[169]

2.3.3 Transmission electron microscopy (TEM)

Like SEM, TEM also utilizes high energy electron beam to obtain high-resolution images for specimen. However, different from SEM, the TEM uses transmitted electrons instead of reflected

distinguishing the closest spacing between two points, which can be calculated ideally by Rayleigh criterion:

$$r = \frac{0.612\lambda}{n(\sin \alpha)}$$

where λ represents the wavelength used to imaging an object, α represents the aperture angle, and $n=1$ when the system is under vacuum condition. However, for a real TEM system, there are several factors affecting the ultimate resolution including astigmatism, chromatic aberration, and spherical aberration.

Two primary operation modes existing in a TEM: imaging mode and diffraction mode, which are shown in Figure 2.8[165]. The two modes can be altered by changing the focal plane position of the intermediate lens. Regarding diffraction mode, the image plane is adjusted to the back focal plane of the objective lens. As to imaging mode, the image plane is at the image plane of the objective lens. In this work, scanning transmission electron microscopy (STEM) and high-resolution TEM (HRTEM) are critical. For HRTEM, there are several essential requirements: 1) objective lens have to be set to reach shortest focal length possible; 2) higher accelerating voltage is more ideal; 3) field emission guns is better as it reduces chromatic aberration; 4) smaller objective aperture is suitable as it reduces spherical aberration; 4) the sample of interest should be high quality with limited ion damage. As to STEM, it is a working mode where beam is parallel to the optic axis, which produces the contrast proportional to atomic number Z . Apart from these two primary modes, electron energy loss spectroscopy (EELS) and energy dispersive X-ray spectroscopy (EDS) can also be collected simultaneously while obtaining regular TEM images.

To obtain a good TEM image, the thin film sample preparation process is critical. For both cross-sectional and plan-view TEM, there are several steps required to obtain samples with good

quality. 1) the sample needs to be first cut to small pieces about $1\text{ mm} \times 3\text{ mm}$ in size; 2) two pieces need to be glued together with film facing each other under heating for 4 hours; 3) the sample needs to be pre-thinned till thickness is between $40\ \mu\text{m}$ to $60\ \mu\text{m}$, and followed by polishing to avoid visible surface damages using diamond papers ($15\ \mu\text{m}$, $6\ \mu\text{m}$, and $1\ \mu\text{m}$); 4) further thin and polish the sample to be around $25\ \mu\text{m}$ thick using a dimpler; 5) use ion milling to create an electron transparent region, which generally happens at the center of the dimple track.

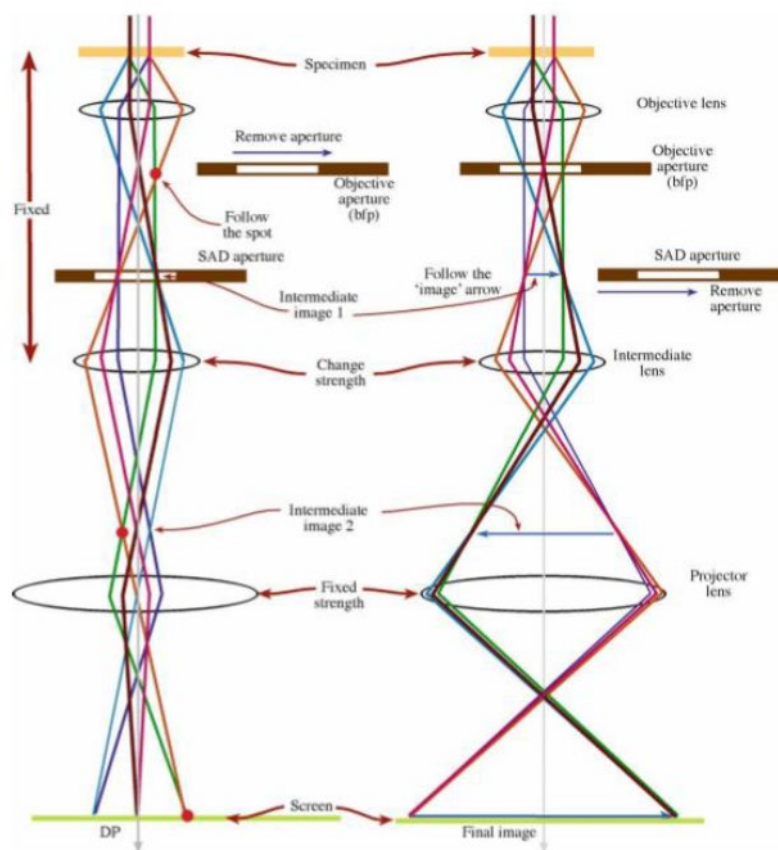


Figure 2.8 Two primary operation modes of TEM.[165]

2.4 Cell assembly

The coin cells are assembled inside a glovebox, which is filled with Ar atmosphere. The moisture level and oxygen level are kept under 0.1 ppm to prevent contamination of lithium

metal and electrolyte. For a coin cell, the lithium metal is used as anode which is cut into 1/2'' discs using a hand-held punch from lithium ribbon (Sigma Aldrich). These are further flattened before assembly. The separator for the battery is Celgard 2400, which are cut into size of 9/16''. The electrolyte used for the cell is 1M LiPF₆ in EC/DEC mixed solvent with molar ratio 1:1. To start the assembly, the thin film cathode is first placed and centered at the positive casing of the coin cell, after which 50 μ L of electrolyte is added on top of the cathode surface. Then the separator is placed onto the cathode followed by another 50 μ L of electrolyte. The lithium metal disc is then placed on top of that. It should be noted that both the cathode and anode need to be centered with respect to the casing position. Lastly, one stainless steel spacer and one spring are placed on top of the anode in order followed up by the negative casing. The negative casing is first pre-pressed to close the cell assembly by hand and is then put on to the crimper to fully seal the cell.

2.5 Electrochemical characterization

2.5.1 Galvanostatic charging

Galvanostatic charging, also known as constant current charging, is the most applied test method for batteries. During the test, a constant current is given to the cell and the voltage, as well as capacity, is monitored, which can be repeated for charge and discharge cycles by simply reversing the voltage. This method exhibits great advantage of obtaining dQ/dV curves, which is a differential capacity curve like cyclic voltammetry curve that helps identify the chemical reactions during the cycling process. However, dQ/dV curves have advantages over cyclic voltammetry in terms of constant over-potential, which is only available at very slow sweep rate for a cyclic voltammetry measurement.

2.5.2 Potentiostatic charging

Potentiostatic charging, also known as constant voltage charging, is a relatively simple testing method, and often a supplementary charging technique combined with galvanostatic charging. During the constant current charging, there will be certain charge build-up at electrode surfaces causing polarization and deteriorate the cell performance. Therefore, a charging program with initially constant current charging and a follow-up constant voltage charging toward the end of charging cycle can help give optimal capacity.

2.5.3 Cyclic Voltammetry

A sweeping potential with a constant scan rate is given to the cell and the responsive current is logged, which is repeatedly charging and discharging the cell to measure the anodic and cathodic current values and can provide information of redox reaction occurring during the cycling. The peak positions indicate the electrochemical potential where the redox reactions are occurring, and the difference between the cathodic and anodic peak can be used to analyze the reversibility of the electrochemical reaction. Further, the lithium ion diffusion rate can be evaluated by varying the sweep rate and compare the peak currents.

2.5.4 Electrochemical impedance spectroscopy

Electrochemical impedance spectroscopy (EIS), known as AC impedance spectroscopy, is a useful tool to model the battery and identify interfacial reactions in the battery. During a measurement, the current response is logged when an AC voltage signal is applied to the battery at different time constant. The Nyquist plot can be obtained by plotting the real portion versus the imaginary portion of the impedance.

2.5.5 Capacity

Capacity is a parameter to quantify the capability a battery can host charges or lithium ions for lithium ion batteries. The lithium is removed from the cathode during charging and inserted back into the cathode during the discharging. Generally, the capacity is normalized either with respect to weight (mAh/g) or volume (mAh/cm³) of the cell. Ideally, a battery with both high specific capacity as well as high volumetric capacity is preferred as it makes the battery light in weight and small. For thin film batteries specifically, mAh/cm²μm¹ is usually the reported unit for capacity due to the common micron-scale thickness.

2.5.6 Power

Power is a parameter that is used to evaluate how fast the battery can be charged or discharged without significant decrease of performance, which is limited intrinsically by the structural and kinetic limitations of internal components of a battery. In other words, the power will drop if the current draw from the battery exceeds the intrinsic rate limitation of the cell. To evaluate the power, rate capability tests can be carried out at different current density (or C-rate) and less the capacity decreases the better the power delivery ability of the battery.

2.5.7 Cycle life

Cycle life is a measurement of life cycles for a battery, which is a value of a number of cycles before the battery performance has been degraded to an unusable status under standardized cycling conditions. For a commercial battery, the cycle life is generally required to be over 2000 cycles.

2.5.8 Open circuit voltage (OCV)

Open circuit voltage is a measurement when there is no charge flow in the battery is occurring and the system is in equilibrium, which is directly related to Gibbs free energy. This parameter could be simple yet quick evaluation of the state electrodes, such as potential internal short, formation of solid electrolyte interphase, degradation of electrodes over cycling, etc.

3. $\text{LiNi}_{0.5}\text{Mn}_{0.3}\text{Co}_{0.2}\text{O}_2/\text{Au}$ NANOCOMPOSITE THIN FILM CATHODE WITH ENHANCED ELECTROCHEMICAL PROPERTIES

3.1 Overview

$\text{Li}(\text{Ni}_x\text{Mn}_y\text{Co}_{1-x-y})\text{O}_2$ (NMC) is considered as one of the most promising cathode materials for Li-ion batteries. Highly textured $\text{LiNi}_{0.5}\text{Mn}_{0.3}\text{Co}_{0.2}\text{O}_2$ (NMC532) thin films with well dispersed Au nanoparticles (~5 nm in average diameter) were deposited by pulsed laser deposition. Microstructure studies reveal the epitaxial nature of the Au nanoparticles and NMC matrix, and their lattice matching relationships. The Au nanoparticles are uniformly distributed and form faceted interfaces with NMC matrix. NMC with 2 at.% Au shows the highest volumetric capacity, best initial columbic efficiency, highest cycling performance, best rate capability and highest capacity retention among all the samples, due to alteration of chemical environment of transition metal while keeping high crystallinity. Moreover, the electrochemical impedance spectroscopy shows that the incorporation of the Au nanoparticles also reduces charge transfer resistance compared to the pure NMC. The results suggest that appropriate Au nanoparticle incorporation enhances the volumetric capacity and promotes the charge transfer process, and thus could lead to enhanced battery performance.

3.2 Introduction

$\text{Li}(\text{Ni}_x\text{Mn}_y\text{Co}_{1-x-y})\text{O}_2$ (NMC) is a promising cathode material and has received extensive attention in recent years because of its higher cutoff voltage, better structural stability and lower cost compared to the traditional LiCoO_2 . [36] NMC was first reported as a possible alternative to LiCoO_2 for cathode material in lithium ion batteries, by Ohzuku and Makimura. [170] Since then, much of the work has been done to explore their microstructural properties [171]–[173] and enhance their electrochemical performance [174]–[176]. One of the drawbacks of NMC cathodes

is that they experience the issue of low conductivity. One solution is to add excessive carbon black.[36] However, such approach will also significantly decrease the volumetric capacity because of the electrochemically inactive carbon black at higher potential.[36] Other efforts have been devoted to grain size reduction of the NMC cathodes to nanoscale[177] as well as thin carbon coating on the cathodes[178]. Further work is very much needed for NMC cathodes to address other issues such as low volumetric density, large interparticle resistance, and side reactions.[179], [180]

On the other hand, all-solid-state thin film batteries have attracted tremendous research interests in recent years, because of safety as well as numerous potential applications, such as implantable medical devices, remote sensors, power source for microelectronics, and CMOS-SRAM memory devices.[181]–[186] From the fundamental study point of view, thin film battery materials provide clean material systems for studying the intrinsic properties of materials and exploring novel nanostructures and material designs for enhanced electrochemical performances. For example, Dahn *et al.*[187] reported the first thin film LiCoO_2 cathode and later Bates *et al.*[188] demonstrated that preferred orientation strongly affected its electrochemical performance. Su *et al.*[175] applied a thin Al_2O_3 layer to improve the cycling performance by delaying interfacial reaction between NMC and electrolyte.

However, due to the absence of conductive additives, NMC cathodes in thin film form exhibit even lower conductivity than its bulk counterparts and thus result in larger charge transfer resistance in the cells.[189] Very limited work has been reported to overcome this issue for NMC thin film cathodes. For example, increased interfacial resistance has been observed in high temperature deposited NMC film, and the charge transfer contribution to the impedance was not fully understood.[190] Most reports on solving low conductivity issue focus on the LiFePO_4

systems by applying either Ag or C doping.[191]–[193] The work on thin film NMC composite approach is scarce.

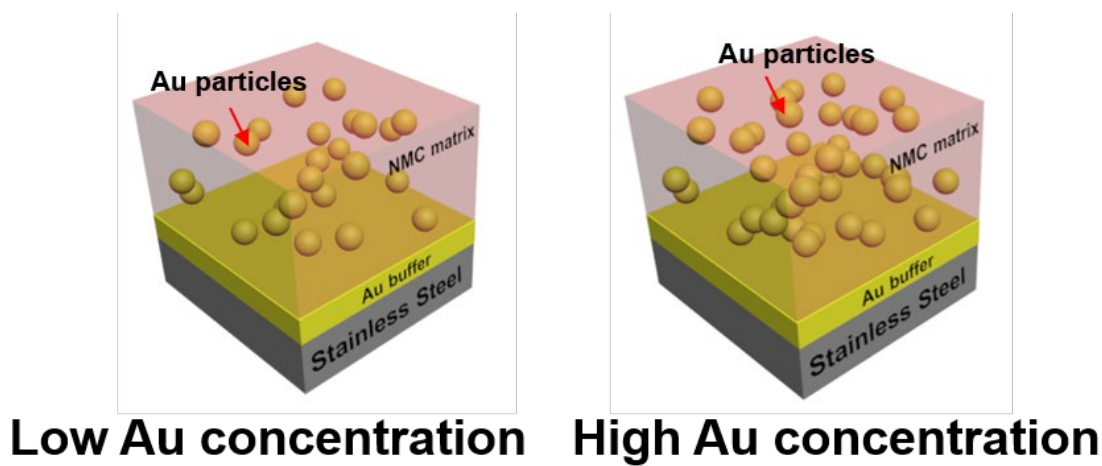


Figure 3.1 Scheme proposing that Au added into the matrix of NMC exists in the form of particles.

In this study, a new NMC/Au nanocomposite structure as thin film cathode has been demonstrated for the first time. The NMC-Au nanocomposites allow incorporating well dispersed Au nanoparticles in NMC matrix with the goal to facilitate the electrical and ionic charge transport process in NMC films. A pulsed laser deposition (PLD) technique was used for the film growth by using a composite target of NMC-Au. The proposed 3-D film morphology of the NMC-Au nanocomposite film is shown in Figure 3.1. With knowledge on prior metal/oxides systems,[194], [195] Au is selected for the demonstration because of its high stability upon oxidizing environment,[196] low alloy potential with lithium,[197] similar cubic close-packed structure[36] and good lattice matching between Au and NMC (e.g., $a_{\text{Au}(111)} (2.35 \text{ \AA})$ matches well with $a_{\text{NMC}(0006)} (2.37 \text{ \AA})$). It is also possible to tune the Au composition by changing the Au composition as illustrated in Figure 1. Further electrochemical studies including Cyclic Voltammetry measurement, charge-discharge cycling test, rate performance test and AC impedance are conducted to correlate with the microstructural characteristics of the NMC-Au nanocomposite

cathode.

3.3 Experimental

A NMC target was prepared by mixing NMC532 (MTI) powder with 15% Li₂CO₃ (Alfa Aesar) to compensate the possible Li loss during the sintering process. The target was pressed into a pellet and sintered at 900 °C with sufficient O₂ flow for 24 hrs. The films were deposited using a PLD system with a 248 nm KrF laser source at the laser frequency of 5 Hz and the laser energy of 1 J cm⁻². The depositions were under 750 °C with 10 mTorr oxygen partial pressure. The cooling rate was set at approximately 10 °C/min after deposition. The Au/NMC composite is achieved by a NMC-Au composite target. The target to substrate distance was set to be 4 cm for all depositions. Both polished stainless steel substrates with sputtered Au buffer layer and *c*-cut Al₂O₃ substrates were used in this study. X-ray diffraction (XRD, PANalytical Empyrean Diffractometer) system with a Cu Kα1 ($\lambda = 1.5406 \text{ \AA}$) source was used to characterize the crystalline characteristics of the samples. Transmission electron microscopy (TEM) and scanning transmission electron microscopy (STEM) (under high angle annular dark field, HAADF) were taken on a FEI TALOS 200X system with a point-to-point resolution of 1.2 Å and 1.6 Å for TEM and STEM modes, respectively. The CR2032 coin cell was assembled in an Ar flowed glovebox (Innovative technology, O₂<0.1ppm, H₂O<0.1ppm) with Li metal anode (Alfa Aesar) and Celgard 2400 separator. Potentiostatic impedance measurement was conducted on a Gamry Series G300 setup using the frequency range from 20 μHz to 20000 Hz at 3.7 V. Electrochemical measurements were conducted using an Arbin BTS2000 testing system. Charge-discharge cycling test was measured between the voltage range of 3.0 V -4.2 V for 50 cycles. Rate performance was tested at the current density of 7.8 μA/cm², 15.6 μA/cm², 39.0 μA/cm², 78.0 μA/cm², 117.2 μA/cm², respectively. There was a 5-minute relaxation time between each

different current density. The Cyclic Voltammetry was measured at a voltage ramp rate of 20 $\mu\text{V/s}$, 50 $\mu\text{V/s}$, 75 $\mu\text{V/s}$, 100 $\mu\text{V/s}$ and 200 $\mu\text{V/s}$.

3.4 Results and Discussion

Standard θ - 2θ XRD plots of the NMC films grown on both *c*-cut sapphire substrates and Au-buffered stainless steel (Au-SS) substrates with different compositions (2 at. % and 6 at. %) of Au are shown in Figure 3.2 (a), (b), respectively. Here, the Au-concentration was controlled by varying the Au composition in the composite target. The primary peaks of NMC (0003), (0006) and (0009) for all the samples with or without Au deposited on sapphire substrates suggest excellent out-of-plane texture of NMC along (000 l). For Au-NMC sample on sapphire substrate, there is a primary peak of metallic Au and a minor peak of Li_xAu alloy in Figure 3.2(a).[197] This suggests that Au content presents as mostly Au secondary phases and some Li_xAu alloys, instead of lattice substitutions in the NMC matrix. Furthermore, all NMC (000 l) peaks of NMC-Au show a shift to higher 2-theta angles in Figure 3.2(a), i.e., a smaller *c*-lattice parameter comparing to that of the pure NMC, indicating a compressive strain in the *c*-axis possibly introduced by the Au secondary phases. The full width half maximum (FWHM) of the Au-NMC films is slightly larger than that of the pure NMC, which is probably due to the decrease of grain size from the introduced Au secondary phases. The NMC films on Au-buffered SS substrate overall show similar results in Figure 3.2(b) as those on sapphire substrates, i.e., (1) highly (000 l) textured films in out-of-plane direction; (2) all NMC peaks in Au-NMC samples shift to larger angles compared to pure NMC; (3) the FWHM of NMC peaks broadens. All the films on Au-SS substrates show slightly lower texture and film crystallinity compared to the ones on sapphire substrates, which is reasonable considering the polycrystalline nature of the Au-SS substrates. In

addition, there is very minor NMC ($10\bar{1}7$) peak in Au-NMC films. Interestingly, there is no obvious Li_xAu peak observed for the Au-NMC on Au-SS samples.

The XRD pole figure analysis was conducted on all the Au-SS samples to explore the overall 3D texture of the NMC films with or without the Au secondary phases. Here NMC (0003) pole in Figure 3.2(a1) -3.2(a3) were obtained and analyzed using MTEX toolkit for pure NMC, 2 at. % Au-NMC, and 6 at. % Au-NMC, respectively. The main observations are: (1) 2 at% Au-NMC and pure NMC show very similar overall texture, i.e., highly textured around (0003) pole. Comparably, 6 at. % Au-NMC has very low texture compared to the other two films, which is probably due to the incorporation of the Au secondary phases in the film. It is noted that there are some background textures in all the pole figures due to the curvature of the SS substrate surface. Overall, the pole figure texture study gives a much better view on film crystallinity and texture for the samples on the curved Au-SS substrates and is consistent with the out of plane XRD measurement in Figure 3.2(a).

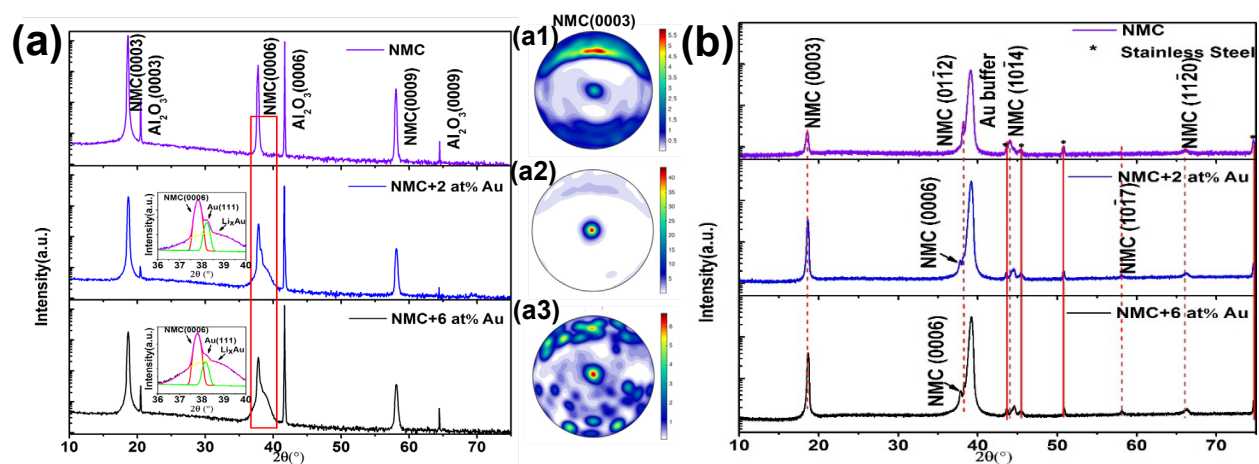


Figure 3.2 X-ray diffraction of as-deposit film on (a) Au buffered Stainless Steel substrate with pole figure of NMC (0003) pole of (a1) Pure NMC, (a2) 2 at% Au added NMC and (a3) 6 at% Au added NMC; (b) c-cut Al_2O_3 substrate with different gold particle percentage introduced to the NMC matrix.

To probe the morphology and distribution of the Au secondary phases in NMC films, plan-view and cross-section TEM/STEM analysis were conducted on all the Au-NMC films on sapphire substrates. Figure 3.3(a) and (b) show the low magnification TEM images taken from plan-view and cross-section TEM samples, respectively, for the 2 at. % Au-NMC film. In the meantime, SEM image of film morphology is shown as insert in Figure 3.3(a1) at the magnification of 50K. It shows the surface morphology of platelet shape, which is typical for NMC.[198] No Au nanoparticles can be obviously seen in the SEM image because of the small Au nanoparticles (~5 nm).

High density Au nanoparticles are well dispersed in the NMC matrix, which is also confirmed by EDX image shown in Figure 3.3(b1). The average diameter of the Au nanoparticles is around 5 nm and uniformly distributed throughout the entire film thickness, enhancing the electronic conductivity in the NMC film. In addition, Au particles tend to accumulate around grain boundaries as it is evidenced in Figure 3.3(a), which is possibly due to the high energy at the boundaries leading to preferential nucleation of gold crystals. Because of 3D nature of the cross-section TEM sample foils, the Au particle density in TEM images is estimated through the foil thickness and thus is overly estimated. The following density calculation is based on the low density values made at multiple regions using multiple plan-view and cross-section TEM images. The overall areal density of the Au nanoparticles is $5.4 \times 10^{11}/\text{cm}^2$ and volume density is $1.1 \times 10^{18}/\text{cm}^3$. To convert the Au density into atomic percent, the number of atoms of Au and NMC are estimated using atomic density in unit cell, which renders 0.92 at.% of Au doping in the overall nanocomposite film, lower than the expected concentration.

Based on the corresponding selected area electron diffraction (SAED) patterns in Figure 3.3(c) and (d), it is clear that NMC films grow highly epitaxial on sapphire substrates evidenced by the

distinguished diffraction dots for Al_2O_3 (connected by yellow lines), NMC (red lines) and Au (pink lines). The epitaxy matching relations are: (0006) Al_2O_3 // (0003) NMC// (111) Au and $(11\bar{2}0)$ Al_2O_3 // $(10\bar{1}\bar{4})$ NMC// (220) Au. The d -spacing of NMC (0003) is estimated to be 4.747 Å, which is consistent with the above XRD results. The corresponding lattice parameters for NMC in the 2 at. % Au sample can be calculated as $a = b = 2.863$ Å, and $c = 14.241$ Å. Comparing to bulk NMC lattice parameters,[199] it shows a compressive strain of 0.19 % in c -axis, and 0.36 % in a - and b -axis. Interestingly, in Figure 3.3(d), there are two sets of NMC diffractions as indicated by the set of green lines and the set of red lines. Both sets of the NMC diffractions are symmetric, which indicates the twinning structures of the NMC domains. The observation of the NMC twin structure is consistent with previous report on pure NMC films.[200] Moreover, the diffraction dots for Au (111) and NMC (0006) are overlapped, due to the similar d -spacing between the two. In addition, there are some minor diffraction dots with large d -spacing possibly from the Li_xAu compound, which is further discussed in the following section.

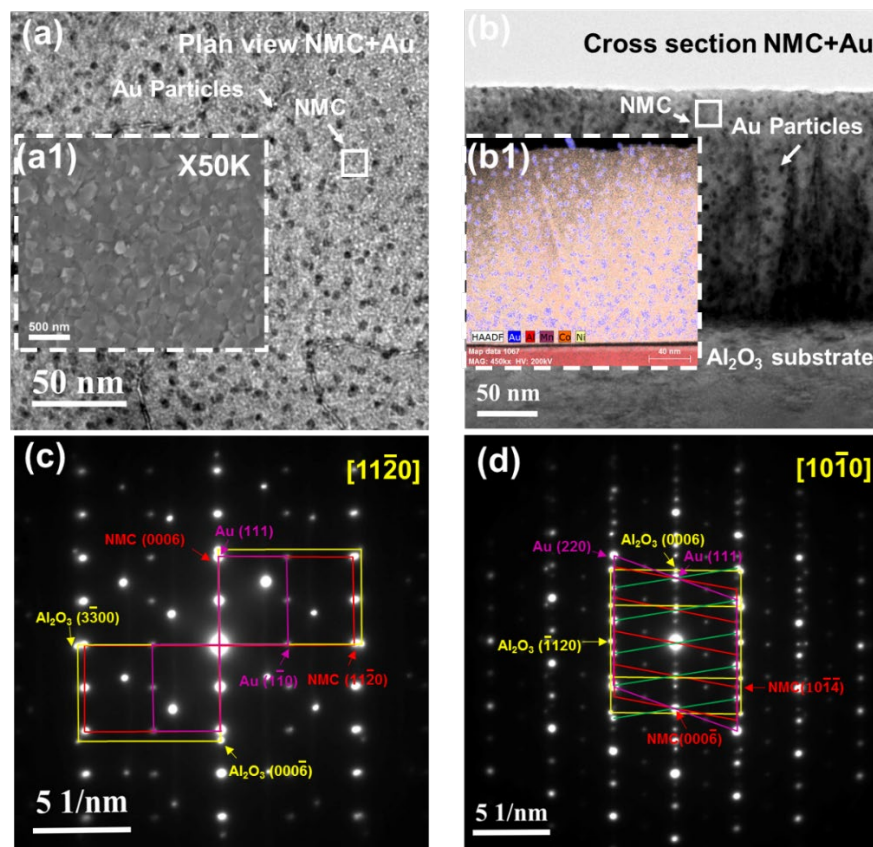


Figure 3.3 TEM images of 2 at. % Au NMC thin film on *c*-cut sapphire substrate: (a) low magnification plan-view and (a1) plan view SEM image of the film morphology; (b) low magnification cross-section showing the 3D nature of the Au nanoparticles being uniformly embedded into the NMC matrix and (b1) corresponding EDX mapping confirming the Au particles distribution; SAED pattern of NMC film from (c) Al_2O_3 $[11\bar{2}0]$ and (d) Al_2O_3 $[10\bar{1}0]$ zone axis.

Figure 3.4 shows a set of high resolution STEM images taken under HAADF condition (also called Z-contract imaging where the image contrast is approximately proportional to $\sim Z^2$) and their corresponding Fast Fourier Transformed (FFT) patterns. First, most of the Au particles are faceted and the ones with round edges could be resulted from multiple facets that are out of focus. Interestingly, some Au substitution regions were observed in the plan-view HAADF image shown in Figure 3.4(c), and Au atoms replaced some transition metal atoms in an alternating manner. The FFT of the NMC matrix, Au particle, and the substitution region has

been processed and shown in Figure 3.4(c1) –(c6), respectively. It is noted that Au occupies every other lattice in the NMC matrix, causing the new phase region with doubled d -spacing. In addition, these substitution regions seem to exist near the NMC domain boundary as shown.

Figure 3.4(a) and 3.4(b) present the matching relationship from Al_2O_3 $[10\bar{1}0]$ and $[11\bar{2}0]$ zone axis, respectively.

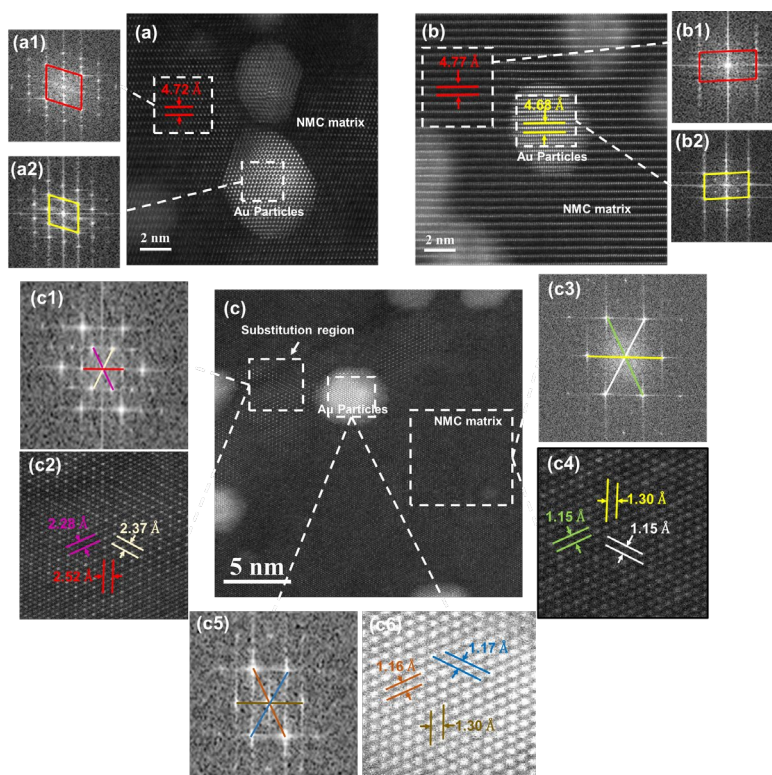


Figure 3.4 HAADF image of 2 at. % Au NMC film from (a) cross section of Al_2O_3 $[10\bar{1}0]$ and (b) $[11\bar{2}0]$ zone axis and (c) plan-view showing some Au substituted matrix region.

Au-NMC films as cathode were assembled in coin cell batteries and tested to explore the effects of Au on the overall electrochemical performance of the cathodes. The CV tests under different rates for the samples with different Au concentration are shown in Figure 3.5(a)(a1)(a2)(a3). It can be observed that the anodic peaks of $\text{Ni}^{2+}/\text{Ni}^{4+}$ for both Au-NMC samples are shifted to higher potential values as well as the shift of $\text{Ni}^{4+}/\text{Ni}^{2+}$ to lower potential values. However, extra peaks

are observed in between the redox pair of Ni. This may be because that the introduced Au/NMC interface changed the charge state of nearby ions by either substituting transition metal sites or fitting in the lithium layers, as evidenced by the microstructural study. Besides, pure NMC exhibits higher current for $\text{Ni}^{2+}/\text{Ni}^{4+}$ oxidation peak but a smaller $\text{Ni}^{4+}/\text{Ni}^{2+}$ peak than 2 at% Au-NMC, which suggests higher electrochemical activity of $\text{Ni}^{2+}/\text{Ni}^{4+}$ and lower reversibility of Ni redox reaction. This phenomenon can be possibly attributed to the alteration of chemical environment of Ni ions caused by Au addition, confirmed by the extra peaks in Figure 3.5(a2). However, 6 at% Au-NMC barely shows any electrochemical reaction, and it can be due to the structural disruption shown in the pole figure (Figure 3.2(a3)).

Charge-discharge tests were carried out for 50 cycles. The charge-discharge curves in Figure 3.5(b)(b1)(b2)(b3) show that the 2 at. % of Au-NMC sample obtains the highest volumetric capacity compared to both the pure NMC and 6 at. % Au-NMC composite, while the 6 at. % Au shows the lowest capacity. The reason for this phenomenon can be attributed to the formation of Li_xAu compound due to the addition of Au. In the 2 at. % Au sample, Li_xAu formed during deposition due to the excessive lithium in the target, which could contribute to the extra initial capacity compared to pure NMC. Higher capacity in later charge-discharge cycles is also a proof of the benefit introduced by Au nanoparticles in the system. The lower capacity of 6 at. % Au-NMC among all the samples, on the other hand, might be caused by the structural collapse triggered by the excess Au particles.

First cycle of cyclic voltammetry measurement for three different samples shown in Figure 3.5(c) reveals more information, where $\text{Mn}^{3+}/\text{Mn}^{4+}$ oxidation is observed in pure NMC. This confirms two points: 1) addition of Au does change the chemical environment of transition metal ions; 2) the fast capacity fade in Figure 3.5(b1) possibly arises from the dissolution of Mn

ions.[201] The rate performance of pure NMC and 2 at. % Au-NMC shows better rate capability and capacity retention of 2 at. % Au-NMC, as indicated in Figure 3.5(d), and 6 at. % Au-NMC is not of interest in this measurement due to low capacity. Further, the first several cycles show significant decay of capacity which is caused by the inhomogeneity due to naturally slow kinetics of (0003) oriented NMC.[202] Interestingly, the columbic efficiency ($C_{\text{discharge}}/C_{\text{charge}}$) is larger than 100% for high current density, which could possibly be related to the diffusion limitation discussed above, which is also proved by the abnormal columbic efficiency variation at each transition of current density.

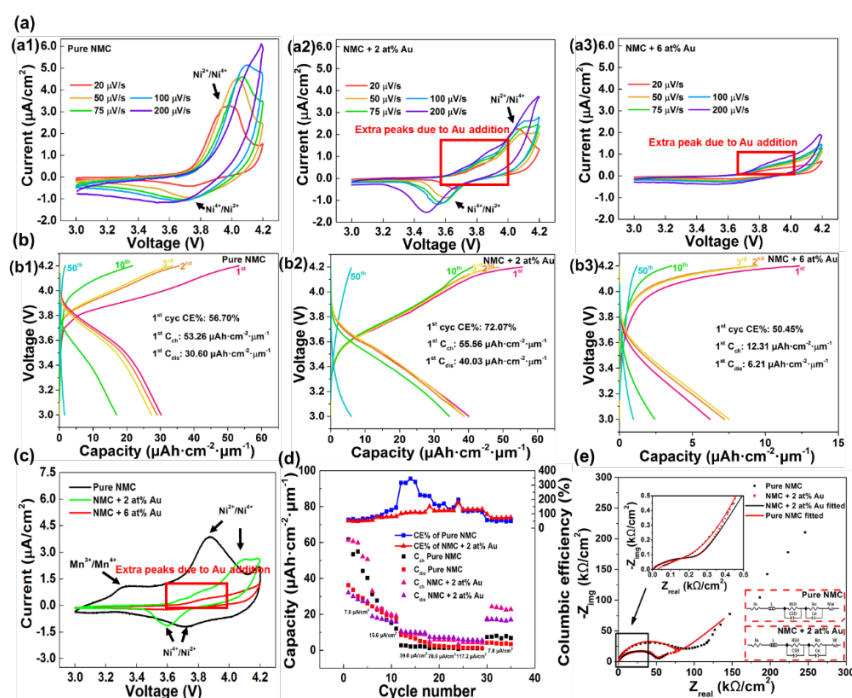


Figure 3.5 Electrochemical test of (a)(a1)(a2)(a3) cyclic voltammetry of different rate (20 $\mu\text{V/s}$, 50 $\mu\text{V/s}$, 75 $\mu\text{V/s}$, 100 $\mu\text{V/s}$ and 200 $\mu\text{V/s}$) for different Au concentration indicating addition of Au increase reversibility of the reaction by introducing extra peaks but excessive Au prevent redox reaction from occurring; (b)(b1)(b2)(b3) Cycling performance at 7.8 $\mu\text{A/cm}^2$ for different Au concentration showing moderate amount of Au has the best cyclability; (c) Initial CV cycle of three samples with different Au concentration indicating that Au can alter the valence state of transition metal ions; (d) Rate measurement at current density of 7.8 $\mu\text{A/cm}^2$, 15.6 $\mu\text{A/cm}^2$, 39.0 $\mu\text{A/cm}^2$, 78.0 $\mu\text{A/cm}^2$, 117.2 $\mu\text{A/cm}^2$ respectively showing better retention for 2 at% Au-NMC; (e) Nyquist plot of 2 at% Au-NMC and pure NMC at 3.7 V showing that addition of Au decreases the charge transfer resistance R_{ct} .

The smaller semicircle in the Nyquist plot for 2 at. % Au-NMC compared to pure NMC in Figure 3.5(e) suggests that the Au additions facilitate the overall charge transfer process, in which the Au nanoparticles exist as local current collectors and shorten the diffusion path of the electrons before interacting with Li atoms. It is also proved by the equivalent circuit indicated in Figure 3.5(e) as finite length Warburg element was used for fitting Au-NMC curve and infinite length Warburg was used for pure NMC. However, the Au-NMC also shows larger interfacial resistance, which is possibly introduced by the interfaces of Au/NMC.[190] Besides, it is worth noting that both fitting show much worse quality in the low frequency portion, which is possible due to the limited measurement capability in low frequency end (20 μ Hz) that introduces perturbation and inaccuracy. It is expected that, optimization on the Au nanoparticle density and distribution could further enhance the overall charge transfer process and electrochemical performance of the thin film batteries.

3.5 Conclusions

NMC/Au epitaxial composite thin films with different Au compositions were prepared using PLD and compared with pure NMC film. The epitaxy matching relationship between Au secondary phases and NMC matrix was explored. Excellent crystallinity and high quality epitaxy growth of the Au-NMC films were demonstrated by both XRD and TEM studies. Based on the electrochemical property measurements, the 2 at. % Au/NMC sample presents the best volumetric capacity and reversibility compared to pure NMC and 6 at. % Au/NMC. The enhancement is attributed to the enhanced electro-conductivity facilitated by the Au nanoparticles in the NMC matrix. Higher Au compositions could lead to lattice deterioration and lower the overall electrochemical performance. This study demonstrates a new approach incorporating metal/oxide nanocomposite structures as cathode for thin film lithium ion batteries.

4. Li_2MnO_3 THIN FILMS WITH TILTED DOMAIN STRUCTURE AS CATHODE FOR LI-ION BATTERIES

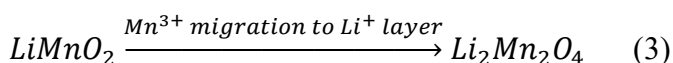
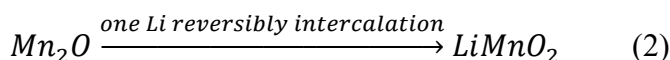
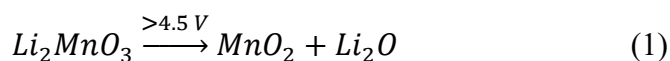
4.1 Overview

Li_2MnO_3 thin film cathodes with tilted domain morphology have been synthesized by a simple one-step oblique-angle deposition (OAD) method using pulsed laser deposition (PLD). The cathode thin films with tilted domains show significantly improved kinetics than the conventional planar form of Li_2MnO_3 thin film, which is attributed to the facilitated Li-ion intercalation paths in the tilted domains. The OAD grown Li_2MnO_3 decreases the cathode-electrolyte interphase thickness as evidenced by TEM and XPS data. The cathode with the tilted domains in the coin cell battery can be continuously cycled for 100 times while the conventional planar Li_2MnO_3 failed after 9 cycles. In the electrochemical window of 2.0V-4.8V, the tilted Li_2MnO_3 demonstrates first cycle capacity of $99.5 \mu\text{Ah}\cdot\text{cm}^{-2}\cdot\mu\text{m}^{-1}$ with about 80% capacity retention after 100 cycles. This demonstration on morphology tuning in thin film cathode suggests enormous potential in thin film cathode designs towards future high efficiency thin film Li-ion batteries.

4.2 Introduction

Li_2MnO_3 is considered as one of the most promising cathode material candidates for Li-ion batteries because of the cheap and abundant Manganese (Mn) element and the very high theoretical capacity of 459mAh g^{-1} . [203] However, Li_2MnO_3 was usually considered as electrochemically inactive and was used in Li-rich cathode materials for structure stability, [70] because of the unlikely oxidation of Mn^{4+} to Mn^{5+} in octahedral sites. [204] Interestingly, it has

been proven achievable as an active cathode material by several experimental reports. The generally accepted reaction mechanisms can be summarized in the reaction Equations (1)-(3), which indicates that it will experience gradual “layer-to-spinel” phase transformation upon cycling.[205]



Li_2MnO_3 cathode systems with different particle morphologies were reported as a primary approach for enhancing its electrochemical activity. For example, Amalraj *et al.* studied size dependence of Li_2MnO_3 particles and showed the improved electrochemical performance of nano-sized particles than micro-sized particles due to lowered impedance and shortened lithium diffusion length.[203] Vendra *et al.* synthesized Li_2MnO_3 nanowires with average diameter of 50 nm and showed improved columbic efficiency.[78] However, these reports all suggest significant kinetic problems due to its insulating nature, such as low cycle rates, slow activation, and increased capacity upon cycling.

Furthermore, very limited work has been performed on thin film battery of Li_2MnO_3 despite the importance of thin film battery in many application fields.[72], [206], [207] Zheng *et al.* reported the growth of planar dense Li_2MnO_3 thin film using pulsed laser deposition method, however the electrochemical performance was poor due to the limited film conductivity.[208] Taminato *et al.* studied thickness contribution to electrochemical performance. But the high capacity performance was only achieved in very thin films as thin as 12 nm, which limit the total energy capacity of the cell.[77], [209], [210]

Overall it is challenging to meet energy density requirement ($\sim 2 \text{ J mm}^{-3}$) from limited areal

footprint using the conventional planar thin film batteries.[211] Three-dimensional (3D) battery designs can be a potential solution as they provide higher energy density as well as higher power density with the increased surface area and decreased ion diffusion and electron harvesting pathways.[212]–[214] Examples include integration of porous Fe_3O_4 nanoflakes on cone-shaped Cu substrate by two-step chemical and electrochemical deposition,[215] micro-sized $\text{MnO}_2/\text{C}/\text{TiN}/\text{Si}$ pillar arrays through Deep Reactive Ion Etching[216] and others^[18–23]. However, no such 3D battery work has been done on Li_2MnO_3 cathode in thin film form.

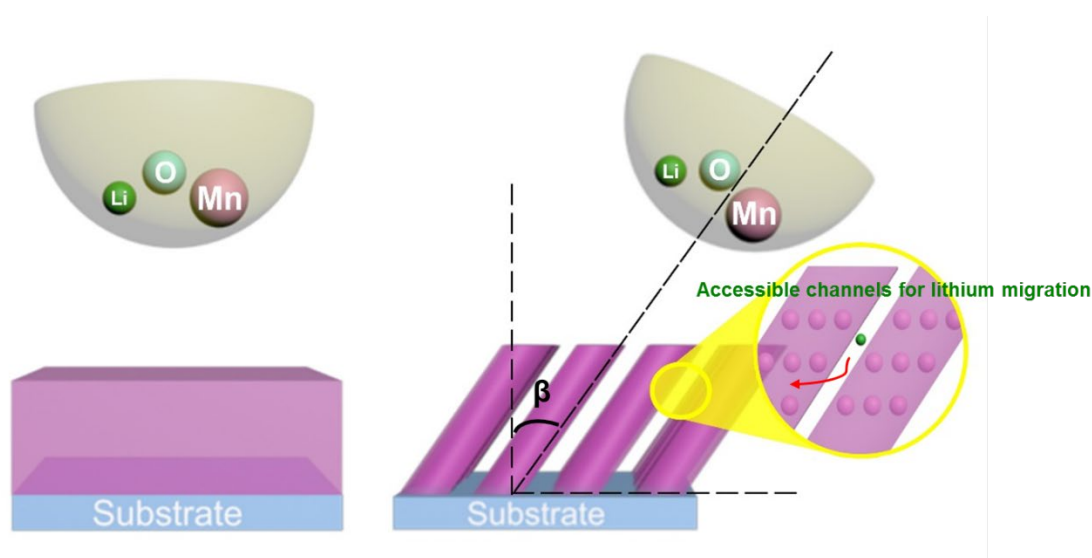


Figure 4.1 Schematic drawing showing the different substrate growth configuration of conventional pulsed laser deposition and pulsed laser oblique angle deposition.

In this report, the Li_2MnO_3 thin film cathode with a unique columnar grain morphology has been obtained by oblique-angle deposition (OAD) using pulsed laser deposition (PLD) and the schematic configuration of OAD is shown in Figure 4.1. This technique was widely applied to achieved porous thin film structures because of introduced shadowing effect.[222] The reasons for achieving this tilted grain geometry is to improve the kinetics of the cell in two aspects: 1) the introduced porosity will enhance the wetting of electrolyte in cathode and increase total ionic

conductivity; 2) the reduced dimension along in-plane direction can shorten ion diffusion pathways, which are supposed to suppress the cathode/electrolyte interface formation and thus the battery performance can be improved. The conventional Li_2MnO_3 cathode with planar geometry was also synthesized and compared with the tilted grain morphology to demonstrate the superior electrochemical performance from the three-dimensional geometry.

4.3 Experimental

Li_2MnO_3 (Pfaltz & Bauer) powder was mixed with 15% Li_2CO_3 (Alfa Aesar), milled in a high energy ball mill for 1 hr, decomposed in flowing Ar at 350 °C, pressed into a pellet, and sintered at 900 °C under O_2 atmosphere for 24hrs. The additional Li_2CO_3 was used as the easy vaporization of Li at elevated temperature. Pulsed laser deposition system (Lambda Physik Compex Pro 205, 248 nm KrF) were used to grow the designed thin film using oblique angle configuration schemed in Figure 4.1. The growth parameters are following: laser frequency 10 Hz, energy density 2.5 J cm^{-2} , O_2 atmosphere pressure 50 mTorr, deposition temperature 750 °C, cooling rate 10 °C/min under 15 Torr O_2 , plume to substrate angle 60°, target to substrate distance 5 cm. Both sputtered Au buffer layer coated polished stainless steel substrates (Au-SS) and *c*-cut Al_2O_3 substrates were used in this study. The tilted grown samples and non-tilt samples are represented as tilted LMO and non-tilted LMO in the rest of the text for easy representation. X-ray diffraction (XRD) was performed using PANalytical Empyrean Diffractometer system with a Cu $\text{K}\alpha_1$ ($\lambda = 1.5406 \text{ \AA}$) source. FEI TALOS 200X system is used to take Transmission electron microscopy (TEM) and scanning transmission electron microscopy (STEM) (under high angle annular dark field, HAADF) images. Ar filled glovebox (MBraun, $\text{O}_2 < 0.1 \text{ ppm}$, $\text{H}_2\text{O} < 0.1 \text{ ppm}$) was used to assemble CR2032 coin cell. Li metal anode (Alfa Aesar), Celgard 2400 separator, and 1M LiPF_6 in EC:DEC organic electrolyte were used for the cell. The film

thickness is about 150 nm-160 nm, substrate area is 0.64 cm^2 , the density can be estimated to be single crystalline Li_2MnO_3 3.71 g/cm^3 due to the high crystallinity nature of the films, and these lead to loading mass about $3.56 \times 10^{-2} \text{ mg}$ to $3.80 \times 10^{-2} \text{ mg}$. XPS measurement was conducted on cycled cathode using Kratos AXIS Ultra DLD Imaging X-ray Photoelectron Spectrometer (XPS). Arbin BTS2000 testing system was used for all the electrochemical tests. Charge-discharge cycling test was measured first under constant current of $5 \mu\text{A/cm}^2$ between the voltage range of 2.0 V - 4.8 V and then kept under constant voltage until the current decreased to $1 \mu\text{A}$. A step-wise rate performance was tested at between $5 \mu\text{A/cm}^2$ - $80 \mu\text{A/cm}^2$, the current density is doubled at each step. The Cyclic Voltammetry (CV) was measured at potential sweep rate from $10 \mu\text{V/s}$ to $200 \mu\text{V/s}$, more details can be found in the discussion. Gamry Series G300 potentiostat was applied to measure the electrochemical impedance spectroscopy. Frequency range was set $300 \mu\text{Hz}$ to 30000 Hz . The cell was charged to and kept at 4 V for 2hrs before performed the measurement.

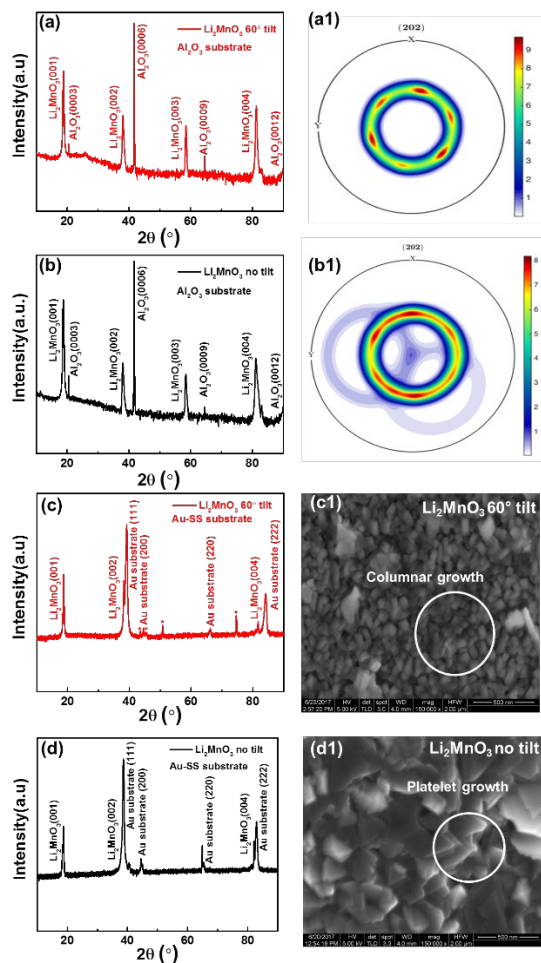


Figure 4.2 Out of plane X-ray profile of (a) oblique grow Li_2MnO_3 and (a1) (202) pole figure of Li_2MnO_3 on Al_2O_3 substrate; (b) non-tilt Li_2MnO_3 and (b1) (202) pole figure of Li_2MnO_3 on Al_2O_3 substrate, where comparison shows nearly identical crystallographic orientation of the different configuration. Out of plane X-ray profile of (c) oblique grow Li_2MnO_3 and (c1) SEM morphology scan of Li_2MnO_3 on Au-SS substrate; (d) non-tilt Li_2MnO_3 and (d1) SEM morphology scan of Li_2MnO_3 on Au-SS substrate, where it still exhibits same crystallographic orientation but largely different surface morphology.

4.4 Results and discussion

Out of plane theta-2theta XRD patterns on $\alpha\text{-Al}_2\text{O}_3$ and Au buffered stainless steel (SS) for both tilted LMO and non-tilted LMO films are shown in Figure 4.2 (a)-(d). Interestingly, the growth configuration only affects the film morphology but barely alter the crystallographic relationship between film and substrate. For the films grown on $\alpha\text{-Al}_2\text{O}_3$ (0001), the d -spacing

for Li_2MnO_3 (001) are calculated to be 4.7168 Å and 4.7290 Å for the tilted LMO and non-tilt LMO, respectively. XRD pole figure data of Li_2MnO_3 (202) analyzed by MTEX toolkit are presented in Figure 4.2(a1) and 4.2(b1), which indicates the crystallographic orientation were not affected by the introduced growth configuration. The out of plane θ - 2θ XRD with Li_2MnO_3 on Au-SS substrates are plotted in Figure 4.2(c)-(d), which also exhibits very similar pattern for tilted LMO and non-tilted LMO samples, and d -spacing for Li_2MnO_3 (001) are calculated to be 4.7319 Å for tilted LMO and 4.7345 Å for non-tilted LMO, which are both larger than the films grown on Al_2O_3 (0001) substrates and smaller than the bulk value of 4.7416 Å.[223] Both tilted and non-tilted film don't show the characteristic superlattice peak because they exhibit preferred Li_2MnO_3 (001) orientation in the out-of-plane direction.¹⁰ The SEM micrographs of corresponding samples showing in Figure 4.2(c1) and 4.2(d1) indicate the obvious difference in surface morphology due to the different growth configurations, where the tilted configuration introduced columnar grains and non-tilt configuration led to expected platelet morphology for layered cathode materials similar to prior report.[198]

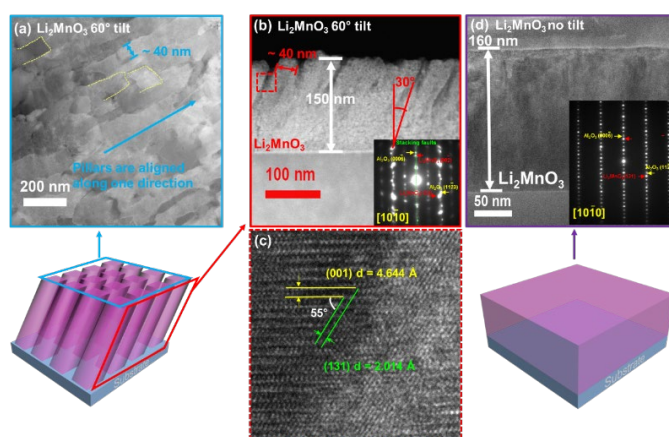


Figure 4.3 Low magnification STEM images of (a) plan view perspective of and (b) cross sectional perspective of oblique grow Li_2MnO_3 , the inset shows the corresponding SAED from Al_2O_3 $[10\bar{1}0]$ zone axis. (c) high resolution TEM of pillar interface squared out in (b) and the cleavage plane is measured to be Li_2MnO_3 (131). (d) cross sectional perspective of non-tilt Li_2MnO_3 and the selected area diffraction pattern of non-tilt Li_2MnO_3 from Al_2O_3 $[10\bar{1}0]$ zone axis is shown in the inset.

To further study the morphology and crystallographic relationship of the tilted LMO, plan-view and cross-section TEM/STEM analysis were performed and presented in Figure 4.3. Figure 4.3(a) and 4.3(b) are the low magnification plan-view and cross-sectional STEM images of the sample, as indicated in the schematic drawing, which show that the film was grown as tilted and well aligned pillars. The pillar size can be estimated to be ~ 40 nm in width with an average 5 nm interspacing between pillars. In short, the formation of the gaps is resulted from the shadowing effect during the OAD and limited adatom surface diffusion.[224] It has been reported that the dimension of columns and intercolumnar spacing could be adjusted depending on the growth temperature, growth rate, substrate-to-source distance and tilting angle.[225] The growth parameters are optimized based on previous experience for better electrochemical performance.[162], [164], [226] The pillar tilting angle β is measured to be around 30° , which matches with the zenithal evaporation angle but doesn't follow the classical expression.[225] The detailed crystallographic match relationships between the Li_2MnO_3 and Al_2O_3 are shown in the inset of Figure 4.3(b), the selected area electron diffraction (SAED) pattern from Al_2O_3 $[10\bar{1}0]$ zone axis indicates the clear matching of $\text{Li}_2\text{MnO}_3(002)//\text{Al}_2\text{O}_3(0006)$ in the out of plane direction. The broadened in-plane diffraction dots of the tilted LMO film exhibit the reduced column diameters as well as the increased defects density, which is consistent with the TEM images observed. Moreover, the blurred streaks along the (001) planes represents the high density stacking faults in the tilted LMO which is consistent with a prior report.[227] These high density stacking faults can provide reaction points for Li intercalation.[79] The High Resolution Transmission Electron Microscopy (HRTEM) image from the squared area in Figure 4.3(b) is presented in Figure 4.3(c), where the oblique plane was confirmed as $\text{Li}_2\text{MnO}_3(131)$ (d -spacing = 4.644 \AA), which makes the pillar tilt angle to be $\beta = 35^\circ$ based on the angle between Li_2MnO_3

(002) and (131). For comparison, the TEM image of the non-tilted LMO film on Al₂O₃ is shown in Figure 4.3(d), where it doesn't show any similar columnar morphology. Besides, the diffraction pattern indicates very similar crystallographic matching relationship as that of the tilted LMO in Figure 4.3(b) where similar dots representing stacking faults can be observed, which indicates that only film morphology was affected by different substrate configuration.

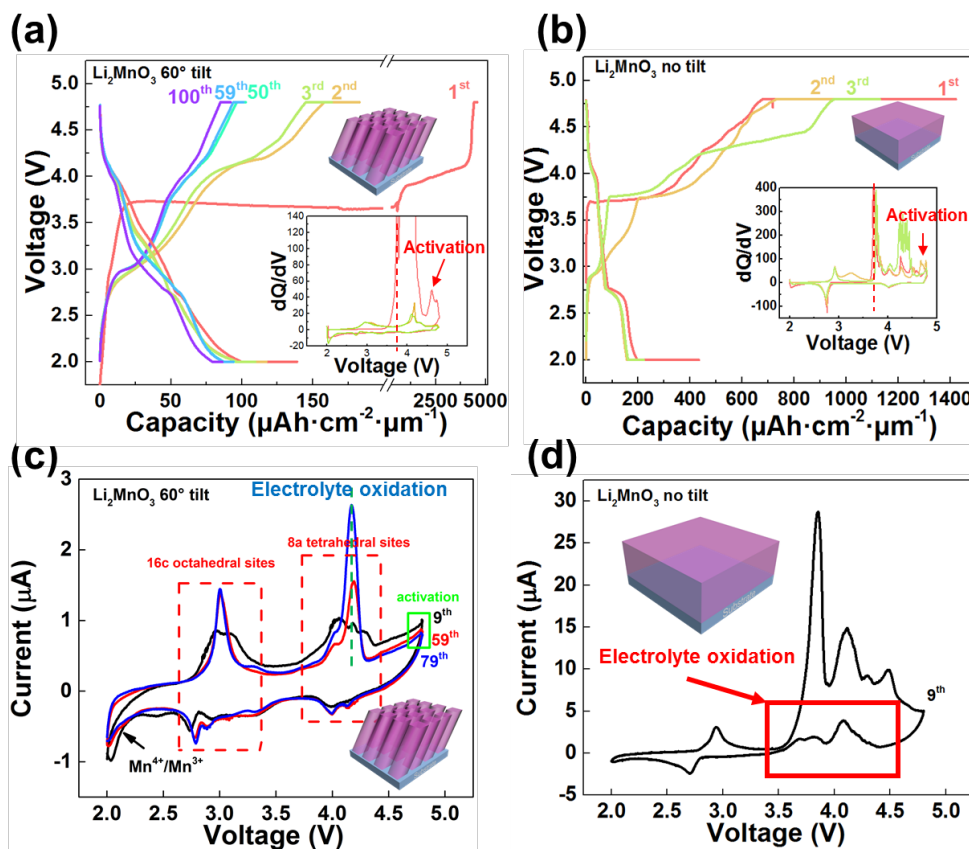


Figure 4.4 Cycling performance test of (a) oblique grow Li₂MnO₃ at 5 μA/cm² for 100 cycles, the inset is the dQ/dV plot for the first three cycles; (b) non-tilt Li₂MnO₃ at 5 μA/cm² for 3 cycles, the inset is the dQ/dV plot for the first three cycles. Cyclic voltammetry of (c) oblique grow Li₂MnO₃ with potential sweep rate of 20 μV/s at 9th, 59th, and 79th cycles showing homogenization through cycling; (d) non-tilt Li₂MnO₃ with potential sweep rate of 20 μA/s at 9th exhibiting cathodic-type behavior on both sweep directions.

Electrochemical measurements were performed on both samples and the titled LMO shows superior electrochemical performance than that of the non-tilt LMO, and both films demonstrate

a layered-to-spinel transformation process that matches the mechanism mentioned in the introduction. First, from the cycling result in Figure 4.4(a) where estimated C-rate is 0.5C, tilted LMO achieves $138.79 \mu\text{Ah}\cdot\text{cm}^{-2}\cdot\mu\text{m}^{-1}$ total discharge capacity and $99.5 \mu\text{Ah}\cdot\text{cm}^{-2}\cdot\mu\text{m}^{-1}$ from constant current discharge for the first cycle, which is much higher than the reported value.[208] Furthermore, it still obtains $86.24 \mu\text{Ah}\cdot\text{cm}^{-2}\cdot\mu\text{m}^{-1}$ in total discharge capacity and $79.24 \mu\text{Ah}\cdot\text{cm}^{-2}\cdot\mu\text{m}^{-1}$ from constant current discharge part for the 100th cycle, which leads to a 62.1% capacity retention of total capacity and 79.6% of constant current discharge. As to non-tilt LMO, though it presents a higher capacity, the constant current charge capacity portion gradually increased from the 1st to the 3rd cycle, which is possibly due to the slow kinetics caused by rearrangement of Mn and O atoms.[208] Besides, the non-tilt LMO cell electrochemically failed at 10th cycle, as shown in Figure 4.4(b), the 10th charge cycle cannot reach 4.8 V even after long cycling time. Further, the coulombic efficiency of the non-tilt LMO is around 20-25% for the first three cycles, which further proves the limited electrochemical performance of the planar LMO films. It is noted that, both tilted and non-tilted LMO show the very large charge capacity that exceeds the theoretical value, which was also reported in other thin film electrode related literatures.^{12,35} This very large capacity is a commonly observed behavior and could be due to the electrolyte decomposition at thin film surface states[228] and structural accommodation through defects movement[210]. Overall the above result indicates an increase of cell kinetics because of the decreased in-plane lithium diffusion dimension and availability of electrolyte mixing in gaps of tilted LMO film compared to the non-tilt LMO. The dQ/dV curves of the first three cycles are plot for tilted LMO and non-tilt LMO in the inset of Figure 4.4(a) and 4.4(b). Both sample shows a peak around 3.7V, which could be attributed to the diffusion limitation due to the thin film nature.[164] However, this is only observed in the first cycle for tilted LMO but consistently

exists in non-tilt LMO even after the first cycle. The high intensity of the peak around 4V in tilted LMO in the first cycle indicates a full layer-to-spinel transformation due to fast kinetics. This peak has rather random intensity from the 1st to the 3rd cycle.[70] The peak around 4.2 V has several possible reasons. It could possibly be electrolyte oxidation based on Figure S3. It could also be a shoulder peak due to different local composition.[229] The peak at voltage > 4.5 V indicating by red arrow corresponds to the irreversible activation of Li_2MnO_3 due to oxygen evolution, which was reported in prior literatures.[34] Different from tilted LMO, non-tilt LMO shows multiple peaks at voltage > 4.5 V even after the first cycle, marked by red arrows, meaning the incomplete activation due to inhomogeneity and slow kinetics.

In Figure 4.4(c) and 4.4(d), the cyclic voltammetry (CV) measurements were conducted at the 9th, 59th, and 79th cycle for tilted LMO and at 9th cycle only for non-tilt LMO as it fails at 10th cycle. The general feature shows a typical spinel-type reaction where the redox pairs around 4.0V and 3.0V are corresponding to lithium reaction at $8a$ tetrahedral sites and $16c$ octahedral from spinel phase.[229]–[231] Regarding TLMO film, the small peak around 4.7V still represents partial loss of lattice oxygen due to lithium extraction, and the peaks around 2.0V are attributed to the spinel redox reaction of $\text{Mn}^{4+}/\text{Mn}^{3+}$ pair. Shoulder peaks are due to the different local composition as discussed previously. The increased intensity and sharpening of these peaks from 9th cycle to 59th cycle is due to the homogenization upon cycling. However, the peak at 4.2V with abnormally high intensity is due to the gradual electrolyte decomposition as evidenced in Figure S3. Figure S3 shows a CV measurement on a blank Au-SS with no loaded cathode materials. Peaks with high positive intensity can be observed between 3.4V to 4.2V in both forward and backward sweep directions. This can be explained by the electrolyte decomposition at the substrate surface because of the increased potential from surface states effect. To further

validate this statement, it can be observed in Figure 4.4(d) this phenomenon was overly exaggerated in the non-tilt LMO film based on the emergence “oxidation” anodic peaks in the backward sweep direction. Therefore, it can naturally lead to a conclusion that the Cathode Electrolyte Interphase (CEI) layer for the non-tilt LMO could be much thicker than that of the tilted LMO.

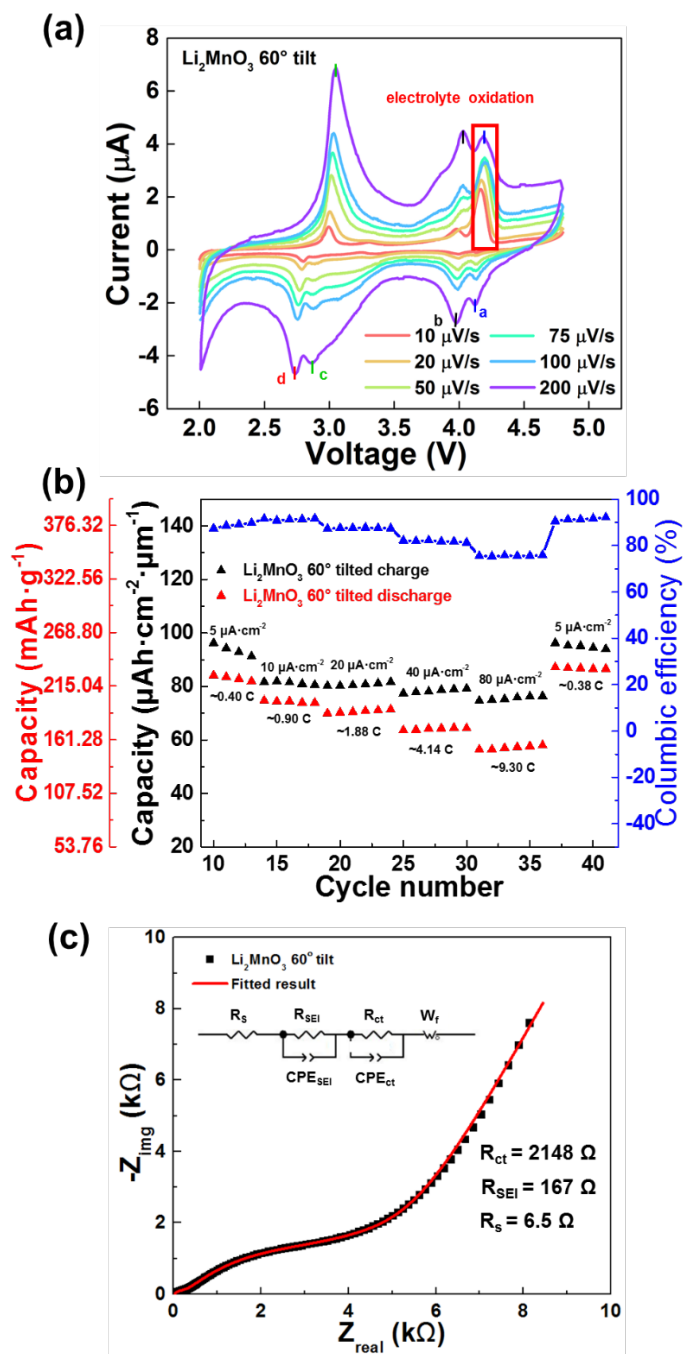


Figure 4.5 (a) Cyclic voltammograms of oblique grown Li_2MnO_3 on different potential sweep rates of 10 $\mu\text{V/s}$, 20 $\mu\text{V/s}$, 50 $\mu\text{V/s}$, 75 $\mu\text{V/s}$, 100 $\mu\text{V/s}$, and 200 $\mu\text{V/s}$ with labeled major redox reactions "a", "b", "c", and "d"; (b) C-rate performance test at current density of 5 $\mu\text{A}/\text{cm}^2$, 10 $\mu\text{A}/\text{cm}^2$, 20 $\mu\text{A}/\text{cm}^2$, 40 $\mu\text{A}/\text{cm}^2$, 80 $\mu\text{A}/\text{cm}^2$ respectively with calculated coulombic efficiency and estimated C-rate value; (c) fitted electrochemical impedance spectrum data of oblique grown Li_2MnO_3 with scheme indicating the equivalent circuit for the fitting.

More electrochemical performance measurements are presented in Figure 4.5 to evaluate the kinetical aspect of tilted LMO. The cyclic voltammetry curves measured at potential scan rate from 10 $\mu\text{V/s}$ to 200 $\mu\text{V/s}$ are shown in Figure 4.5(a). The representation of the redox pair peaks is already discussed in above mentioned section, and the anodic peak at around 4.2 V can be attributed to the electrolyte decomposition as discussed. It means the process is not diffusion controlled, but rather an accumulation-consumption based reaction. This shows the kinetics of tilted LMO was improved by the tilted pillar geometry as the scan rate value is quite typical for thin film battery.[164] The rate capability test is represented in Figure 4.5(b) and shows the capacity of 84.17 $\mu\text{Ah}\cdot\text{cm}^{-2}\cdot\mu\text{m}^{-1}$ (226.25 $\text{mAh}\cdot\text{g}^{-1}$), 73.94 $\mu\text{Ah}\cdot\text{cm}^{-2}\cdot\mu\text{m}^{-1}$ (198.75 $\text{mAh}\cdot\text{g}^{-1}$), 71.41 $\mu\text{Ah}\cdot\text{cm}^{-2}\cdot\mu\text{m}^{-1}$ (191.95.25 $\text{mAh}\cdot\text{g}^{-1}$), 64.42 $\mu\text{Ah}\cdot\text{cm}^{-2}\cdot\mu\text{m}^{-1}$ (173.16 $\text{mAh}\cdot\text{g}^{-1}$) and 58.01 $\mu\text{Ah}\cdot\text{cm}^{-2}\cdot\mu\text{m}^{-1}$ (155.93 $\text{mAh}\cdot\text{g}^{-1}$) at the estimated C-rate of 0.40 C, 0.90 C, 1.88 C, 4.14 C, and 9.30 C, respectively. To show that the tilted LMO has superior rate performance, the results are compared with reported value. Vendra *et al.* reported a slightly higher capacity retention at high C-rate however with lower capacity.[78] Taminto *et al.* reported higher capacity value at similar C-rate only when the thickness is very thin (12.6nm).[77] Lim *et al.* reported both lower capacity and capacity retention.[232] The capacity returns to 86.65 $\mu\text{Ah}\cdot\text{cm}^{-2}\cdot\mu\text{m}^{-1}$ (0.38 C) at the end of step-wise rate measurement. The slightly increased capacity should be from increased reaction depth thus slightly more phase transformation,[77] however this phenomenon is not significant as most film finished layer-to-spinel transformation in the first cycle. It is important for Li ion battery cathode to have high capacity retention when cycled at high C-rate, and the excellent capacity retention at high C-rate of the tilted LMO demonstrate potential application for thick thin film electrode.[78] Although the cell kinetics were improved by the tilted grain morphology as it provides more lithium pathways, it is worth noting that the relatively large decrease in

coulombic efficiency can be observed with increased current density. This can be possibly attributed to the surface states introduced by the columnar morphology. Therefore, the next step will be focusing on solving this problem. Several possible solutions could be to introduce conductive carbon coatings and graphene into the cathode materials.[233], [234] The EIS was also measured at an OCV of ~ 4.0 V, and the Nyquist plot is shown in Figure 4.5(c). The data was fitted with the equivalent circuit illustrated in the figure, and the charge transfer resistance R_{ct} based on fitted data equals to 2148Ω with solid electrolyte interface resistance R_{SEI} of 167Ω .

4.5 Conclusion

Unique tilted pillar morphology in Li_2MnO_3 thin film cathode was demonstrated by simple and effective OAD in PLD. Tilted grains with porosity in the tilted Li_2MnO_3 thin film cathode are demonstrated and significantly promote the kinetics of Li intercalation process compared to that of cathode prepared by conventional PLD method. Specifically, a high capacity of Li_2MnO_3 and high rate performance has been achieved in this tilted pillar geometry in Li_2MnO_3 thin film cathode, which enabled the practical application of Li_2MnO_3 thin film cathode in Li-ion batteries. The tilted pillar geometry can be further tuned for enhancing electrochemical performance and can be adopted in many other thin film cathodes beyond Li_2MnO_3 . Furthermore, this tilted pillar morphology with gaps grants the future potential of integrating the solid state electrolyte with thin film cathodes towards the all-solid-state thin film batteries using the simple sequential thin film deposition method.

5. Li_2MnO_3 CATHODE THIN FILMS WITH TILTED Au NANOPILLARS AS EFFECTIVE CURRENT COLLECTORS FOR LI-ION BATTERY APPLICATION

5.1 Overview

Novel Li_2MnO_3 (LMO)-Au nanocomposite thin film with tilted Au pillars are synthesized by an oblique angle deposition technique (OAD) in pulsed laser deposition. The pillar tilt angle and pillar dimension can be tuned by varying the inclination angle of the incoming flux and the growth rate. The obtained LMO-nanocomposite structure exhibits a volumetric discharge capacity of $35.78 \mu\text{Ah}\cdot\text{cm}^{-2}\cdot\mu\text{m}^{-1}$ for the 1st cycle but $62.32 \mu\text{Ah}\cdot\text{cm}^{-2}\cdot\mu\text{m}^{-1}$ at 100th cycle, which is attributed to significantly increased reaction depth upon cycling, indicating that Au pillars function as effective current collectors to facilitate full activation. In addition, the LMO-Au nanocomposites display highly anisotropic optical complex dielectric function in plane and out-of-plane, reduced bandgap, and high hardness of 10 GPa, nearly doubling that in pure Li_2MnO_3 . This study presents a novel approach for processing nanocomposite thin films with tunable tilted current collectors towards advanced thin film batteries, nanoscale plasmonic systems and other oxide-metal electrochemical systems.

5.2 Introduction

Significant researches have been focused on lithium ion battery as it is one of the most promising energy storage method. During cycling process, the electrode experiences repeated volume changes due to lithiation/delithiation and can finally lead to cracking and mechanical failure,[235] especially in two phase system like $\text{FePO}_4/\text{LiFePO}_4$.[94], [236] Many efforts were devoted to solve this problem, which were, however, mainly limited to surface coating and

elemental doping techniques,[237]–[241] though some recent simulation result shows the grain boundaries engineering can also be beneficial to stress alleviation.[242]

Different from the current solutions, vertical aligned nanocomposite can be one promising method and it introduces vertical domains in the matrix body, which are known to accommodate strain relaxation.[243] Vertical Aligned Nanocomposite (VAN) is one category of the nanocomposite materials, where nanocomposite is materials that contain multiphase building blocks with dimensions in nanometer range and exhibit improved physical properties. It has a wide range of applications in tuning electrical properties, [164], [195], [244], [245] magnetic properties,[195], [246] and optical properties[247] due to the unique coexisting in-plane and out-of-plane lattice matching. It is wise to introduce VAN to thin film electrodes due to the low conductivity from lack of conductive additives and film delamination at film-to-substrate interfaces causing by volume change.

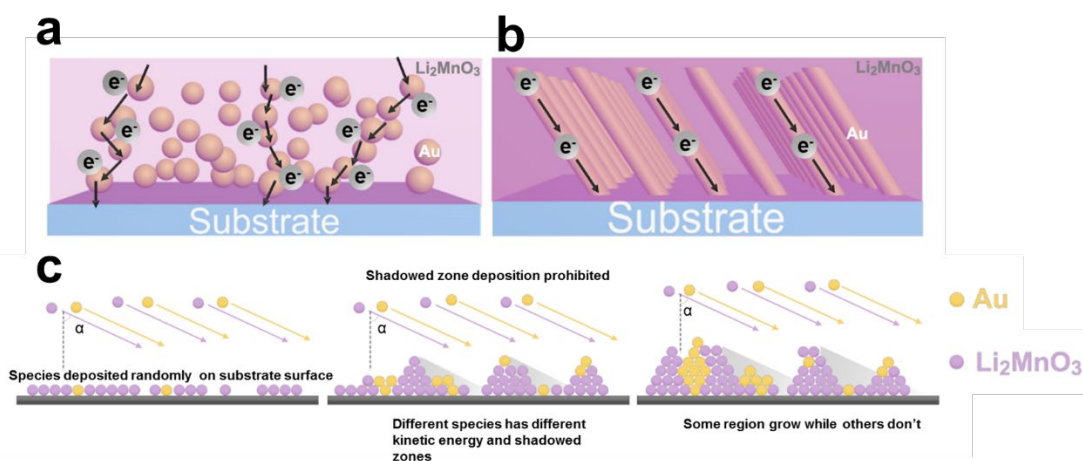


Figure 5.1 The schematic drawing of comparison between a) Li_2MnO_3 - Au particle and b) Li_2MnO_3 - Au pillar composite structures; and illustration of c) expected growth mechanism.

Here we propose, for the first time, a novel design of incorporating Au nanopillars into Li_2MnO_3 thin films through Oblique Angle Deposition (OAD) in pulsed laser deposition (PLD)

achieved by simply tilt the substrate. PLD offers extraordinary advantages in precise stoichiometry control of alloys or ceramics that obtain very sophisticated composition with minimal restrictions on the selection of target and substrate.[248] Besides, OAD is a technique where the incoming flux of target adatoms form certain angle with the substrate where the flux source introduces shadowing effect, and thus can achieve many novel porous structure designs.[222], [225], [249], [250] The schematic drawing of the design is shown in Figure 5.1(b). Different from the particle in matrix design we've explored in previous work (illustrated in Figure 5.1(a)), the Li_2MnO_3 -Au pillar configuration can provide a more effective, continuous pathway for electron, and the more effective solid-solid interfaces can possibly avoid the structure disruption.[164] Interestingly, there is no obvious columnar feature that was usually reported in OAPLD involved literatures, but the Au still exists as long, tilted pillars. This indicates a unique growth mechanism (Figure 5.1(c)), which is possibly due to the combined effect of mixed flux source (Au and Li_2MnO_3) and shadowing effect. More details will be discussed in later section. Despite the unexpected structural findings of the Li_2MnO_3 -Au nanocomposite thin films, the assembled coin cell exhibits excellent capacity retention even at 100th cycle. Optical measurement was also conducted, confirming the anisotropic optical response originated from Au pillars. The nanoindentation result suggests almost doubled hardness after the Au pillar incorporation compared to pure Li_2MnO_3 .

5.3 Experiments

Composite film growth. Li_2MnO_3 target was prepared by mixing commercial Li_2MnO_3 powder from Pfaltz & Bauer with 15% Li_2CO_3 (Alfa Aesar) due to the easy vaporization of Li during sintering. The Li_2MnO_3 target was sintered at 900 °C under oxygen flow for 24 hrs. The Li_2MnO_3 -Au composite target was prepared by attaching a piece of thin Au strip on central line

of the Li_2MnO_3 target and the target was concentrically rotating during the deposition. The composite Li_2MnO_3 -Au film were deposited on both Al_2O_3 single crystalline substrates for structural analysis and Au buffered stainless steel (Au-SS) substrates for electrochemical measurement. All depositions were conducted using pulsed laser deposition with KrF excimer laser source ($\lambda = 248$ nm, Lambda Physik Compex Pro 205) at laser frequency of 10Hz and energy of 2.5 J cm^{-2} . The target surface to substrate surface distance is kept at 5 cm. The temperature was set at $750 \text{ }^\circ\text{C}$ and oxygen partial pressure was maintained at 50 mTorr during deposition. Substrates were tilted at certain angle away from the substrate holder to achieve the oblique angle deposition configuration. The deposited film was cooled under 15 Torr O_2 at rate of $10 \text{ }^\circ\text{C}/\text{min}$.

Structural characterization. X-ray diffraction pattern (XRD) was measured using a $\text{Cu K}\alpha 1$ ($\lambda = 1.5406 \text{ \AA}$) source (PANalytical Empyrean Diffractometer) to characterize the out of plane crystalline characteristics of the samples. The measurement used 0.05° step size and 0.5 s step dwelling time with 2 theta angle range between 10° to 90° . Scanning electron microscopy (SEM, NovaNano SEM) was used to probe the surface morphology of composite film on Au-SS substrates. The acceleration voltage was set at 5 kV and spot size of 2.0 was used to be able to obtain high magnification images. Transmission electron microscopy (TEM), scanning transmission electron microscopy (STEM) (under high angle annular dark field, HAADF), and elemental distribution spectrum (EDS) were taken on sample deposited on Al_2O_3 using a FEI TALOS 200X system operated at 200kV.

Coin cell battery assembly and electrochemical characterization. CR2032 coin cell was assembled in a Ar filled glovebox (MBraun Labmaster, $\text{O}_2 < 0.1 \text{ ppm}$, $\text{H}_2\text{O} < 0.1 \text{ ppm}$) using Lithium metal anode (Alfa Aesar), Celgard 2400 PP separator (Celgard), and 1M LiPF_6 salt

dissolved in 1:1 volume ratio EC:DEC mixed organic electrolyte (Sigma Aldrich). The assembled coin cells were evaluated using a Arbin BTS2000 battery testing system. The cutoff voltage window was set between 2.0 V-4.8 V. Cycling performance was measured first at constant current density of $5 \mu\text{A}/\text{cm}^2$ and then kept under constant voltage until the current decreased below $1 \mu\text{A}$. The Cyclic Voltammetry (CV) at different cycles were measured at $20 \mu\text{V}/\text{s}$, and CV at different voltage sweep rate of $10 \mu\text{V}/\text{s}$, $20 \mu\text{V}/\text{s}$, $50 \mu\text{V}/\text{s}$, $75 \mu\text{V}/\text{s}$, $100 \mu\text{V}/\text{s}$ and $200 \mu\text{V}/\text{s}$ were also measured to evaluate the kinetics property of the battery. The rate performance measurement was conducted at current density respectively of $5 \mu\text{A}/\text{cm}^2$, $10 \mu\text{A}/\text{cm}^2$, $20 \mu\text{A}/\text{cm}^2$, and $80 \mu\text{A}/\text{cm}^2$, and the C-rate values of each current density were estimated using the actual discharge time. Electrochemical impedance spectrum was measured using Gamry Series G300 Potentiostat between $500 \mu\text{Hz}$ and 200000 Hz at 4V at 100^{th} cycle. The cell was aged at 4V constant voltage for 2 hrs to reach stable potential before the measurement started.

Optical characterization. The optical dielectric permittivity of all the films was evaluated using spectroscopic ellipsometry (JA Woollam RC2). The ellipsometer parameters ψ and Δ , related by the equation: $r_p/r_s = \tan(\psi)e^{i\Delta}$ (where r_p and r_s are the reflection coefficient for the p-polarization and s-polarization light, respectively) were fitted using the CompleteEASE software. The incident angle was varied from 50° to 70° with a step size of 10° . The ψ and Δ are measured at different angles to improve the accuracy of the fitted model. Li_2MnO_3 film was modeled using a Tauc-Lorentz oscillator and a Lorentz oscillator. Li_2MnO_3 -Au film was assumed to anisotropic since the Au pillar grows as a tilted pillar. Its in-plane permittivity was modeled using a Tauc-Lorentz oscillator and a Lorentz oscillator while the permittivity along the z direction was built

using a Tauc-Lorentz oscillator and a Drude-Lorentz model. The fitted models are shown in Figure 4.5(a)-(c).

Mechanical property measurement. Nanoindentation test was performed on a Hysitron TI 950 2000XYp with a Berkovich indenter. A loading-unloading function was applied to obtain force-displacement curves, based on which the film hardness at various depths was measured using instrumented nanoindentation method.[251]

5.4 Results and discussion

Study of morphology and microstructure

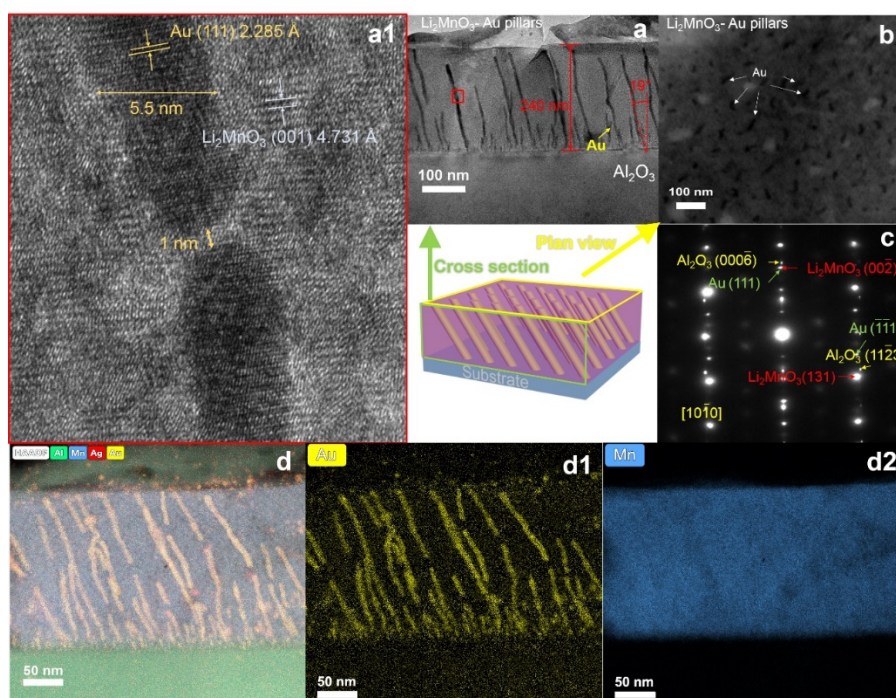


Figure 5.2 (a) Cross sectional TEM image of Li_2MnO_3 -Au composite on both Al_2O_3 substrate with (a1) HRTEM shows the d spacing of Au (111) and Li_2MnO_3 (001); (b) Plan-view TEM image indicates an aligned trend of the Au pillars inside Li_2MnO_3 ; (c) SAED pattern confirms the matching relationship Au and Li_2MnO_3 matrix from Al_2O_3 $[10\bar{1}0]$ zone axis; (d)(d1)(d2) EDX mapping confirming the elemental distribution in the film.

Structural characterization of the $\text{Li}_2\text{MnO}_3/\text{Au}$ composite thin film was achieved by X-ray diffraction (XRD), scanning electron microscopy (SEM), transmission electron microscopy (TEM), and high-angle annular dark-field scanning transmission electron microscopy (HAADF-STEM). Successful confirmation of the expected pillar structure in Figure 5.1 was performed through TEM/STEM technique on $\text{Li}_2\text{MnO}_3\text{-Au}$ on the Al_2O_3 sample. Figure 5.2(a) shows the low magnification TEM image of the sample. The Au particles exist as tilted pillars and they are roughly 50 nm separate from each other, and the average width of the pillars in Figure 5.3(a) is equal to 6 nm with aspect ratio varies from 40 – 4, measured from the figure. The pillars are all tilted toward one direction, forming an inclination angle of 19° with the substrate. Figure 5.2(b) shows the plan view image of the sample, which further demonstrates the uniform distribution of aligned Au pillars. High resolution TEM image is present in Figure 5.2(a1) to study the formation mechanism of such Au pillars. It can be observed that 1) there are some small Au particles distributing near the film-substrate interface region and 2) small gaps can be observed between pillars along longitudinal axes. The abovementioned mechanism can be explained using Figure 5.1(c). First, the small Au particles near interface are Au nucleates formed at the beginning stage of the growth but terminated to grow later due to shadowing effect.[252] Second, the gap in pillar along longitudinal axis is due to the adatom diffusion. In general, OAPLD would introduce pores due to the limited adatom diffusivity and shadowing effect, thus forming columnar-like growth feature.[253] Several main types of morphologies formed with mixed source are multilayered columns,[254] zigzag-shaped multilayer columns,[255] top/sides coated columns,[256]–[258]tilted columns with porosity,[259] and laterally assembled columns.[260] However, in this case the Au pillars in the Li_2MnO_3 matrix act as “adatoms diffusion bridge” so that the incoming flux arriving at two adjacent Li_2MnO_3 columns would

diffuse along the Au surface and hence connect the two columns that would otherwise leave a pore, in another word, the Au promoted the adatoms diffusion. The d -spacing of Li_2MnO_3 and along the out of plane direction is measured to be 4.731 Å and 2.285 Å, corresponding to $\text{Li}_2\text{MnO}_3(001)$ and $\text{Au}(111)$. Further, nano-sized domains can be observed in the HRTEM, which was reported to able to provide structure stability.[210] The epitaxial matching relationships of the Li_2MnO_3 -Au can be identified as $\text{Li}_2\text{MnO}_3(002)//\text{Au}(111)//\text{Al}_2\text{O}_3(0006)$ in the out of plane orientation and $\text{Li}_2\text{MnO}_3(131)//\text{Au}(\bar{1}\bar{1}\bar{1})//\text{Al}_2\text{O}_3(\mathbf{1}\mathbf{1}\bar{2}\mathbf{3})$ for the in-plane orientation based on corresponding selected area diffraction pattern (SAED) taken from $\text{Al}_2\text{O}_3[\mathbf{10}\bar{1}\mathbf{0}]$ zone axis shown in Figure 5.2(c). The film composition is confirmed by element distribution spectrum (EDS) in Figure 5.2(d). There are some small particles mostly on top of the film and these might be from the redeposition of metal ions during the TEM sample preparation. Interestingly, there are also Ag signal detected from the pillar, which could be from the Ag paste used to fix the substrate during the deposition.

The XRD pattern in Fig S1a indicates the highly textured growth of Li_2MnO_3 on both Al_2O_3 and Au-SS substrates. The XRD shows the composite $\text{Li}_2\text{MnO}_3/\text{Au}$ has $\text{Li}_2\text{MnO}_3(001)$ d -spacing of 4.728 Å on Al_2O_3 and 4.762 Å on Au-SS, which is equal to 0.14% compressive strain and 0.25% tensile strain in c -axis direction compared to reported bulk value.[261] The different strain state could be from different substrate. The Au peak is indistinguishable in the XRD pattern for both substrates. Unlike the peak broadening with particle morphology,[164] this indicates better lattice match between Au and Li_2MnO_3 . Besides, the Li_2MnO_3 peaks have overall lower intensity on Au-SS than that on Al_2O_3 , which also matches our previous results.[164]

Cycling performance of $\text{Li}_2\text{MnO}_3\text{-Au}$

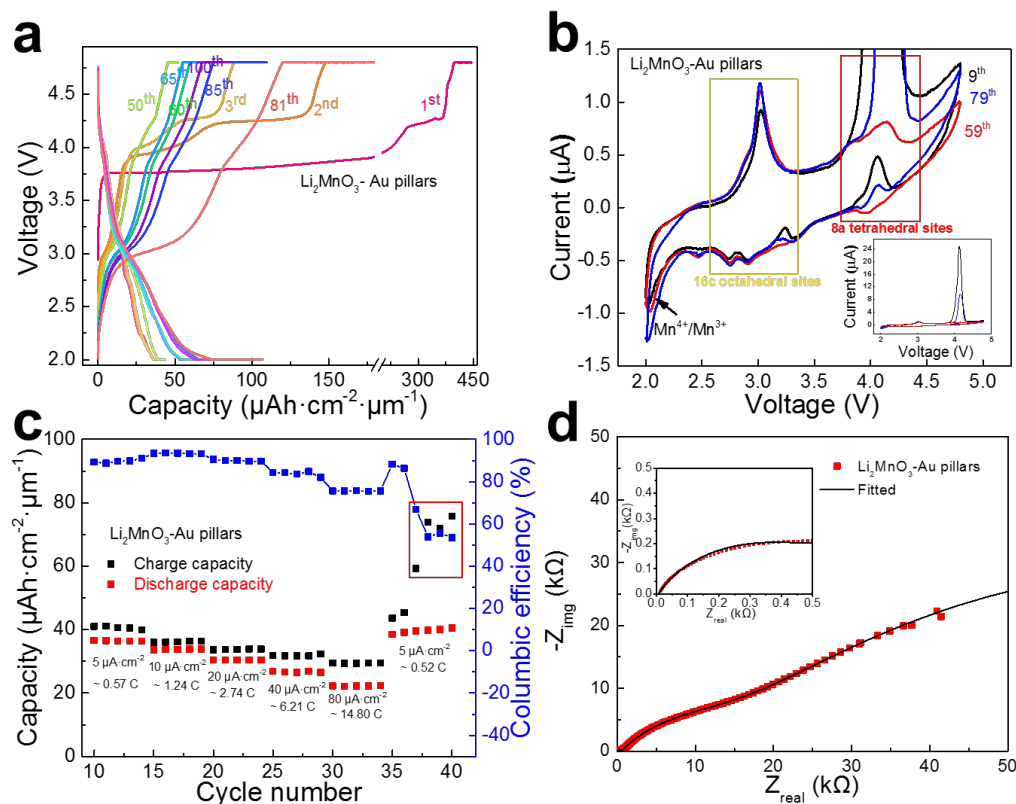


Figure 5.3 (a) Cycling performance of $\text{Li}_2\text{MnO}_3\text{-Au}$ after 100 cycles; (b) Cyclic voltammograms of $\text{Li}_2\text{MnO}_3\text{-Au}$ with potential $20 \mu\text{V/s}$ sweep rate at 9th, 59th, and 79th cycles; (c) C-rate performance test at current density of $5 \mu\text{A/cm}^2$, $10 \mu\text{A/cm}^2$, $20 \mu\text{A/cm}^2$, $40 \mu\text{A/cm}^2$, $80 \mu\text{A/cm}^2$ respectively with calculated columbic efficiency, and the corresponding estimated C-rate values are also labeled; (d) EIS measurement of the cell after cycling.

The electrochemical performance of the $\text{Li}_2\text{MnO}_3\text{-Au}$ on Au-SS substrate has been evaluated in 2032R coin cell. Figure 5.3(a) shows the cycling performance of the thin film battery, and it shows a $35.78 \mu\text{Ah}\cdot\text{cm}^{-2}\cdot\mu\text{m}^{-1}$ first cycle discharge capacity from constant current discharging step and total discharge capacity of $41.2 \mu\text{Ah}\cdot\text{cm}^{-2}\cdot\mu\text{m}^{-1}$. It is worth noting that the cell exhibits $62.32 \mu\text{Ah}\cdot\text{cm}^{-2}\cdot\mu\text{m}^{-1}$ constant current discharge capacity and $71.64 \mu\text{Ah}\cdot\text{cm}^{-2}\cdot\mu\text{m}^{-1}$ total capacity at 100th cycle, which is roughly a 74% increase compared to the first cycle. This phenomenon was reported in literature as gradual phase transformation upon cycling.[78]

However, the first cycle shows an unexpectedly large total charge capacity of $445.27 \mu\text{Ah}\cdot\text{cm}^{-2}\cdot\mu\text{m}^{-1}$, which can be translated to $1196.96 \text{mAh}\cdot\text{g}^{-1}$ and it exceeds the theoretical capacity $459 \text{mAh}\cdot\text{g}^{-1}$ for Li_2MnO_3 . Similar phenomenon was observed in pure Li_2MnO_3 as reported previously.[76] However, this phenomenon is much more significant in pure Li_2MnO_3 and the cell failed at 10th cycle. This can be the proof of increased film conductivity as the first overlarge charge capacity were also reported in other thin film work and were mainly attributed to electrolyte decomposition.[210], [228]

Two plateaus can be observed in the 1st cycle charge curve but not in the 100th cycle charge curve. The plateau that appears around 3.75 V might be attributed to the diffusion limit of the lithium ions, representing the step which lithium ions overcome the energy barrier and be extracted from the cathode. It shows the slow activation nature for thin film batteries and only appears in the first charge cycle. Another plateau around 4.2 V can be from the electrolyte decomposition and the SEI formation because it gradually fades upon cycling. Besides, it is observed the capacity increase starts from the 60th cycle. The cycle was performed after a cyclic voltammetry measurement at 59th cycle with sweep rate of $10 \mu\text{V/s}$ as shown in Figure 5.3(b). This might be due to the deep reaction from the very slow scan rate, which can be converted to a very slow C-rate of 0.01 C compared to the 0.5 C of regular cycles. This can explain why the capacity starts fading after the 60th cycle but increased again at 80th cycle and continues to fade until the 100th cycle. As the deep cycle increased the depth of reaction and thus the amount of material that undergoes phase transformation. In addition, the extra capacity can be ascribed from the extended plateau around 3V, which is the lithium intercalation at 16c octahedral sites of the spinel phase, again, proves the abovementioned statement. This behavior should be attributed

to the long Au tilted pillars that works as efficient current collectors after full activation, which was not observed in case of pure Li_2MnO_3 .

Reaction chemistry study by cyclic voltammetry measurement

Cyclic voltammetry measurement was conducted to study the redox reaction in the thin film electrode. Figure 5.3(b) demonstrates the CV results at the 9th, 59th, and 79th cycle. The CV shows typical redox reactions of spinel type structure, where the redox pair around 3V is the lithium insertion in empty 16c octahedral sites and the peaks around 4V is that in empty 8a tetrahedral sites. However, the unexpectedly large oxidation peak and the abnormal oxidation peak in the negative sweep direction also indicate the existence of electrolyte decomposition. Similar behavior has been observed in pure Li_2MnO_3 as reported before,[76] therefore the feature could be from the insulating nature of Li_2MnO_3 , especially in the dense thin film morphology. However, while the pure Li_2MnO_3 fails after the 9th cycle, the Li_2MnO_3 -Au composite can be cycled for at least 100 cycles and the electrochemical performance increase upon cycling. It indicates that the Au pillars increase the conductivity of the composite film and the cathode will need to be gradually activated by cycles. The CV measurement at different sweep rates of 10 $\mu\text{V/s}$, 20 $\mu\text{V/s}$, 50 $\mu\text{V/s}$, 75 $\mu\text{V/s}$, 100 $\mu\text{V/s}$, 200 $\mu\text{V/s}$ is shown in Figure 5.3(b). There are two sets of redox reaction pairs appearing in the curves. The redox couples at 4.04V/3.95V and 3.04V/2.88V are the Li intercalation at 8a tetrahedral and 16c octahedral interstitial sites, respectively, and there are also some shoulder peaks next to the two main redox couples, which is typical in spinel type Mn-based materials.[229] Further, the oxidation peaks at 4.2 V that are irrelevant to the sweep rates. These are the sign of electrolyte decomposition due to slow kinetics abovementioned, and the higher peak intensity at slower sweep rate suggests the slow reaction

constant. However, the reaction is suppressed compared to pure Li_2MnO_3 , indicating the kinetics improvement from Au pillars.

Rate performance and impedance study

The rate performance at current density $5 \mu\text{A cm}^{-2}$ to $80 \mu\text{A cm}^{-2}$ is shown in Figure 5.3(c), and the C-rate value are estimated and labeled at each corresponding current density. The Li_2MnO_3 -Au possesses excellent rate performance with 61% capacity retention at $80 \mu\text{A cm}^{-2}$ compared to $5 \mu\text{A cm}^{-2}$. The discharge capacity at 0.57 C is of $36.45 \mu\text{Ah cm}^{-2} \mu\text{m}^{-1}$ and the columbic efficiency is about 89.67 %. Besides, the columbic efficiency doesn't decrease until the current density is at $40 \mu\text{A cm}^{-2}$, where the discharge capacity retains ~73.15% of its value at 0.57 C. However, it is surprising four cycles at the end of stepwise rate performance measurements show unexpectedly large charge capacity. It can be observed that the voltage first decreases then recovers during the charge process, which is not the diffusion limitation as discussed for the 1st cycle but instead the presence of side reaction.[262] This can be the potential explanation that the electrolyte decomposition peak around 4.2V disappear at the 59th cycle but show up in the 79th cycle, presented in Figure 5.3(b), as well as the reason that the 81th cycle experiences much significant increase regarding only charge capacity. Electrochemical Impedance Spectroscopy measurements of the cell at 100th cycle is presented in Figure 5.3(d). The model used to fit the spectrum contains three R-C circuits that can be possibly ascribed to cathode electrolyte interphase, charge transfer process in the cell, and the inhomogeneous Au/ Li_2MnO_3 interfaces.[263][264]

Study of anisotropic optical properties

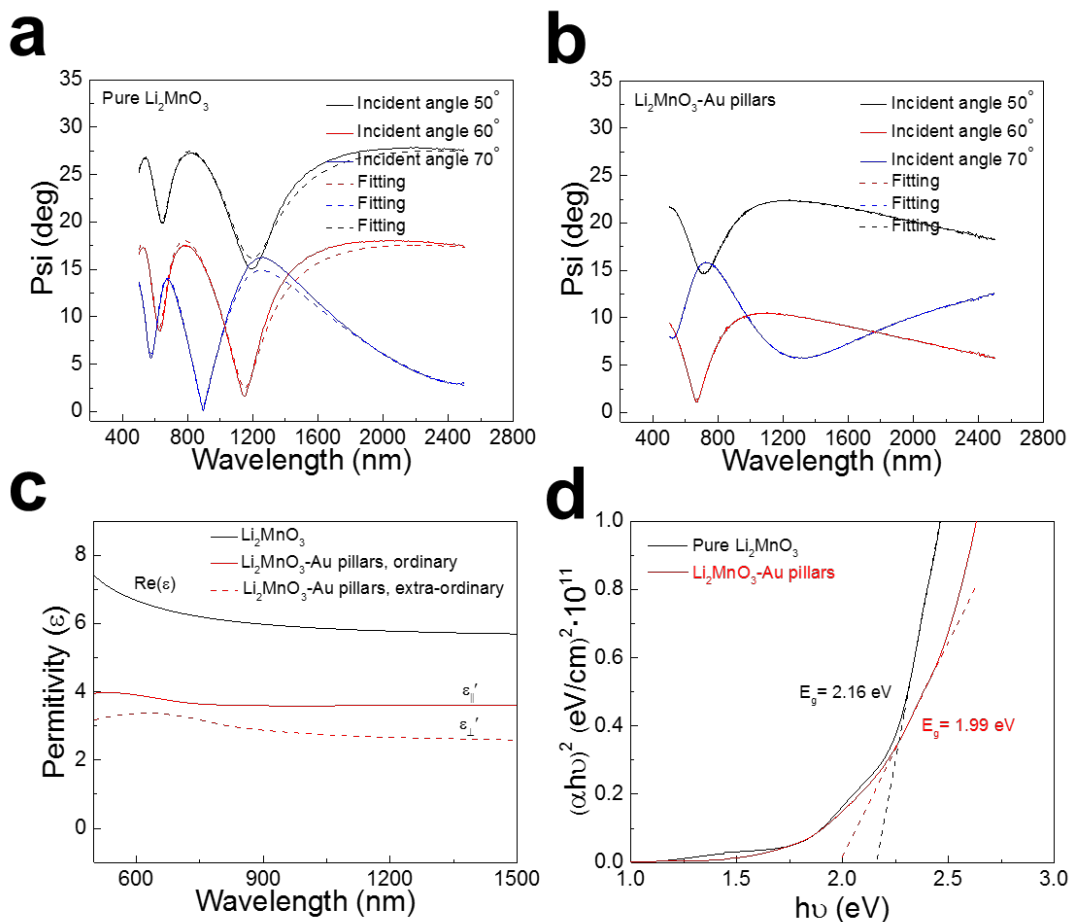


Figure 5.4 Psi obtained by ellipsometer at 50°, 60° and 70° with fitted data of (a) pure Li_2MnO_3 and (b) Li_2MnO_3 -Au pillars composite film; (c) Permittivity data measured through ellipsometer indicating the increased absorption of Li_2MnO_3 -Au and introduced anisotropy; (d) Tauc plot obtained through transmission measurement deciding the bandgap of Li_2MnO_3 and Li_2MnO_3 -Au pillar.

Apart from the traditional electrochemical performance, we are also interested in the optical properties due to the plasmonic Au. Anisotropic optical properties are evaluated to study the tunable optical permittivity due to the presence of tilted Au pillars in the film. Dielectric permittivity of the pure Li_2MnO_3 and Li_2MnO_3 -Au samples are calculated using angular dependent spectroscopic ellipsometry measurement and the results are presented in Figure

5.4(a)-(c). The ellipsometer parameter ψ and Δ was fitted with the use of general oscillator models to make it Kramers-Kronig consistent (see Methods section). The permittivity of Li_2MnO_3 (Figure 5.4(c)) shows a normal dispersion curve that is characteristic for dielectric materials. Interestingly, the Li_2MnO_3 -Au sample shows anisotropic permittivity in the in-plane and out-of-direction. The in-plane permittivity (ϵ'_{\parallel}) shows a typical dielectric behavior while the out-of-plane permittivity (ϵ'_{\perp}) shows the decrease in intensity indicating the existence of Au pillars in the z direction. The anisotropic behavior of Li_2MnO_3 -Au grants the potential of real-time online monitoring of battery charge-discharge behavior. The Au appears not just as pillars in the Li_2MnO_3 matrix but a certain degree of doping in the Li_2MnO_3 lattice as well as evidenced by the decrease of the bandgap for Li_2MnO_3 -Au composite from 2.15 eV to 1.95 eV calculated using the Tauc plot in Figure 5.4(d).

Tunability of physical properties by tilting angle

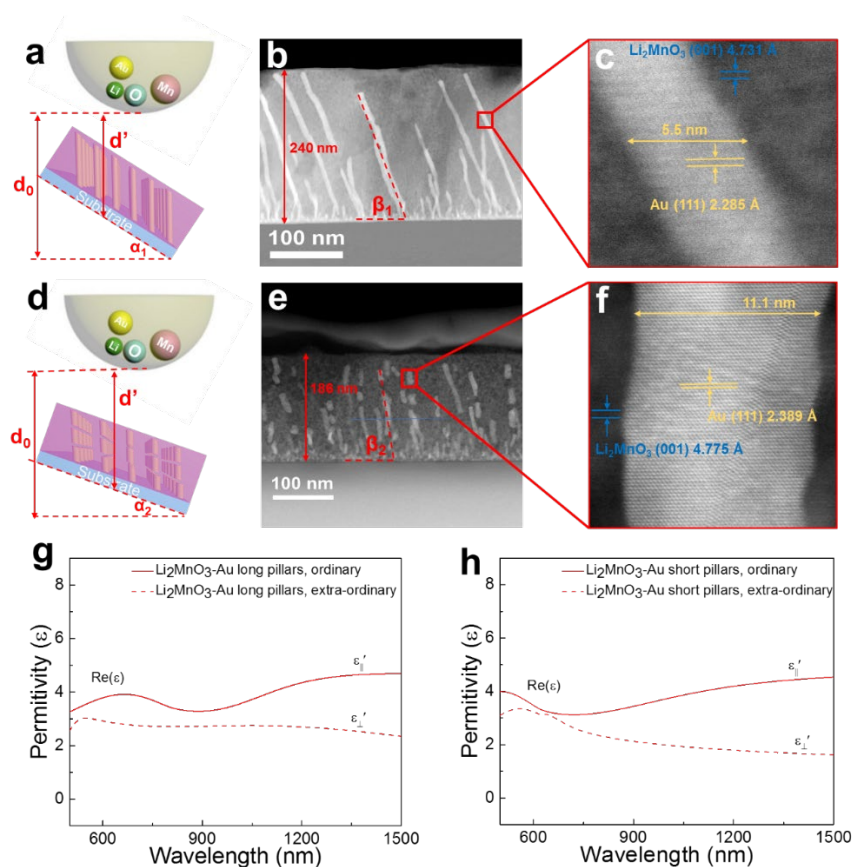


Figure 5.5 (a) Illustration of growth setup at higher tilt angle α_1 ; (b) thin film grown with thicker film and smaller tilt angle β_1 ; (c) HRSTEM showing Au pillar with small width; (d) illustration of growth setup at higher tilt angle α_2 ; (e) thin film grown with thinner film and larger tilt angle β_2 ; (f) HRSTEM showing Au pillar with increased width; (g) Permittivity curve of Li_2MnO_3 at higher tilt angle α_1 ; (h) permittivity curve of Li_2MnO_3 at a lower tilt angle α_2 .

Angular tunability on Li_2MnO_3 -Au pillar thin film morphology was also studied and the change of properties was characterized using optical measurement technique. TEM samples films grown at different tilt angle α were prepared, observed using HAADF technique and the result is shown in Figure 5.5. The setup shown in Figure 5.5(a) have target-to-substrate holder distance d_0 , actually target-to-substrate distance d' , and tilt angle α_1 . The composite film possesses thickness about 240 nm, long Au pillars with aspect ratio larger than 20, and pillar-substrate angle β_1 about 70° . On the other hand, the film exhibits thinner film (~ 180 nm) under

smaller tilt angle α_2 . Besides, the pillars are shorter yet wider (~ 11.1 nm) compared to configuration in Figure 5b, and the pillar-substrate angle β_2 is about 80° . What's more, the short pillars also hold different strain state compared to the long pillars. As it is mentioned, the long pillars experience a 0.14 % compressive strain in Li_2MnO_3 along [001] direction and 2.77 % compressive strain in Au along [111] direction, whereas the short pillars have 0.53 % tensile strain of Li_2MnO_3 (001) and 1.66 % tensile strain of Au (111). Reason smaller tilt angle renders this result can be explained by the growth rate controlled by the tilt angle. Smaller tilt angle indicates slower growth rate, further indicating increased stability of in-plane growth and suppression of out-of-plane growth.[265] This matches with the difference in thickness between the two configurations. It is known that smaller tilt angle α_2 result in less significant shadowing effect (more close to normal growth configuration), therefore the Li_2MnO_3 adatoms have higher chance to disrupt the continuous growth certain Au pillars, forming Au morphology that is more close to particle.[225][265] Furthermore, the Au pillars of these two films demonstrate distinct optical behavior as observed in Figure 5.5(g) and Figure 5.5(h). The permittivity (ϵ'_{\parallel}) along the in-plane direction presents a blue shift which might be due to the increased in-plane dimension of the Au pillars. Additionally, the out-of-plane permittivity (ϵ'_{\perp}) of shorter Au pillars decays faster than longer pillars due to its relatively higher volumetric percent.

5.5 Conclusion

The epitaxial Li_2MnO_3 -Au are obtained from oblique angle pulsed laser deposition and the tilted Au pillars can be obtained with different tilt angle, separation space, and length by altering the tilt angle and growth rate. The film was obtained in terms of Au pillars embedded in Li_2MnO_3 dense film rather than separated Li_2MnO_3 -Au composite columns, which is different from the typical result reported regarding other composite OAPLD systems.[252], [253], [266],

[267] This indicates the potential of creating even more complicated and novel structures by selecting the correct materials combination, where new applications can be explored. Besides, the successful demonstration angular tunability and correlation between thin film structure and optical properties suggesting such opto-electrochemical systems can be engineered to achieve real-time battery performance monitor and evaluation through optical approaches.

6. $\text{LiMn}_{0.5}\text{Ni}_{0.3}\text{Co}_{0.2}\text{O}_2$ THIN FILM CATHODE INTEGRATION ON NORMAL GLASS SLIDES BY PULSED LASER DEPOSITION

6.1 Overview

Simply one-step synthesis of $\text{LiMn}_{0.5}\text{Ni}_{0.3}\text{Co}_{0.2}\text{O}_2$ thin film on Al-doped ZnO transparent current collector is achieved on regular glass substrates using pulsed laser deposition (PLD) technique. The crystal structure, texture properties, film morphology and electrochemical properties are compared before and after galvanostatic cycling process. The AZO current collector shows excellent stability after the cycling. The successful integration of cathode on glass substrates provide successful first step integration of all-solid-state battery on glass substrates.

6.2 Introduction

Thin film lithium ion batteries have been extensively explored due to their advantages in applications such as portable electronics and microelectronics, because they exclude inactive additives such as binder and are superior in full-cell integration with designable structures and configurations. Most of the substrates for thin film lithium ion batteries are opaque conductive substrates such as Al, Cu, Ti, Carbon based substrates, but not much efforts are devoted on other substrates such as glass.

Glass is very widely applied in many fields and can be associated with battery for advanced applications such as google glass. It is much cheaper and readily available compared to other conductive substrates mentioned above. Besides, it is also explored as a useful substrate for different applications.[268], [269] However, glass is normally insulating and needed to be pretreated before it can be used for full-cell integration. ITO is a type of conductive glass that is

usually applied as current collectors on glass or other substrates. Hwang *et al.* deposited LiMn_2O_4 on ITO buffered Pt/Al substrates and discovered improved properties using RF magnetron sputtering,[270] Different synthesis techniques[271] and different cathode systems[272] were also explored. Different from ITO, Perkins *et al.* explored LiCoO_2 on SnO_2 buffered glass substrate and the film orientation and crystallinity is heavily dependent to it.[273]

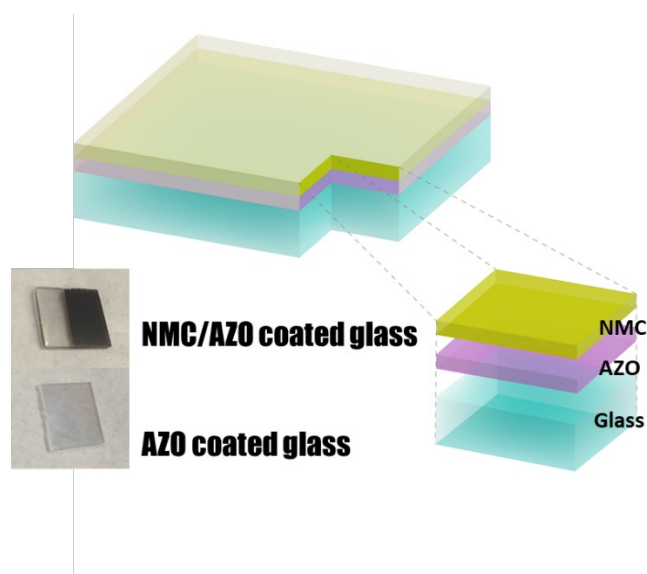


Figure 6.1 Schematic drawing of the stack of cathode and current collector on glass substrates.

In this work, we demonstrate the half-cell integration of transparent conductive Al-doped ZnO as current collector and NMC532 as cathode on glass substrates, which is illustrated in Figure 6.1. The thin film half-cell has been tested with electrochemical measurements including cyclic voltammetry and cycling performance, and the as-deposited thin film is compared with the electrochemically cycled thin film on crystallinity, texture, and surface morphologies.

6.3 Experimental



Figure 6.2 Scheme and photo for the two-electrode setup for electrochemical measurements.

NMC532 (MTI) powder was mixed with 15% Li_2CO_3 (Alfa Aesar), cold-pressed into a pellet, and sintered at $900\text{ }^\circ\text{C}$ under O_2 atmosphere for 24hrs. More details can be found in previous reports.[77],[155] Pulsed laser deposition system (Lambda Physik Compex Pro 205, 248 nm KrF) was applied for both NMC and AZO film growth. The glass substrates are glass slides purchased from Fisher scientific. The target-to-substrate distance was set to 5 cm. For NMC, the growth parameters are: laser frequency 5 Hz for 33 mins, energy density 1.9 J cm^{-2} , O_2 atmosphere pressure 10 mTorr, deposition temperature $550\text{ }^\circ\text{C}$, annealing 1 h at $550\text{ }^\circ\text{C}$ for 1 h then cooled at $10\text{ }^\circ\text{C/min}$ under 15 Torr O_2 . For AZO, the growth parameters are: laser frequency 10 Hz for 7 mins, energy density 3.3 J cm^{-2} , O_2 atmosphere pressure 7 mTorr, deposition temperature $420\text{ }^\circ\text{C}$, cooled at $10\text{ }^\circ\text{C/min}$ under 7 mTorr O_2 . X-ray diffraction (XRD) was performed using PANalytical Empyrean Diffractometer system with a $\text{Cu K}\alpha 1$ ($\lambda = 1.5406\text{ \AA}$) source. FEI NOVA nanoSEM Field Emission was used for micrograph probe at 10 kV. SEM FEI TALOS 200X system was used to take Transmission electron microscopy (TEM) and scanning transmission electron microscopy (STEM) (under high angle annular dark field, HAADF) images. Ar filled glovebox (MBraun, $\text{O}_2 < 0.1\text{ ppm}$, $\text{H}_2\text{O} < 0.1\text{ ppm}$) was used to perform two-

electrode measurements with Li metal anode (Sigma Aldrich) and 1M LiPF₆ in EC:DMC organic electrolyte. The set-up can be found in Figure 6.2. Arbin BTS2000 testing system was used for all the electrochemical tests. The voltage window for all the measurements is between 2.0V-4.2V and current was kept constant at about 5 $\mu\text{A}/\text{cm}^2$. The C-rate is estimated based on the actual measurement time for each cycle. The Cyclic Voltammetry (CV) was measured at potential ramp rate from 20 $\mu\text{V}/\text{s}$ to 400 $\mu\text{V}/\text{s}$.

6.4 Results and discussion

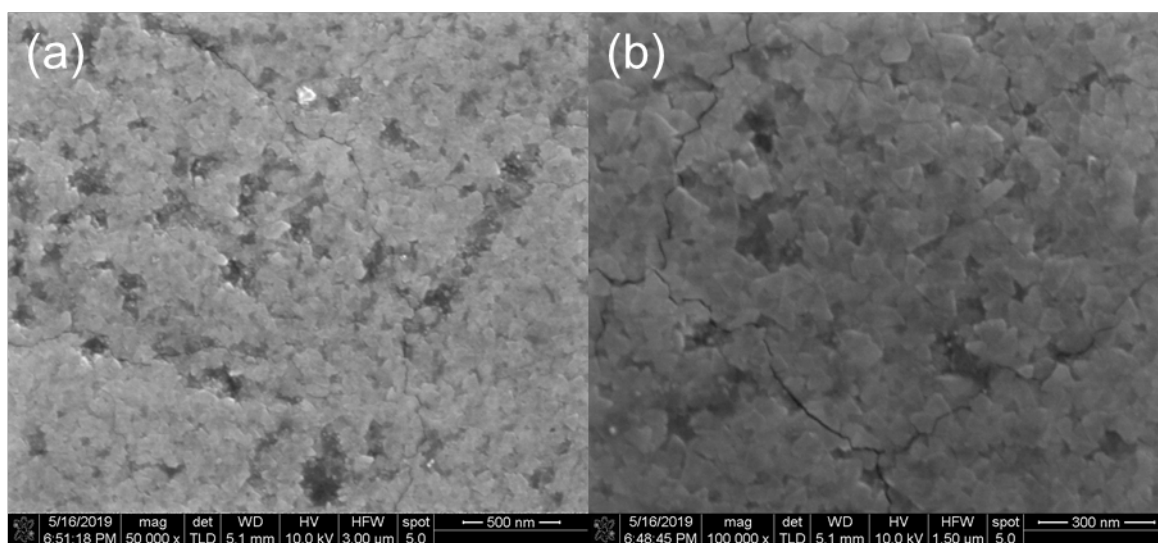


Figure 6.3 (a) Low-magnification SEM micrograph of as-deposited NMC/AZO/glass thin films; (b) high-magnification SEM micrograph of as-deposited NMC/AZO/glass thin films.

The as-deposit film was examined on its surface morphology using SEM, as shown in Figure 6.3, which exhibits a typical platelet grain morphology of layered oxides obtained by pulsed laser deposition.[198] Besides, some minor cracks can be observed along the grain boundaries. The possible reasons for this can be a result of strain relaxation from the large mismatch between the preferred orientation of AZO current collectors and NMC films.[235], [274], [275] This statement can be further confirmed by the out-of-plane XRD measurement results shown in

Figure 6.4(a). First, the XRD pattern shows both AZO buffer layer and NMC film have highly preferred growth orientation along the out-of-plane direction, and the lattice misfit between AZO(0002) ($d=1.36 \text{ \AA}$) and NMC(0006) ($d=1.25 \text{ \AA}$) can be calculated by the following equation:

$$\varepsilon_{\parallel} = \frac{|d_{NMC(0006)} - d_{AZO(0002)}|}{d_{NMC(0006)}}$$

which gives out misfit ε_{\parallel} around 8%. Additionally, the in-plane texture property was explored using pole figure measurement exhibit in Figure 6.4(b) -6.4(e). Different from the aforementioned out-of-plane XRD pattern, the in-plane pole figures for both AZO($10\bar{1}4$) and NMC($10\bar{1}4$) show a powder-like behavior, indicating a polycrystalline nature along the in-plane orientation.

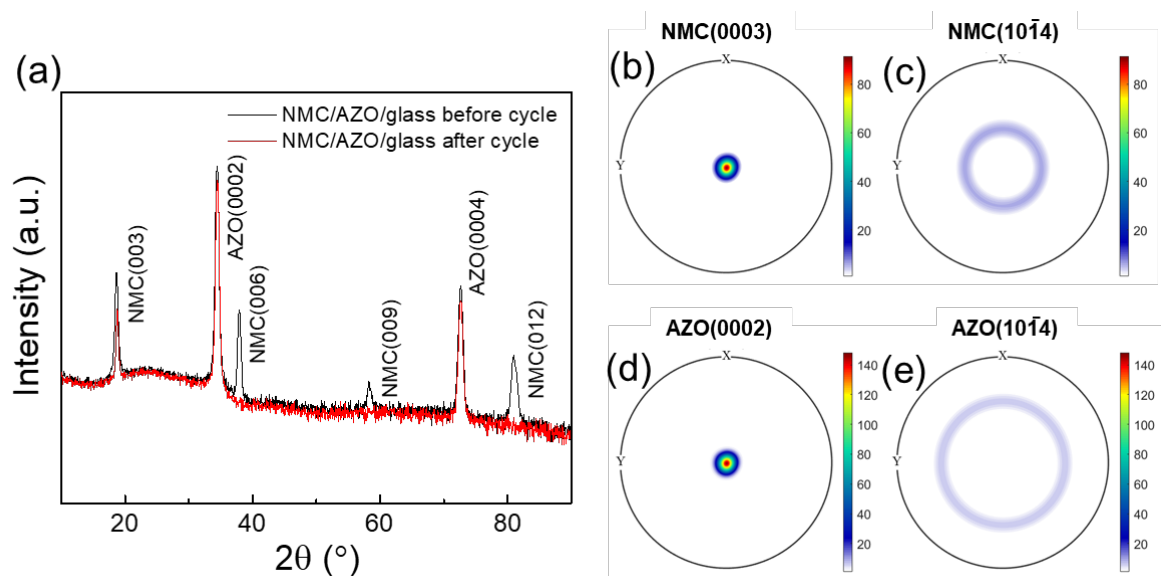


Figure 6.4 (a) Out-of-plane XRD pattern of as-deposited NMC/AZO/glass thin films and cycled NMC/AZO/glass thin films; (b) pole figure NMC(0003), (c) pole figure NMC($10\bar{1}4$), (d) pole figure AZO(0002), and (e) pole figure AZO($10\bar{1}4$) of as-deposited thin films.

The electrochemical measurements were conducted using a two-electrode set-up in the glovebox. The thin film cathode was cycled between 3.0V- 4.2V galvanostatically and the charge rate can be estimated to be around 0.02C while the discharge rate is roughly 0.05C for the first

cycle in Figure 6.5(a). The discharge capacity is about $800 \mu\text{Ah cm}^{-2} \mu\text{m}^{-1}$, which exceeds the theoretical volumetric capacity of $574.08 \mu\text{Ah cm}^{-2} \mu\text{m}^{-1}$ and this suggests heavy pseudocapacitive contribution from the thin film nature.[276] The possible electrolyte decomposition can be excluded as the dQ/dV plot shown in the inset only shows the typical anodic and cathodic peaks of $\text{Ni}^{2+}/\text{Ni}^{4+}$ pairs.[55] 5 consecutive cycles of CV measurements were performed at ramp rate of $50 \mu\text{V/s}$ in Figure 6.5(b). The average potential of cathodic peaks is around 3.5V and that of anodic peaks is 3.95V , representing $\text{Ni}^{4+} \rightarrow \text{Ni}^{2+}$ reduction reactions and $\text{Ni}^{2+} \rightarrow \text{Ni}^{4+}$ oxidation reactions, respectively. The relatively large potential difference between anodic and cathodic reactions suggests a significant polarization in the cathode, which is expected due to the thin film properties of the as-deposited NMC. It is also noted the intensity ratio of cathodic peaks to anodic peaks largely increased after the first cycle, indicating the improved redox reaction reversibility after full activation and homogenization. The galvanostatic cycling test shows the capacity decays fast in 10 cycles, and the C-rate at the 10th cycle is about 2.6C where the 1st cycle has C-rate about 0.3C in Figure 6.5(c). The CV measurements were again applied on the cycled film, shown in Figure 6.5(d), and it shows pure pseudocapacitive behavior under different ramp rates.[277]

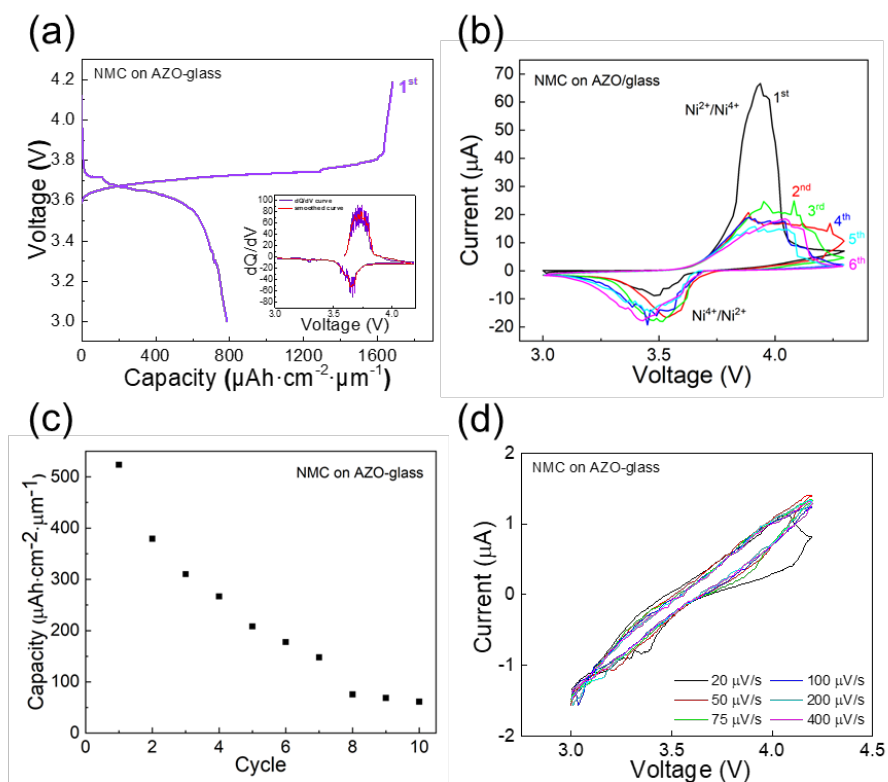


Figure 6.5 (a) Charge-discharge curve of the first cycle of NMC/AZO/glass with inset showing the dQ/dV plot of that; (b) five consecutive CV cycles of NMC/AZO/glass thin films at potential sweep rate of $50\ \mu\text{V/s}$; (c) cycling behavior of NMC/AZO/glass thin films for 10 cycles; (d) CV measurements of NMC/AZO/glass after cycles at different sweep rate of $20\ \mu\text{V/s}$, $50\ \mu\text{V/s}$, $75\ \mu\text{V/s}$, $100\ \mu\text{V/s}$, $200\ \mu\text{V/s}$, and $400\ \mu\text{V/s}$.

The cycled film was cleaned and the structure as well as surface morphology was remeasured using XRD and SEM. The out-of-plane XRD of the cycled film is shown in Figure 6.4(a), which is observed that the peak intensities of NMC are largely decreased while that of AZO almost stays the same. Similar results are shown in the pole figure measurements demonstrated in Figure 6.6(a)-6.6(d). The NMC(0003) pole figure has decreased out-of-plane intensity and shows more random distribution of orientations, suggesting possible fragmentation or mechanical failure of cycled film. However, the AZO pole figures almost have no difference compared to the as-deposited AZO pole figures. The SEM micrographs in Figure 6.6(e)-6.6(f) confirm the

mechanical failure, where the cracks along the grain boundaries has propagated significantly and some intragranular cracks can also be observed in the high-mag SEM micrograph. Nonetheless, no obvious film delamination is observed.

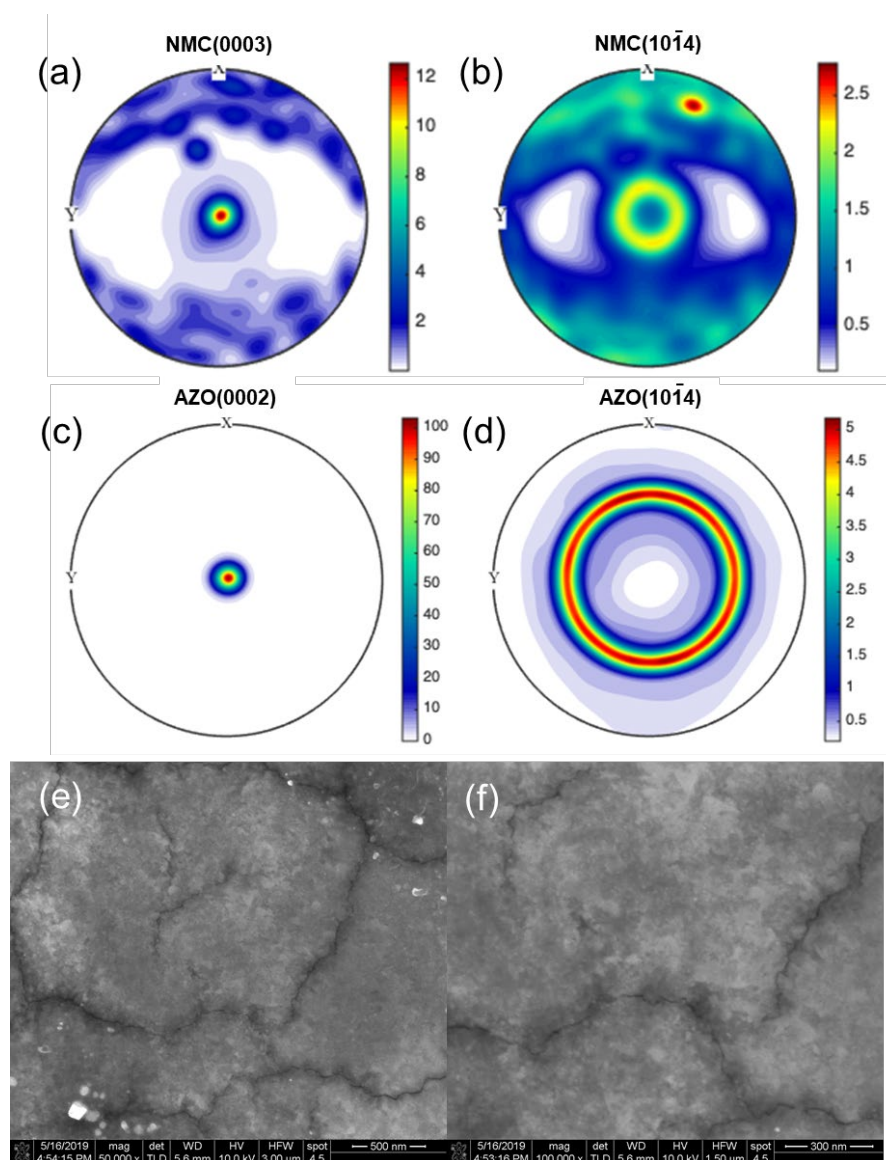


Figure 6.6 (a) pole figure NMC(0003), (b) pole figure NMC($10\bar{1}4$), (c) pole figure AZO(0002), and (d) pole figure AZO($10\bar{1}4$) of as-deposited thin films; (e) low-magnification SEM micrograph of cycled NMC/AZO/glass thin films; (f) high-magnification SEM micrograph of cycled NMC/AZO/glass thin films.

6.5 Conclusion

In this work, we have demonstrated a very straightforward method to integrate thin film cathode on glass substrates. This method has great potential in designing all-solid-state batteries integrated on glass substrates due to the flexibility of PLD growth on different material systems. However, the film needs to be modified using either nanocomposite/nanostructured methodology to improve the actual film performance.

7. SUMMARY AND OUTLOOK

Thin film batteries are promising for high power lithium ion batteries as the reduced thickness allows faster lithium diffusion in the electrodes. However conventional 2D planar film geometries could have limited energy loading due to the constraint footprint. Therefore, modification on thin film electrodes is necessary to meet industrial standard. In this review, we have reviewed representative advancements of thin film cathode electrodes using nanostructure and nanocomposite concepts for advanced lithium ion battery applications. It can be summarized that:

- 1) Interconnected nanostructures have better cycling stability due to the robust building blocks;
- 2) Synthesis techniques involve fine atomic level reaction gives out thin films with better performance;
- 3) Most thin film cathodes require high temperature treatments in order to obtain proper crystallinity, crystallographic phase or mechanical robustness;
- 4) Higher surface area can increase the active material loading and electrochemical performance, but also promote more side reactions, which generally require application of surface coatings;

However, several challenges remain in this field.

- 1) Thick film slurry electrodes are far well studied than thin film electrodes. It is important to focus more on binder-free thin film electrodes as it can help reduce the inactive mass in the electrodes to improve energy density, and high-performance thin film electrodes are necessary for safer all-solid-state batteries.

- 2) A large portion of studies has been conducted on anode materials or the relatively simple cathode model systems (LiFePO_4 , LiCoO_2 , LiMn_2O_4 , V_2O_5) due to the difficulties in synthesizing complicated cathode materials by using current established thin film techniques. Therefore, it is important to develop simple, cost-effective and scalable techniques for advanced thin film cathode modifications.
- 3) Microstructure study of nanocomposite thin film cathodes are lacking. This is however especially important in order to achieve correct conclusion of enhancement mechanisms and to design better structures.
- 4) A standardized data format was missing from many literatures studying thin film electrodes and thus is very much needed. It seems rather random that whether the value of gravimetric capacity, volumetric capacity, or areal capacity were chosen to be published in these literatures, which adds significant difficulties to compare the performance of different studies.

We selected the reported data of several representative modified thin film cathode materials modified by the different modification approaches and summarizes in Peukert plot shown in Figure 7.1, which can provide basic guidance for future research to design advanced thin film

cathode electrodes.

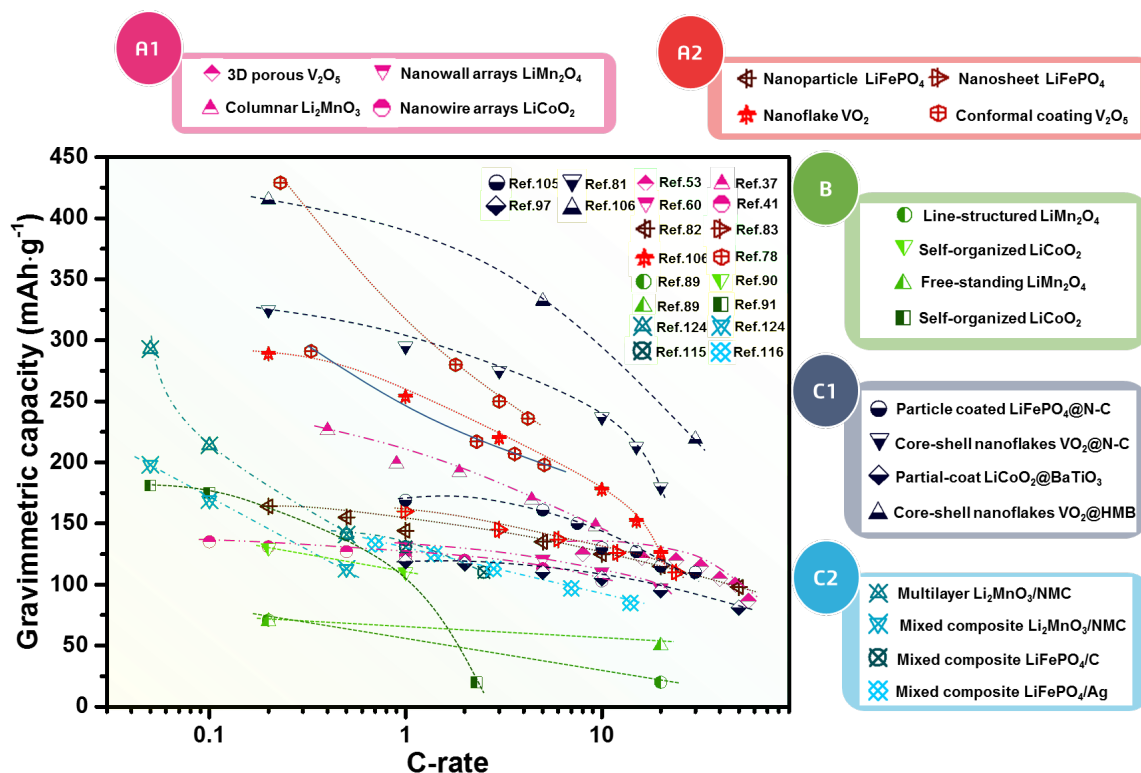


Figure 7.1 Peukert plot of representative thin film cathode electrodes modified with approach A1,A2,B,C1, and C2.

Apart from the current effort that has been put into the thin film cathode modification work by us, there are several things worth attention and continuous study in the future:

- 1) Despite the advantages of synthesizing thin film cathodes with complex compositions, it is still relatively difficult to synthesize lithiated cathode materials. Another type of layered oxide, VO_x , which is usually synthesized as nonlithiated state, worths more attention;
- 2) More integration work on substrates like MICA, glass should be explored and our previous results of Au incorporation or morphology change should be applied into the integration work;

- 3) Similar modification technique should be applied to solid state electrolyte to aiming to improve the electrochemical performance and solving instable electrolyte-electrode interfacial issue;
- 4) All-solid-state lithium ion batteries on substrates like glass or MICA needs to be finally integrated using comprehensive modification techniques, which is potentially applicable for transparent batteries or flexible batteries.

REFERENCES

- [1] M. Winter and R. J. Brodd, "What Are Batteries , Fuel Cells , and Supercapacitors ? What Are Batteries , Fuel Cells , and Supercapacitors ?," vol. 104, no. September, pp. 4245–4270, 2004.
- [2] X. Lu, M. Yu, G. Wang, Y. Tong, and Y. Li, "Flexible solid-state supercapacitors: design, fabrication and applications," *Energy Environ. Sci.*, vol. 7, no. 7, pp. 2160–2181, 2014.
- [3] Y. Liu, H. Pan, M. Gao, and Q. Wang, "Advanced hydrogen storage alloys for Ni/MH rechargeable batteries," *J. Mater. Chem.*, vol. 21, no. 13, pp. 4743–4755, 2011.
- [4] R. Alcántara, P. Lavela, J. L. Tirado, E. Zhecheva, and R. Stoyanova, "Recent advances in the study of layered lithium transition metal oxides and their application as intercalation electrodes," *J. Solid State Electrochem.*, vol. 3, no. 3, pp. 121–134, 1999.
- [5] J. M. Tarascon and M. Armand, "Issues and challenges facing rechargeable lithium batteries.," *Nature*, vol. 414, no. 6861, pp. 359–67, 2001.
- [6] K. Xu, "Nonaqueous liquid electrolytes for lithium-based rechargeable batteries," *Chem. Rev.*, vol. 104, no. 10, pp. 4303–4417, 2004.
- [7] R. Selim and P. Bro, "Some Observations on Rechargeable Lithium Electrodes in a Propylene Carbonate Electrolyte," *J. Electrochem. Soc.*, vol. 121, no. 11, p. 1457, 1974.
- [8] V. R. Koch and J. H. Young, "The Stability of the Secondary Lithium Electrode in Tetrahydrofuran-Based Electrolytes," *J. Electrochem. Soc.*, vol. 125, no. 9, p. 1371, 1978.
- [9] I. Yoshimatsu, "Lithium Electrode Morphology during Cycling in Lithium Cells," *J. Electrochem. Soc.*, vol. 135, no. 10, p. 2422, 1988.
- [10] M. S. Whittingham, "Elecgtrical Energy Storage and Intercalacgtn Chemistry," *Science (80-)*, vol. 192, no. 4244, pp. 1126–1127, 1976.
- [11] M. S. Whittingham, "Chemistry of intercalation compounds: Metal guests in chalcogenide hosts," *Prog. Solid State Chem.*, vol. 12, no. 1, pp. 41–99, 1978.
- [12] M. BRAIN, "How Lithium-ion Batteries Work," 2006. [Online]. Available: <http://electronics.howstuffworks.com/everyday-tech/lithium-ion-battery1.htm>.
- [13] J. B. Goodenough and Y. Kim, "Challenges for rechargeable Li batteries," *Chem. Mater.*, vol. 22, no. 3, pp. 587–603, 2010.

- [14] J. R. D. Rosamaría Fong, Ulrich von Sacken, "Studies of Lithium Intercalation into Carbons Using Nonaqueous Electrochemical Cells," *J. Electrochem. Soc.*, vol. 137, no. 7, pp. 2009–2013, 1990.
- [15] A. Blyr, C. Sigala, G. Amatucci, D. Guyomard, Y. Chabre, and J. M. Tarascon, "Self-Discharge of LiMn₂O₄/C Li-ion Cells in Their Discharge State," vol. 145, no. 1, 1998.
- [16] D. W. Murphy, J. N. Carides, F. J. Di Salvo, C. Cros, and J. V. Waszczak, "Cathodes for nonaqueous lithium batteries based on VS₂," *Mater. Res. Bull.*, vol. 12, no. 8, pp. 825–830, 1977.
- [17] X. Zhang, R. Kostecki, T. J. Richardson, J. K. Pugh, and P. N. Ross, "Electrochemical and Infrared Studies of the Reduction of Organic Carbonates," *J. Electrochem. Soc.*, vol. 148, no. 12, p. A1341, 2001.
- [18] K. Hayashi, Y. Nemoto, S. Tobishima, and J. Yamaki, "Mixed solvent electrolyte for high voltage lithium metal secondary cells," *Electrochim. Acta*, vol. 44, pp. 2337–2344, 1999.
- [19] S. E. Sloop, J. K. Pugh, S. Wang, J. B. Kerr, and K. Kinoshita, "Chemical Reactivity of PF₅ and LiPF₆ in Ethylene Carbonate/Dimethyl Carbonate Solutions," *Electrochem. Solid-State Lett.*, vol. 4, no. 4, p. A42, 2001.
- [20] A. Eftekhari, Y. Liu, and P. Chen, "Different roles of ionic liquids in lithium batteries," *J. Power Sources*, vol. 334, no. December 2016, pp. 221–239, 2016.
- [21] H. Davy, "The Bakerian Lecture: On Some Chemical Agencies of Electricity," *Phil. Trans. Roy. Soc.*, vol. 97, no. 1807, pp. 1–56, 1807.
- [22] J.-W. Song, C. C. Nguyen, and S.-W. Song, "Stabilized cycling performance of silicon oxide anode in ionic liquid electrolyte for rechargeable lithium batteries," *RSC Adv.*, vol. 2, no. 5, p. 2003, 2012.
- [23] T. Sugimoto *et al.*, "Application of bis(fluorosulfonyl)imide-based ionic liquid electrolyte to silicon-nickel-carbon composite anode for lithium-ion batteries," *J. Power Sources*, vol. 195, no. 18, pp. 6153–6156, 2010.
- [24] B. G. Adachi, N. Imanaka, and H. Aono, "Fast Li @ Conducting Ceramic Electrolytes," *Ceram.*, pp. 127–135, 1996.
- [25] J. B. Bates, N. J. Dudney, B. Neudecker, A. Ueda, and C. D. Evans, "Thin-film lithium and lithium-ion batteries," *Solid State Ionics*, vol. 135, no. 1–4, pp. 33–45, 2000.

- [26] K. Nagata and T. Nanno, "All solid battery with phosphate compounds made through sintering process," *J. Power Sources*, vol. 174, no. 2, pp. 832–837, 2007.
- [27] D. Aurbach, M. Koltypin, and H. Teller, "In situ AFM imaging of surface phenomena on composite graphite electrodes during lithium insertion," *Langmuir*, vol. 18, no. 23, pp. 9000–9009, 2002.
- [28] M. Yoshio, H. Wang, and K. Fukuda, "Spherical carbon-coated natural graphite as a lithium-ion battery-anode material," *Angew. Chemie - Int. Ed.*, vol. 42, no. 35, pp. 4203–4206, 2003.
- [29] M. Winter, J. O. Besenhard, M. E. Spahr, and P. Novák, "Insertion Electrode Materials for Rechargeable Lithium Batteries," *Adv. Mater.*, vol. 10, no. 10, pp. 725–763, 1998.
- [30] Z. Chen, Y. Cao, J. Qian, X. Ai, and H. Yang, "Facile synthesis and stable lithium storage performances of Sn- sandwiched nanoparticles as a high capacity anode material for rechargeable Li batteries," *J. Mater. Chem.*, vol. 20, no. 34, p. 7266, 2010.
- [31] P. Poizot, S. Laruelle, S. Grugeon, L. Dupont, and J. Tarascon, "Nano-sized transition-metaloxides as negative-electrode materials for lithium-ion batteries," *Nature*, vol. 407, no. September, pp. 496–499, 2000.
- [32] Y. Kwon and J. Cho, "High capacity carbon-coated Si₇₀Sn₃₀ nanoalloys for lithium battery anode material," *Chem. Commun. (Camb)*, no. 9, pp. 1109–1111, 2008.
- [33] J. Cabana, L. Monconduit, D. Larcher, and M. R. Palacín, "Beyond intercalation-based Li-ion batteries: The state of the art and challenges of electrode materials reacting through conversion reactions," *Adv. Mater.*, vol. 22, no. 35, pp. 170–192, 2010.
- [34] J. Yan, X. Liu, and B. Li, "Recent progress in Li-rich layered oxides as cathode materials for Li-ion batteries," *RSC Adv.*, vol. 4, no. 108, pp. 63268–63284, 2014.
- [35] A. k. Padhi, K. S. Nanjundaswamy, and J. B. Goodenough, "Phospho-olivines as Positive-Electrode Materials for Rechargeable Lithium Batteries," *J. Electrochem. Soc.*, vol. 144, no. 4, pp. 1188–1194, 1997.
- [36] M. S. Whittingham, "Lithium Batteries and Cathode Materials," *Chem. Rev.*, vol. 104, no. 10, pp. 4271–4302, 2004.
- [37] C. M. Julien, A. Mauger, K. Zaghib, and H. Groult, "Comparative Issues of Cathode Materials for Li-Ion Batteries," *Inorganics*, vol. 2, pp. 132–154, 2014.

- [38] J. Chen, C. Hsu, Y. Lin, M. Hsiao, and G. T. Fey, "High-power LiFePO₄ cathode materials with a continuous nano carbon network for lithium-ion batteries," *J. Power Sources*, vol. 184, pp. 498–502, 2008.
- [39] Y. Wang, Y. Wang, E. Hosono, K. Wang, and H. Zhou, "The Design of a LiFePO₄ / Carbon Nanocomposite With a Core – Shell Structure and Its Synthesis by an In Situ Polymerization Restriction Method **," *Angew. Chem. Int. Ed.*, no. 47, pp. 7461–7465, 2008.
- [40] A. S. Aricò *et al.*, "Nanostructured materials for advanced energy conversion and storage devices," *Nat. Mater.*, vol. 4, no. May, pp. 366–377, 2005.
- [41] G. T. Fey, H. Tu, K. Huang, Y. Lin, H. Kao, and S. Chan, "Particle size effects of carbon sources on electrochemical properties of LiFePO₄/C composites," *J. Solid State Electrochem.*, vol. 16, pp. 1857–1862, 2012.
- [42] J. Wang and X. Sun, "Understanding and recent development of carbon coating on LiFePO₄ cathode materials for lithium-ion batteries," *Energy Environ. Sci.*, no. 5, pp. 5163–5185, 2012.
- [43] M. M. Thackeray, P. G. Bruce, J. B. Goodenough, and S. P. Road, "LITHIUM INSERTION INTO MANGANESE SPINELS," *Mater. Res. Bull.*, vol. 18, pp. 461–472, 1983.
- [44] A. M. Kannan and A. Manthiram, "Surface/Chemically Modified LiMn₂O₄ Cathodes for Lithium-Ion Batteries," *Electrochem. Solid-State Lett.*, vol. 5, no. 7, pp. 167–169, 2002.
- [45] J. S. Gnanaraj, V. G. Pol, A. Gedanken, and D. Aurbach, "Improving the high-temperature performance of LiMn₂O₄ spinel electrodes by coating the active mass with MgO via a sonochemical method," *Electrochem. commun.*, vol. 5, pp. 940–945, 2003.
- [46] D. Lee, K. Lee, S. Myung, H. Yashiro, and Y. Sun, "Improvement of electrochemical properties of Li_{1.1}Al_{0.05}Mn_{1.85}O₄ achieved by an AlF₃ coating," *J. Power Sources*, vol. 196, no. 3, pp. 1353–1357, 2011.
- [47] D. H. Jang, Y. J. Shin, and S. M. Oh, "Dissolution of Spinel Oxides and Capacity Losses in 4 V Li/Li_xMn₂O₄ Cells," *J. Electrochem. Soc.*, vol. 143, no. 7, pp. 2204–2211, 1996.
- [48] Y. Xia and M. Yoshio, "Studies on Li-Mn-O spinel system (obtained from melt-impregnation method) as a cathode for 4 V lithium batteries Part IV . High and low temperature performance of LiMn₂O₄," *J. Power Sources*, vol. 66, pp. 129–133, 1997.

- [49] M. M. Thackeray *et al.*, “Stabilization of insertion electrodes for lithium batteries,” *J. Power Sources*, vol. 81–82, pp. 60–66, 1999.
- [50] K. Yoon and K. Kim, “Investigations into capacity fading as a result of a Jahn – Teller distortion in 4 V LiMn₂O₄ thin film electrodes,” *Electrochim. Acta*, vol. 49, pp. 3327–3337, 2004.
- [51] K. Y. Chung, C. Ryu, and K. Kim, “Onset Mechanism of Jahn-Teller Distortion in 4 V LiMn₂O₄ and Its Suppression by LiM_{0.05}Mn_{1.95}O₄ (M = Co, Ni) Coating,” *J. Electrochem. Soc.*, vol. 4, pp. 791–795, 2005.
- [52] C. Shen, R. Gundakaram, R. Liu, and H. Sheu, “Absence of phase transformation at low temperature in Co-doped LiMn₂O₄ samples,” *J. Chem. Soc. Dalt. Trans.*, pp. 37–40, 2001.
- [53] X. Li, Y. Xu, and C. Wang, “Suppression of Jahn – Teller distortion of spinel LiMn₂O₄ cathode,” *J. Alloys Compd.*, vol. 479, pp. 310–313, 2009.
- [54] K. Mizushima, P. C. Jones, P. J. Wiseman, and J. B. Goodenough, “A NEW CATHODE MATERIAL FOR BATTERIES OF HIGH ENERGY DENSITY,” *Mater. Res. Bull.*, vol. 15, pp. 783–789, 1980.
- [55] Z. Liu, A. Yu, and J. Y. Lee, “Synthesis and characterization of LiNi_{1-x-y}Co_xMn_yO₂ as the cathode materials of secondary lithium batteries,” *J. Power Sources*, vol. 81–82, pp. 416–419, 1999.
- [56] C. Julien, A. Mauger, K. Zaghib, and H. Groult, “Optimization of layered cathode materials for lithium-ion batteries,” *Materials (Basel)*, vol. 9, no. 7, 2016.
- [57] K. A. Jarvis, Z. Deng, L. F. Allard, A. Manthiram, and P. J. Ferreira, “Atomic Structure of a Lithium-Rich Layered Oxide Material for Lithium-Ion Batteries : Evidence of a Solid Solution,” *Chem. Mater.*, no. 23, pp. 3614–3621, 2011.
- [58] M. M. Thackeray, C. S. Johnson, J. T. Vaughey, N. Li, and S. A. Hackney, “Advances in manganese-oxide ‘ composite ’ electrodes for lithium-ion batteries,” *J. Mater. Chem.*, vol. 15, pp. 2257–2267, 2005.
- [59] J. B. Bates *et al.*, “Fabrication and characterization of amorphous lithium electrolyte thin films and rechargeable thin-film batteries,” *J. Power Sources*, vol. 43, pp. 103–110, 1993.

- [60] F. Mattelaer, P. M. Vereecken, J. Dendooven, and C. Detavernier, "The Influence of Ultrathin Amorphous ALD Alumina and Titania on the Rate Capability of Anatase TiO₂ and LiMn₂O₄ Lithium Ion Battery Electrodes," *Adv. Mater. Interfaces*, vol. 4, no. 13, pp. 1–11, 2017.
- [61] S. Lee *et al.*, "Li₃PO₄ surface coating on Ni-rich LiNi_{0.6}Co_{0.2}Mn_{0.2}O₂ by a citric acid assisted sol-gel method: Improved thermal stability and high-voltage performance," *J. Power Sources*, vol. 360, pp. 206–214, 2017.
- [62] X. Xiong, Z. Wang, H. Guo, Q. Zhang, and X. Li, "Enhanced electrochemical properties of lithium-reactive V₂O₅ coated on the LiNi_{0.8}Co_{0.1}Mn_{0.1}O₂ cathode material for lithium ion batteries at 60C," *J. Mater. Chem. A*, vol. 1, pp. 1284–1288, 2013.
- [63] M. K. Devaraju and I. Honma, "Hydrothermal and solvothermal process towards development of LiMPO₄ (M = Fe, Mn) nanomaterials for lithium-ion batteries," *Adv. Energy Mater.*, vol. 2, no. 3, pp. 284–297, 2012.
- [64] P. Hou, H. Zhang, Z. Zi, L. Zhang, and X. Xu, "Core-shell and concentration-gradient cathodes prepared via co-precipitation reaction for advanced lithium-ion batteries," *J. Mater. Chem. A*, vol. 5, no. 9, pp. 4254–4279, 2017.
- [65] Y. Liu *et al.*, "Architecturing hierarchical function layers on self-assembled viral templates as 3D nano-array electrodes for integrated Li-ion microbatteries," *Nano Lett.*, vol. 13, no. 1, pp. 293–300, 2013.
- [66] C. Zhu, Y. Fu, and Y. Yu, "Designed Nanoarchitectures by Electrostatic Spray Deposition for Energy Storage," *Adv. Mater.*, vol. 31, no. 1, pp. 1–25, 2019.
- [67] W. Lu *et al.*, "Recent Progresses and Development of Advanced Atomic Layer Deposition towards High-Performance Li-Ion Batteries," *Nanomaterials*, vol. 7, no. 10, p. 325, 2017.
- [68] W. Pfleging, "A review of laser electrode processing for development and manufacturing of lithium-ion batteries," *Nanophotonics*, vol. 7, no. 3, pp. 549–573, 2017.
- [69] C. Chen, R. A. Eichel, and P. H. L. Notten, "Metal-organic chemical vapor deposition enabling all-solid-state Li-ion microbatteries: A short review," *J. Electroceramics*, vol. 38, no. 2–4, pp. 230–247, 2017.
- [70] B. Yan, J. Liu, B. Song, P. Xiao, and L. Lu, "Li-rich thin film cathode prepared by pulsed laser deposition," *Sci. Rep.*, vol. 3, no. 003, pp. 3–7, 2013.

- [71] J. Joseph, A. T. Murdock, D. H. Seo, Z. J. Han, A. P. O. Mullane, and K. K. Ostrikov, "Plasma Enabled Synthesis and Processing of Materials for Lithium-Ion Batteries," *Adv. Mater. Technol.*, vol. 3, no. 1800070, pp. 1–19, 2018.
- [72] Y. N. Zhou, M. Z. Xue, and Z. W. Fu, "Nanostructured thin film electrodes for lithium storage and all-solid-state thin-film lithium batteries," *J. Power Sources*, vol. 234, pp. 310–332, 2013.
- [73] Y. Zhou and Z. W. Fu, "Nanostructured Thin film Electrode Materials for Lithium Ion Battery," *Prog. Chem.*, vol. 23, no. 3, pp. 337–348, 2011.
- [74] J. Sun, K. Tang, X. Yu, H. Li, and X. Huang, "Needle-like LiFePO₄ thin films prepared by an off-axis pulsed laser deposition technique," *Thin Solid Films*, vol. 517, no. 8, pp. 2618–2622, 2009.
- [75] F. Sauvage, E. Baudrin, L. Gengembre, and J. M. Tarascon, "Effect of texture on the electrochemical properties of LiFePO₄ thin films," *Solid State Ionics*, vol. 176, no. 23–24, pp. 1869–1876, 2005.
- [76] Z. Qi, J. Tang, J. Huang, D. Zemlyanov, V. G. Pol, and H. Wang, "Li₂MnO₃ Thin Films with Tilted Domain Structure as Cathode for Li-Ion Batteries," *ACS Appl. Energy Mater.*, vol. 2, no. 5, pp. 3461–3468, 2019.
- [77] S. Taminato *et al.*, "Highly reversible capacity at the surface of a lithium-rich manganese oxide: a model study using an epitaxial film system.," *Chem. Commun. (Camb.)*, vol. 51, no. 9, pp. 1673–6, 2015.
- [78] V. K. Vendra, T. Q. Nguyen, A. K. Thapa, J. B. Jasinski, and M. K. Sunkara, "Scalable synthesis and surface stabilization of Li₂MnO₃ NWs as high rate cathode materials for Li-ion batteries," *RSC Adv.*, vol. 5, pp. 36906–36912, 2015.
- [79] M. Cheng, W. Tang, Y. Sun, and K. Zhu, "Electrochemical properties of Li₂MnO₃ nanocrystals synthesized using a hydrothermal method," *RSC Adv.*, vol. 5, pp. 71088–71094, 2015.
- [80] H. Xia, Y. Wan, W. Assenmacher, W. Mader, G. Yuan, and L. Lu, "Facile synthesis of chain-like LiCoO₂ nanowire arrays as three-dimensional cathode for microbatteries," *NPG Asia Mater.*, vol. 6, no. 9, p. e126, 2014.

- [81] K. Senthil, G. Kwak, and K. Yong, "Fabrication of superhydrophobic vanadium pentoxide nanowires surface by chemical modification," *Appl. Surf. Sci.*, vol. 258, no. 19, pp. 7455–7459, 2012.
- [82] M. Prześniak-Welenc *et al.*, "Electrical conductivity and relaxation processes in V_2O_5 nanorods prepared by sol-gel method," *Phys. Status Solidi Basic Res.*, vol. 252, no. 9, pp. 2111–2116, 2015.
- [83] V. Goyal, N. Choudhary, K. Singh, and D. Kaur, "Structural and optical properties of (001)-oriented vanadium pentoxide nanorods," *Nanomater. Energy*, vol. 4, no. 1, pp. 54–63, 2015.
- [84] C. H. Chen, E. M. Kelder, and J. Schoonman, "Unique porous LiCoO₂ thin layers prepared by electrostatic spray deposition," *J. Mater. Sci.*, vol. 31, no. 20, pp. 5437–5442, 1996.
- [85] J. Ma and Q. Z. Qin, "Electrochemical performance of nanocrystalline LiMPO₄ thin-films prepared by electrostatic spray deposition," *J. Power Sources*, vol. 148, no. 1–2, pp. 66–71, 2005.
- [86] D. Shu, K. Y. Chung, W. Il Cho, and K. B. Kim, "Electrochemical investigations on electrostatic spray deposited LiMn₂O₄ films," *J. Power Sources*, vol. 114, no. 2, pp. 253–263, 2003.
- [87] C. H. Chen, A. A. J. Buysman, E. M. Kelder, and J. Schoonman, "Fabrication of LiCoO₂ thin film cathodes for rechargeable lithium battery by electrostatic spray pyrolysis," *Solid State Ionics*, vol. 80, no. 1–2, pp. 1–4, 1995.
- [88] Y. T. Kim, S. Gopukumar, K. B. Kim, and B. W. Cho, "Performance of electrostatic spray-deposited vanadium pentoxide in lithium secondary cells," *J. Power Sources*, vol. 117, no. 1–2, pp. 110–117, 2003.
- [89] J. L. Shui, G. S. Jiang, S. Xie, and C. H. Chen, "Thin films of lithium manganese oxide spinel as cathode materials for secondary lithium batteries," *Electrochim. Acta*, vol. 49, no. 13, pp. 2209–2213, 2004.
- [90] U. Lafont, A. Anastasopol, E. Garcia-Tamayo, and E. Kelder, "Electrostatic spray pyrolysis of LiNi_{0.5}Mn_{1.5}O₄ films for 3D Li-ion microbatteries," *Thin Solid Films*, vol. 520, no. 9, pp. 3464–3471, 2012.

- [91] S. Koike and K. Tatsumi, "Preparation and performances of highly porous layered LiCoO₂ films for lithium batteries," *J. Power Sources*, vol. 174, no. 2, pp. 976–980, 2007.
- [92] S. Wang, S. Li, Y. Sun, X. Feng, and C. Chen, "Three-dimensional porous V₂O₅ cathode with ultra high rate capability," *Energy Environ. Sci.*, vol. 4, no. 8, pp. 2854–2857, 2011.
- [93] J. Mosa, M. Aparicio, A. Durán, C. Laberty-Robert, and C. Sanchez, "Nanocrystalline mesoporous LiFePO₄ thin-films as cathodes for Li-ion microbatteries," *J. Mater. Chem. A*, vol. 2, no. 9, pp. 3038–3046, 2014.
- [94] A. Yamada, H. Koizumi, N. Sonoyama, and R. Kanno, "Phase Change in Li_xFePO₄," *Electrochem. Solid-State Lett.*, vol. 8, no. 8, p. A409, 2006.
- [95] S. W. Oh, S.-T. Myung, H. J. Bang, C. S. Yoon, K. Amine, and Y.-K. Sun, "Nanoporous Structured LiFePO₄ with Spherical Microscale Particles Having High Volumetric Capacity for Lithium Batteries," *Electrochem. Solid-State Lett.*, vol. 12, no. 9, p. A181, 2009.
- [96] B. G. Park, S. Kim, I. D. Kim, and Y. J. Park, "Structural and electrochemical performance of three-dimensional LiMn₂O₄ thin film," *J. Mater. Sci.*, vol. 45, no. 14, pp. 3947–3953, 2010.
- [97] C. H. Mi, Y. X. Cao, X. G. Zhang, X. B. Zhao, and H. L. Li, "Synthesis and characterization of LiFePO₄/(Ag + C) composite cathodes with nano-carbon webs," *Powder Technol.*, vol. 181, no. 3, pp. 301–306, 2008.
- [98] D. Yu *et al.*, "Mica-like vanadium pentoxide-nanostructured thin film as high-performance cathode for lithium-ion batteries," *J. Power Sources*, vol. 266, pp. 1–6, 2014.
- [99] H. Xia, Q. Xia, B. Lin, J. Zhu, J. K. Seo, and Y. S. Meng, "Self-standing porous LiMn₂O₄ nanowall arrays as promising cathodes for advanced 3D microbatteries and flexible lithium-ion batteries," *Nano Energy*, vol. 22, pp. 475–482, 2016.
- [100] M. Bettge *et al.*, "Hierarchically textured Li_xMn_{2-y}O₄ thin films as positive electrodes for lithium-ion batteries," *J. Power Sources*, vol. 206, pp. 288–294, 2012.
- [101] M. Bettge *et al.*, "Low-temperature vapour-liquid-solid (VLS) growth of vertically aligned silicon oxide nanowires using concurrent ion bombardment," *Nanotechnology*, vol. 20, no. 11, 2009.

- [102] T. Aoshima, K. Okahara, C. Kiyohara, and K. Shizuka, "Mechanisms of manganese spinels dissolution and capacity fade at high temperature," *J. Power Sources*, vol. 97–98, pp. 377–380, 2001.
- [103] G. P. Pandey, S. A. Klankowski, T. Liu, J. Wu, and J. Li, "Toward highly stable solid-state unconventional thin-film battery-supercapacitor hybrid devices: Interfacing vertical core-shell array electrodes with a gel polymer electrolyte," *J. Power Sources*, vol. 342, pp. 1006–1016, 2017.
- [104] M. M. Shaijumon, E. Perre, B. Daffos, P. L. Taberna, J. M. Tarascon, and P. Simon, "Nanoarchitected 3D cathodes for Li-ion microbatteries," *Adv. Mater.*, vol. 22, no. 44, pp. 4978–4981, 2010.
- [105] E. Perre, L. Nyholm, T. Gustafsson, P. L. Taberna, P. Simon, and K. Edström, "Direct electrodeposition of aluminium nano-rods," *Electrochem. commun.*, vol. 10, no. 10, pp. 1467–1470, 2008.
- [106] H. Yim *et al.*, "Three-dimensional hemisphere-structured $\text{LiSn}_{0.0125}\text{Mn}_{1.975}\text{O}_4$ thin-film cathodes," *Electrochem. commun.*, vol. 43, pp. 36–39, 2014.
- [107] F. Mattelaer, K. Geryl, G. Rampelberg, J. Dendooven, and C. Detavernier, "Amorphous and Crystalline Vanadium Oxides as High-Energy and High-Power Cathodes for Three-Dimensional Thin-Film Lithium Ion Batteries," *ACS Appl. Mater. Interfaces*, vol. 9, no. 15, pp. 13121–13131, 2017.
- [108] R. F. Balderas-Valadez *et al.*, "Porous silicon pillar and bilayer structure as a nucleation center for the formation of aligned vanadium pentoxide nanorods," *Ceram. Int.*, vol. 43, no. 11, pp. 8023–8030, 2017.
- [109] J. Cai, Q. Sun, and X. Meng, "Novel nanostructured materials by atomic and molecular layer deposition," *AIMS Mater. Sci.*, vol. 5, no. 5, pp. 957–999, 2018.
- [110] M. Mäntymäki, M. Ritala, and M. Leskelä, "Metal Fluorides as Lithium-Ion Battery Materials: An Atomic Layer Deposition Perspective," *Coatings*, vol. 8, no. 8, p. 277, 2018.
- [111] K. Gerasopoulos *et al.*, "Hierarchical three-dimensional microbattery electrodes combining bottom-up self-assembly and top-down micromachining," *ACS Nano*, vol. 6, no. 7, pp. 6422–6432, 2012.

- [112] Y. H. Ding, H. M. Ren, Y. Y. Huang, F. H. Chang, and P. Zhang, “Three-dimensional graphene/LiFePO₄ nanostructures as cathode materials for flexible lithium-ion batteries,” *Mater. Res. Bull.*, vol. 48, no. 10, pp. 3713–3716, 2013.
- [113] J. Z. Wang *et al.*, “Development of MoS₂-CNT composite thin film from layered MoS₂ for lithium batteries,” *Adv. Energy Mater.*, vol. 3, no. 6, pp. 798–805, 2013.
- [114] F. S. Gittleson *et al.*, “Ultrathin Nanotube/Nanowire Electrodes by Spin-Spray Layer-by-Layer Assembly: A Concept for Transparent Energy Storage,” *ACS Nano*, vol. 9, no. 10, pp. 10005–10017, 2015.
- [115] K. H. Seng, J. Liu, Z. P. Guo, Z. X. Chen, D. Jia, and H. K. Liu, “Free-standing V₂O₅ electrode for flexible lithium ion batteries,” *Electrochem. commun.*, vol. 13, no. 5, pp. 383–386, 2011.
- [116] Y. Zhang *et al.*, “A Safe High-Performance All-Solid-State Lithium-Vanadium Battery with a Freestanding V₂O₅ Nanowire Composite Paper Cathode,” *ACS Appl. Mater. Interfaces*, vol. 8, no. 50, pp. 34309–34316, 2016.
- [117] M. Sathiya, A. S. Prakash, K. Ramesha, J. M. Tarascon, and A. K. Shukla, “V₂O₅-anchored carbon nanotubes for enhanced electrochemical energy storage,” *J. Am. Chem. Soc.*, vol. 133, no. 40, pp. 16291–16299, 2011.
- [118] X. Chen *et al.*, “MWCNT/V₂O₅ core/shell sponge for high areal capacity and power density Li-ion cathodes,” *ACS Nano*, vol. 6, no. 9, pp. 7948–7955, 2012.
- [119] E. Brown, J. Acharya, G. P. Pandey, J. Wu, and J. Li, “Highly Stable Three Lithium Insertion in Thin V₂O₅ Shells on Vertically Aligned Carbon Nanofiber Arrays for Ultrahigh-Capacity Lithium Ion Battery Cathodes,” *Adv. Mater. Interfaces*, vol. 3, no. 23, pp. 1–11, 2016.
- [120] E. Brown *et al.*, “Facilitating high-capacity V₂O₅ cathodes with stable two and three Li⁺ insertion using a hybrid membrane structure consisting of amorphous V₂O₅ shells coaxially deposited on electrospun carbon nanofibers,” *Electrochim. Acta*, vol. 269, pp. 144–154, 2018.
- [121] M. Chen, X. Liang, F. Wang, D. Xie, G. Pan, and X. Xia, “Self-supported VO₂ arrays decorated with N-doped carbon as an advanced cathode for lithium-ion storage,” *J. Mater. Chem. A*, vol. 7, no. 12, pp. 6644–6650, 2019.

- [122] N. Li, Z. Chen, W. Ren, F. Li, and H.-M. Cheng, "Flexible graphene-based lithium ion batteries with ultrafast charge and discharge rates," *Proc. Natl. Acad. Sci.*, vol. 109, no. 43, pp. 17360–17365, 2012.
- [123] H. Ma, J. Xiang, and X. Xia, "Graphene foam supported LiFePO₄ nanosheets composite as advanced cathode for lithium ion batteries," *Mater. Res. Bull.*, vol. 101, no. January, pp. 205–209, 2018.
- [124] H. C. M. Knoop, M. E. Donders, M. C. M. van de Sanden, P. H. L. Notten, and W. M. M. Kessels, "Atomic layer deposition for nanostructured Li-ion batteries," *J. Vac. Sci. Technol. A Vacuum, Surfaces, Film.*, vol. 30, no. 1, p. 010801, 2011.
- [125] K. B. Gandrud, "Thin film materials for Li-ion batteries made by atomic layer deposition," 2014.
- [126] L. Ma, R. B. Nuwayhid, T. Wu, Y. Lei, K. Amine, and J. Lu, "Atomic Layer Deposition for Lithium-Based Batteries," *Adv. Mater. Interfaces*, vol. 3, no. 21, 2016.
- [127] R. Kohler, P. Smyrek, S. Ulrich, V. Trouillet, and W. Pfleging, "Patterning and annealing of nanocrystalline LiCoO₂ thin films," *J. Optoelectron. Adv. Mater.*, vol. 12, no. 3, pp. 547–552, 2010.
- [128] J. Pröll *et al.*, "Laser modification and characterization of Li-Mn-O thin film cathodes for lithium-ion batteries," *Laser-based Micro- Nanopackaging Assem. V*, vol. 7921, p. 79210Q, 2011.
- [129] J. Pröll *et al.*, "Laser adjusted three-dimensional Li-Mn-O cathode architectures for secondary lithium-ion cells," in *Laser-based Micro- and Nanopackaging and Assembly VI*, 2012, vol. 8244, no. February 2012, p. 82440S.
- [130] R. Kohler, J. Proell, M. Bruns, S. Ulrich, H. J. Seifert, and W. Pfleging, "Conical surface structures on model thin-film electrodes and tape-cast electrode materials for lithium-ion batteries," *Appl. Phys. A Mater. Sci. Process.*, vol. 112, no. 1, pp. 77–85, 2013.
- [131] C. Hudaya *et al.*, "A polymerized C₆₀ coating enhancing interfacial stability at three-dimensional LiCoO₂ in high-potential regime," *J. Power Sources*, vol. 298, pp. 1–7, 2015.
- [132] J. Pröll *et al.*, "Diode laser heat treatment of lithium manganese oxide films," *Appl. Surf. Sci.*, vol. 258, no. 12, pp. 5146–5152, 2012.

- [133] S. R. Li *et al.*, “Three-dimensional porous Fe_{0.1}V₂O_{5.15} thin film as a cathode material for lithium ion batteries,” *Electrochim. Acta*, vol. 64, pp. 81–86, 2012.
- [134] N. F. Uvarov, “Estimation of composites conductivity using a general mixing rule,” *Solid State Ionics*, vol. 136–137, pp. 1267–1272, 2000.
- [135] A. R. Armstrong *et al.*, “Demonstrating oxygen loss and associated structural reorganization in the lithium battery cathode Li[Ni_{0.2}Li_{0.2}Mn_{0.6}]O₂,” *J. Am. Chem. Soc.*, vol. 128, no. 26, pp. 8694–8698, 2006.
- [136] T. Teranishi *et al.*, “Low-Temperature High-Rate Capabilities of Lithium Batteries via Polarization-Assisted Ion Pathways,” *Adv. Electron. Mater.*, vol. 4, no. 4, pp. 1–7, 2018.
- [137] J. Song, S. Jacke, D. Becker, and R. Hausbrand, “Stabilization of Thin Film LiCoO₂ Electrode by LiPON Coating,” *Electrochem. Solid-State Lett.*, vol. 14, no. 2, pp. A11–A13, 2011.
- [138] Y. Kobayashi *et al.*, “5 V Class All-Solid-State Composite Lithium Battery with Li₃PO₄ Coated LiNi_{0.5}Mn_{1.5}O₄,” *J. Electrochem. Soc.*, vol. 150, no. 12, p. A1577, 2003.
- [139] I. Belharouak, C. Johnson, and K. Amine, “Synthesis and electrochemical analysis of vapor-deposited carbon-coated LiFePO₄,” *Electrochem. commun.*, vol. 7, no. 10, pp. 983–988, 2005.
- [140] A. Bünting, S. Uhlenbruck, D. Sebold, H. P. Buchkremer, and R. Vaßen, “Three-Dimensional, Fibrous Lithium Iron Phosphate Structures Deposited by Magnetron Sputtering,” *ACS Appl. Mater. Interfaces*, vol. 7, no. 40, pp. 22594–22600, 2015.
- [141] K. Xie *et al.*, “Nitrogen-doped carbon-wrapped porous single-crystalline CoO nanocubes for high-performance lithium storage,” *ACS Appl. Mater. Interfaces*, vol. 6, no. 13, pp. 10602–10607, 2014.
- [142] Z. Ding *et al.*, “Towards understanding the effects of carbon and nitrogen-doped carbon coating on the electrochemical performance of Li₄Ti₅O₁₂ in lithium ion batteries: A combined experimental and theoretical study,” *Phys. Chem. Chem. Phys.*, vol. 13, no. 33, pp. 15127–15133, 2011.
- [143] D. Xie *et al.*, “Exploring Advanced Sandwiched Arrays by Vertical Graphene and N-Doped Carbon for Enhanced Sodium Storage,” *Adv. Energy Mater.*, vol. 7, no. 3, 2017.

- [144] G. X. Pan, F. Cao, Y. J. Zhang, and X. H. Xia, "Integrated carbon cloth supported LiFePO₄/N-C films as high-performance cathode for lithium ion batteries," *Mater. Res. Bull.*, vol. 98, no. September 2017, pp. 70–76, 2018.
- [145] X. Xia *et al.*, "VO₂ nanoflake arrays for supercapacitor and Li-ion battery electrodes: Performance enhancement by hydrogen molybdenum bronze as an efficient shell material," *Mater. Horizons*, vol. 2, no. 2, pp. 237–244, 2015.
- [146] Z.-B. Zhou, M. Takeda, T. Fujii, and M. Ue, "Li[C₂F₅BF₃] as an Electrolyte Salt for 4 V Class Lithium-Ion Cells," *J. Electrochem. Soc.*, vol. 152, no. 2, p. A351, 2005.
- [147] J. L. Tebbe, A. M. Holder, and C. B. Musgrave, "Mechanisms of LiCoO₂ Cathode Degradation by Reaction with HF and Protection by Thin Oxide Coatings," *ACS Appl. Mater. Interfaces*, vol. 7, no. 43, pp. 24265–24278, 2015.
- [148] J. Liu, B. Wang, Q. Sun, R. Li, T. K. Sham, and X. Sun, "Atomic Layer Deposition of Hierarchical CNTs@FePO₄ Architecture as a 3D Electrode for Lithium-Ion and Sodium-Ion Batteries," *Adv. Mater. Interfaces*, vol. 3, no. 21, 2016.
- [149] S. Kim, J. Liu, K. Sun, J. Wang, S. J. Dillon, and P. V. Braun, "Improved Performance in FeF₂ Conversion Cathodes through Use of a Conductive 3D Scaffold and Al₂O₃ ALD Coating," *Adv. Funct. Mater.*, vol. 27, no. 35, pp. 1–8, 2017.
- [150] Z. Chen, Y. Qin, K. Amine, and Y. K. Sun, "Role of surface coating on cathode materials for lithium-ion batteries," *J. Mater. Chem.*, vol. 20, no. 36, pp. 7606–7612, 2010.
- [151] K.-F. Chiu, "Optimization of Synthesis Process for Carbon-Mixed LiFePO₄ Composite Thin-Film Cathodes Deposited by Bias Sputtering," *J. Electrochem. Soc.*, vol. 154, no. 2, p. A129, 2007.
- [152] K.-F. Chiu, H.-Y. Tang, and B.-S. Lin, "High Conductivity LiFePO₄/C Composite Thin Films with Ti Underlayers Deposited by Radio Frequency Sputtering," *J. Electrochem. Soc.*, vol. 154, no. 4, p. A364, 2007.
- [153] Z. G. Lu, M. F. Lo, and C. Y. Chung, "Pulse laser deposition and electrochemical characterization of LiFePO₄-C composite thin films," *J. Phys. Chem. C*, vol. 112, no. 17, pp. 7069–7078, 2008.

- [154] N. Zhou, E. Uchaker, Y. Y. Liu, S. Q. Liu, Y. N. Liu, and G. Z. Cao, "Effect of carbon content on electrochemical performance of LiFePO₄/C thin film cathodes," *Int. J. Electrochem. Sci.*, vol. 7, no. 12, pp. 12633–12645, 2012.
- [155] Z. G. Lu, C. Hua, M. F. Lo, and C. Y. Chung, "Pulse laser deposition and electrochemical characterization of LiFePO₄-Ag composite thin films," *Adv. Funct. Mater.*, vol. 17, no. 118, pp. 3885–3896, 2007.
- [156] A. Eftekhari, "Electrochemical Deposition and Modification of LiFePO₄ for the Preparation of Cathode with Enhanced Battery Performance," *J. Electrochem. Soc.*, vol. 151, no. 11, p. A1816, 2004.
- [157] A. Eftekhari, "Mixed-Metals Codeposition as a Novel Method for the Preparation of LiMn₂O₄ Electrodes with Reduced Capacity Fades," *J. Electrochem. Soc.*, vol. 150, no. 7, p. A966, 2003.
- [158] A. Eftekhari, "Electrochemical performance and cyclability of LiFe_{0.5}Mn_{1.5}O₄ as a 5 V cathode material for lithium batteries," *J. Power Sources*, vol. 124, no. 1, pp. 182–190, 2003.
- [159] F. Wu, G. Tan, J. Lu, R. Chen, L. Li, and K. Amine, "Stable Nanostructured With Polycrystalline Li-Deficient Li_{0.28}Co_{0.29}Ni_{0.3}Mn_{0.2}O₂ for Lithium-Ion Batteries," *Nano Lett.*, vol. 14, pp. 1281–1287, 2014.
- [160] L. Nation, J. Li, C. James, Y. Qi, N. Dudney, and B. W. Sheldon, "In situ stress measurements during electrochemical cycling of lithium-rich cathodes," *J. Power Sources*, vol. 364, pp. 383–391, 2017.
- [161] F. Huang, Z. wen Fu, and Q. zong Qin, "A novel Li₂Ag_{0.5}V₂O₅ composite film cathode for all-solid-state lithium batteries," *Electrochem. commun.*, vol. 5, no. 3, pp. 262–266, 2003.
- [162] C. Jacob, J. Jian, Q. Su, S. Verkhoturov, R. Guillemette, and H. Wang, "Electrochemical and Structural Effects of In Situ Li₂O Extraction from Li₂MnO₃ for Li-Ion Batteries," *ACS Appl. Mater. Interfaces*, vol. 7, no. 4, pp. 2433–2438, 2015.
- [163] C. Jacob, J. Jian, Y. Zhu, Q. Su, and H. Wang, "A new approach to investigate Li₂MnO₃ and Li(Ni_{0.5}Mn_{0.3}Co_{0.2})O₂ mixed phase cathode materials," *J. Mater. Chem. A*, vol. 2, no. 7, pp. 2283–2289, 2014.

- [164] Z. Qi *et al.*, “LiNi_{0.5}Mn_{0.3}Co_{0.2}O₂/Au nanocomposite thin film cathode with enhanced electrochemical properties,” *Nano Energy*, vol. 46, no. January, pp. 290–296, 2018.
- [165] Q. Shi, R. Hu, L. Ouyang, M. Zeng, and M. Zhu, “High-capacity LiV₃O₈ thin-film cathode with a mixed amorphous-nanocrystalline microstructure prepared by RF magnetron sputtering,” *Electrochem. commun.*, vol. 11, no. 11, pp. 2169–2172, 2009.
- [166] Z. Yu, H. Xu, G. Zhu, D. L. Yan, and A. Yu, “Binary Lithium Titanate–Titania Nanocomposite Thin-Film Electrodes for Electrochemical Energy Storage,” *Energy Technol.*, vol. 4, no. 7, pp. 798–803, 2016.
- [167] X. Yu *et al.*, “Pulsed Laser Deposition and Characterization of Heteroepitaxial LiMn₂O₄/La_{0.5}Sr_{0.5}CoO₃ Bilayer Thin Films as Model Lithium Ion Battery Cathodes,” *ACS Appl. Nano Mater.*, vol. 1, no. 2, pp. 642–653, 2018.
- [168] R. K. Singh, O. W. Holland, J. Narayan, R. K. Singh, O. W. Holland, and J. Narayan, “Theoretical model for deposition of superconducting thin films using pulsed laser evaporation technique Theoretical model for deposition of superconducting thin films using pulsed laser evaporation technique,” *Appl. Phys. Lett.*, vol. 233, no. 1990, 2012.
- [169] D. B. Williams and C. B. Carter, *Transmission Electron Microscopy*, 2nd ed. Springer, 2009.
- [170] O. Tsutomu and M. Yoshinari, “Layered Lithium Insertion Material of LiCo_{1/3}Ni_{1/3}Mn_{1/3}O₂ for Lithium-Ion Batteries,” *Chem. Lett.*, vol. 30, no. 7, pp. 642–643, 2001.
- [171] W. H. Kan, A. Huq, and A. Manthiram, “Exploration of a Metastable Normal Spinel Phase Diagram for the Quaternary Li–Ni–Mn–Co–O System,” *Chem. Mater.*, vol. 28, no. 6, pp. 1832–1837, 2016.
- [172] S.-M. Bak *et al.*, “Structural Changes and Thermal Stability of Charged LiNi_xMn_yCo_zO₂ Cathode Materials Studied by Combined In Situ Time-Resolved XRD and Mass Spectroscopy,” *ACS Appl. Mater. Interfaces*, vol. 6, no. 24, pp. 22594–22601, Dec. 2014.
- [173] S. K. Martha *et al.*, “A comparative study of electrodes comprising nanometric and submicron particles of LiNi_{0.50}Mn_{0.50}O₂, LiNi_{0.33}Mn_{0.33}Co_{0.33}O₂, and LiNi_{0.40}Mn_{0.40}Co_{0.20}O₂ layered compounds,” *J. Power Sources*, vol. 189, no. 1, pp. 248–255, 2009.

- [174] H. M. . B. Wu I; Abouimrane, A. ; Sun, Y. K.; Amine, K., “Surface modification of $\text{LiNi}_0.5\text{Mn}_1.5\text{O}_4$ by ZrP_2O_7 and ZrO_2 for lithium-ion batteries,” vol. 195, no. 9, p. 4.
- [175] Y. Su, S. Cui, Z. Zhuo, W. Yang, X. Wang, and F. Pan, “Enhancing the High-Voltage Cycling Performance of $\text{LiNi}_0.5\text{Mn}_0.3\text{Co}_0.2\text{O}_2$ by Retarding Its Interfacial Reaction with an Electrolyte by Atomic-Layer-Deposited Al_2O_3 ,” *ACS Appl. Mater. Interfaces*, vol. 7, no. 45, pp. 25105–25112, Nov. 2015.
- [176] Z. Wu *et al.*, “Prelithiation Activates $\text{Li}(\text{Ni}_0.5\text{Mn}_0.3\text{Co}_0.2)\text{O}_2$ for High Capacity and Excellent Cycling Stability,” *Nano Lett.*, vol. 15, no. 8, pp. 5590–5596, Aug. 2015.
- [177] M. N. Hang *et al.*, “Impact of Nanoscale Lithium Nickel Manganese Cobalt Oxide (NMC) on the Bacterium *Shewanella oneidensis* MR-1,” *Chem. Mater.*, vol. 28, no. 4, pp. 1092–1100, 2016.
- [178] M. Metzger *et al.*, “Carbon Coating Stability on High-Voltage Cathode Materials in H_2O -Free and H_2O -Containing Electrolyte,” *J. Electrochem. Soc.*, vol. 162, no. 7, pp. A1227–A1235, 2015.
- [179] H.-K. Song, K. T. Lee, M. G. Kim, L. F. Nazar, and J. Cho, “Recent Progress in Nanostructured Cathode Materials for Lithium Secondary Batteries,” *Adv. Funct. Mater.*, vol. 20, no. 22, pp. 3818–3834, 2010.
- [180] D. Deng, “Li-ion batteries: basics, progress, and challenges,” *Energy Sci. Eng.*, vol. 3, no. 5, pp. 385–418, 2015.
- [181] X. Yu, J. B. Bates, G. E. Jellison, and F. X. Hart, “A Stable Thin-Film Lithium Electrolyte: Lithium Phosphorus Oxynitride,” *J. Electrochem. Soc.*, vol. 144, no. 2, pp. 524–532, 1997.
- [182] J. B. Bates, N. J. Dudney, B. Neudecker, A. Ueda, and C. D. Evans, “Thin-film lithium and lithium-ion batteries,” *Solid State Ionics*, vol. 135, no. 1–4, pp. 33–45, 2000.
- [183] J. L. Souquet and M. Duclot, “Thin film lithium batteries,” *Solid State Ionics*, vol. 148, no. 3–4, pp. 375–379, 2002.
- [184] C. V Ramana, K. Zaghib, and C. M. Julien, “Highly oriented growth of pulsed-laser deposited $\text{LiNi}_0.8\text{Co}_0.2\text{O}_2$ films for application in microbatteries,” *Chem. Mater.*, vol. 18, no. 6, pp. 1397–1400, 2006.

- [185] J. F. M. Oudenhoven, L. Baggetto, and P. H. L. Notten, "All-Solid-State Lithium-Ion Microbatteries: A Review of Various Three-Dimensional Concepts," *Adv. Energy Mater.*, vol. 1, no. 1, pp. 10–33, 2011.
- [186] G. R. Hardin, Y. Zhang, C. D. Fincher, and M. Pharr, "Interfacial Fracture of Nanowire Electrodes of Lithium-Ion Batteries," *JOM*, Jun. 2017.
- [187] M. Antaya, J. R. Dahn, J. S. Preston, E. Rossen, and J. N. Reimers, "Preparation and Characterization of LiCoO₂ Thin Films by Laser Ablation Deposition," *J. Electrochem. Soc.*, vol. 140, no. 3, pp. 575–578, 1993.
- [188] J. B. Bates, N. J. Dudney, B. J. Neudecker, F. X. Hart, H. P. Jun, and S. A. Hackney, "Preferred Orientation of Polycrystalline LiCoO₂ Films," *J. Electrochem. Soc.*, vol. 147, no. 1, pp. 59–70, 2000.
- [189] Z. Shi, L. Lü, and G. Ceder, "Solid State thin film lithium microbatteries," 2003.
- [190] T. Kato *et al.*, "Effects of sintering temperature on interfacial structure and interfacial resistance for all-solid-state rechargeable lithium batteries," *J. Power Sources*, vol. 325, pp. 584–590, 2016.
- [191] Z. G. Lu, H. Cheng, M. F. Lo, and C. Y. Chung, "Pulsed Laser Deposition and Electrochemical Characterization of LiFePO₄–Ag Composite Thin Films," *Adv. Funct. Mater.*, vol. 17, no. 18, pp. 3885–3896, 2007.
- [192] Z. G. Lu, M. F. Lo, and C. Y. Chung, "Pulse Laser Deposition and Electrochemical Characterization of LiFePO₄–C Composite Thin Films," *J. Phys. Chem. C*, vol. 112, no. 17, pp. 7069–7078, 2008.
- [193] K. F. Chiu and C. L. Chen, "Electrochemical performance of magnetron sputter deposited LiFePO₄–Ag composite thin film cathodes," *Surf. Coatings Technol.*, vol. 205, no. 5, pp. 1642–1646, 2010.
- [194] L. Li *et al.*, "Self-Assembled Epitaxial Au–Oxide Vertically Aligned Nanocomposites for Nanoscale Metamaterials," *Nano Lett.*, vol. 16, no. 6, pp. 3936–3943, Jun. 2016.
- [195] J. Huang *et al.*, "Self-assembled Co–BaZrO₃ nanocomposite thin films with ultra-fine vertically aligned Co nanopillars," *Nanoscale*, vol. 9, no. 23, pp. 7970–7976, 2017.
- [196] S. C. Mui *et al.*, "Block Copolymer-Templated Nanocomposite Electrodes for Rechargeable Lithium Batteries," *J. Electrochem. Soc.*, vol. 149, no. 12, pp. A1610–A1615, 2002.

- [197] F. U. Renner *et al.*, “Gold model anodes for Li-ion batteries: Single crystalline systems studied by in situ X-ray diffraction,” *Electrochim. Acta*, vol. 53, no. 21, pp. 6064–6069, 2008.
- [198] J. C. Garcia *et al.*, “Surface Structure, Morphology, and Stability of $\text{Li}(\text{Ni}_{1/3}\text{Mn}_{1/3}\text{Co}_{1/3})\text{O}_2$ Cathode Material,” *J. Phys. Chem. C*, vol. 121, no. 15, pp. 8290–8299, 2017.
- [199] C. Julien, A. Mauger, K. Zaghib, and H. Groult, “Optimization of Layered Cathode Materials for Lithium-Ion Batteries,” *Materials (Basel)*, vol. 9, no. 7, p. 595, 2016.
- [200] C. Jacob, T. Lynch, A. Chen, J. Jian, and H. Wang, “Highly textured $\text{Li}(\text{Ni}_{0.5}\text{Mn}_{0.3}\text{Co}_{0.2})\text{O}_2$ thin films on stainless steel as cathode for lithium-ion battery,” *J. Power Sources*, vol. 241, pp. 410–414, 2013.
- [201] N. Choi, J. Han, S. Ha, I. Park, and C.-K. Back, “Recent advances in the electrolytes for interfacial stability of high-voltage cathodes in lithium-ion batteries,” *RSC Adv.*, vol. 5, pp. 2732–2748, 2014.
- [202] Y. Yoon, C. Park, J. Kim, and D. Shin, “Lattice orientation control of lithium cobalt oxide cathode film for all-solid-state thin film batteries,” *J. Power Sources*, vol. 226, no. 15, pp. 186–190, 2013.
- [203] S. F. Amalraj *et al.*, “Study of the nanosized Li_2MnO_3 : Electrochemical behavior, structure, magnetic properties, and vibrational modes,” *Electrochim. Acta*, vol. 97, pp. 259–270, 2013.
- [204] F. Yang, Q. Zhang, X. Hu, T. Peng, and J. Liu, “Preparation of Li-rich layered-layered type $x\text{Li}_2\text{MnO}_3 \cdot (1-x)\text{LiMnO}_2$ nanorods and its electrochemical performance as cathode material for Li-ion battery,” *J. Power Sources*, vol. 353, no. May, pp. 323–332, 2017.
- [205] S. H. Park, Y. Sato, J. K. K. Kim, and Y. S. Lee, “Powder property and electrochemical characterization of Li_2MnO_3 material,” *Mater. Chem. Phys.*, vol. 102, no. 2–3, pp. 225–230, 2007.
- [206] M. Roberts *et al.*, “3D lithium ion batteries—from fundamentals to fabrication,” *J. Mater. Chem.*, vol. 21, no. 27, p. 9876, 2011.
- [207] Y. Wang *et al.*, “Lithium and lithium ion batteries for applications in microelectronic devices: A review,” *J. Power Sources*, vol. 286, pp. 330–345, 2015.

- [208] J. Y. Zheng, R. Wang, and H. Li, "Fabrication and electrochemical behavior of a pure-phase Li_2MnO_3 thin film for cathode material of Li-Ion batteries," *Acta Phys. -Chim. Sin.*, vol. 30, no. 10, pp. 1855–1860, 2014.
- [209] T. S. Arthur *et al.*, "Three-dimensional electrodes and battery architectures," *MRS Bull.*, vol. 36, no. 7, pp. 523–531, 2011.
- [210] Y. Sugawara *et al.*, "Interfacial Atomic Structures of Single-Phase Li_2MnO_3 Thin Film with Superior Initial Charge-Discharge Behavior," *J. Electrochem. Soc.*, vol. 165, no. 2, pp. A55–A60, 2018.
- [211] J. W. Long, B. Dunn, D. R. Rolison, and H. S. White, "Three-dimensional battery architectures," *Chem. Rev.*, vol. 104, no. 10, pp. 4463–4492, 2004.
- [212] G. Oltean, H. Desta Asfaw, L. Nyholm, and K. Edström, "A Li-Ion Microbattery with 3D Electrodes of Different Geometries," *ECS Electrochem. Lett.*, vol. 3, no. 6, pp. A54–A57, 2014.
- [213] Y. Zargouni *et al.*, "Electrodeposition and Characterization of Manganese Dioxide Thin Films on Silicon Pillar Arrays for 3D Thin-Film Lithium-Ion Batteries," *ECS Trans.*, vol. 61, no. 9, pp. 29–41, 2014.
- [214] M. Armand and J.-M. Tarascon, "Building better batteries," *Nature*, vol. 451, no. February, pp. 2–7, 2008.
- [215] X. Qian, Q. Xu, T. Hang, S. Shanmugam, and M. Li, "Electrochemical deposition of Fe_3O_4 nanoparticles and flower-like hierarchical porous nanoflakes on 3D Cu-cone arrays for rechargeable lithium battery anodes," *Mater. Des.*, vol. 121, pp. 321–334, 2017.
- [216] Y. Zargouni, S. Deheryan, A. Radisic, K. Alouani, and P. Vereecken, "Electrolytic Manganese Dioxide Coatings on High Aspect Ratio Micro-Pillar Arrays for 3D Thin Film Lithium Ion Batteries," *Nanomaterials*, vol. 7, no. 6, p. 126, 2017.
- [217] C. W. Su, J. M. Li, W. Yang, and J. M. Guo, "Electrodeposition of $\text{Ni}_3\text{S}_2/\text{Ni}$ composites as high-performance cathodes for lithium batteries," *J. Phys. Chem. C*, vol. 118, no. 2, pp. 767–773, 2014.
- [218] J. Xie, J. F. M. Oudenhoven, P.-P. R. M. L. Harks, D. Li, and P. H. L. Notten, "Chemical Vapor Deposition of Lithium Phosphate Thin-Films for 3D All-Solid-State Li-Ion Batteries," *J. Electrochem. Soc.*, vol. 162, no. 3, pp. A249–A254, 2014.

- [219] T. Fujibayashi, Y. Kubota, K. Iwabuchi, and N. Yoshii, "Highly conformal and high-ionic conductivity thin-film electrolyte for 3D-structured micro batteries: Characterization of LiPON film deposited by MOCVD method," *AIP Adv.*, vol. 7, no. 8, pp. 085110–085117, 2017.
- [220] J. Liu, B. Wang, Q. Sun, R. Li, T.-K. Sham, and X. Sun, "Atomic Layer Deposition of Hierarchical CNTs@FePO₄ Architecture as a 3D Electrode for Lithium-Ion and Sodium-Ion Batteries," *Adv. Mater. Interfaces*, vol. 3, no. 21, p. 1600468, 2016.
- [221] A. J. Pearse *et al.*, "Nanoscale Solid State Batteries Enabled by Thermal Atomic Layer Deposition of a Lithium Polyphosphazene Solid State Electrolyte," *Chem. Mater.*, vol. 29, no. 8, pp. 3740–3753, 2017.
- [222] M. Suzuki, "Practical applications of thin films nanostructured by shadowing growth," *J. Nanophotonics*, vol. 7, no. 1, p. 073598, 2013.
- [223] A. Boulineau, L. Croguennec, C. Delmas, and F. Weill, "Reinvestigation of Li₂MnO₃ structure: Electron diffraction and high resolution TEM," *Chem. Mater.*, vol. 21, no. 18, pp. 4216–4222, 2009.
- [224] A. Chen *et al.*, "Tilted Aligned Epitaxial La_{0.7} Sr_{0.3} MnO₃ Nanocolumnar Films with Enhanced Low-Field Magnetoresistance by Pulsed Laser Oblique-Angle Deposition," *Cryst. Growth Des.*, vol. 11, no. 12, pp. 5405–5409, Dec. 2011.
- [225] A. Barranco, A. Borrás, A. R. González-Elipé, and A. Palmero, "Perspectives on oblique angle deposition of thin films: From fundamentals to devices," *Prog. Mater. Sci.*, vol. 76, pp. 59–153, 2016.
- [226] C. Jacob, J. Jian, Y. Zhu, Q. Su, and H. Wang, "A new approach to investigate Li₂MnO₃ and Li(Ni_{0.5}Mn_{0.3}Co_{0.2})O₂ mixed phase cathode materials," *J. Mater. Chem. A*, vol. 2, no. 7, pp. 2283–2289, 2014.
- [227] L. Xiao *et al.*, "Effects of structural defects on the electrochemical activation of Li₂MnO₃," *Nano Energy*, vol. 16, pp. 143–151, 2015.
- [228] M. Hirayama, K. Suzuki, R. Kanno, S. Taminato, K. Hikima, and S. Yasuno, "Thin film all-solid-state battery using Li₂MnO₃ epitaxial film electrode," *Chem. Lett.*, vol. 48, no. 5, pp. 192–195, 2019.

- [229] R. Saroha, A. Gupta, and A. K. Panwar, "Electrochemical performances of Li-rich layered-layered $\text{Li}_2\text{MnO}_3\text{-LiMnO}_2$ solid solutions as cathode material for lithium-ion batteries," *J. Alloys Compd.*, vol. 696, pp. 580–589, 2017.
- [230] J. Pires *et al.*, "Role of propane sultone as an additive to improve the performance of a lithium-rich cathode material at a high potential," *RSC Adv.*, vol. 5, no. 52, pp. 42088–42094, 2015.
- [231] Q. Zhang, T. Peng, D. Zhan, and X. Hu, "Synthesis and electrochemical property of $x\text{Li}_2\text{MnO}_3\cdot(1-x)\text{LiMnO}_2$ composite cathode materials derived from partially reduced Li_2MnO_3 ," *J. Power Sources*, vol. 250, pp. 40–49, 2014.
- [232] J. Lim *et al.*, "Fully activated Li_2MnO_3 nanoparticles by oxidation reaction," *J. Mater. Chem.*, vol. 22, no. 23, p. 11772, 2012.
- [233] F. Ning, H. Shang, B. Li, N. Jiang, R. Zou, and D. Xia, "Surface thermodynamic stability of Li-rich Li_2MnO_3 : Effect of defective graphene," *Energy Storage Mater.*, no. October 2018, pp. 1–7, 2019.
- [234] L. Xiong, M. Sun, Y. Xu, X. Du, and X. Xiao, "Synthesis of carbon coated Li_2MnO_3 cathode material with enhanced rate capability for lithium-ion batteries," *Solid State Ionics*, vol. 325, no. May, pp. 170–175, 2018.
- [235] R. Koerver *et al.*, "Chemo-mechanical expansion of lithium electrode materials-on the route to mechanically optimized all-solid-state batteries," *Energy Environ. Sci.*, vol. 11, no. 8, pp. 2142–2158, 2018.
- [236] N. Meethong, H. Y. S. Huang, S. A. Speakman, W. C. Carter, and Y. M. Chiang, "Strain accommodation during phase transformations in olivine-based cathodes as a materials selection criterion for high-power rechargeable batteries," *Adv. Funct. Mater.*, vol. 17, no. 7, pp. 1115–1123, 2007.
- [237] Y. Yang, X. Z. Liao, Z. F. Ma, B. F. Wang, L. He, and Y. S. He, "Superior high-rate cycling performance of $\text{LiFePO}_4/\text{C-PPy}$ composite at 55 °C," *Electrochem. commun.*, vol. 11, no. 6, pp. 1277–1280, 2009.
- [238] X.-Z. Liao, Z.-F. Ma, Y.-S. He, X.-M. Zhang, L. Wang, and Y. Jiang, "Electrochemical Behavior of LiFePO_4/C Cathode Material for Rechargeable Lithium Batteries," *J. Electrochem. Soc.*, vol. 152, no. 10, p. A1969, 2005.

- [239] G. Du, Y. Zhou, X. Tian, G. Wu, Y. Xi, and S. Zhao, "High-performance 3D directional porous LiFePO₄/C materials synthesized by freeze casting," *Appl. Surf. Sci.*, vol. 453, no. January, pp. 493–501, 2018.
- [240] A. Jiang *et al.*, "Enhancement of electrochemical properties of niobium-doped LiFePO₄/C synthesized by sol–gel method," *J. Chinese Chem. Soc.*, vol. 65, no. 8, pp. 977–981, 2018.
- [241] J. Ahn, S. Yoon, S. G. Jung, J. H. Yim, and K. Y. Cho, "A conductive thin layer on prepared positive electrodes by vapour reaction printing for high-performance lithium-ion batteries," *J. Mater. Chem. A*, vol. 5, no. 40, pp. 21214–21222, 2017.
- [242] Y. F. Zhao, B. Lu, and J. Zhang, "Lithium Diffusion and Stress in a Polycrystalline Film Electrode," *Acta Mech. Solida Sin.*, vol. 31, no. 3, pp. 290–309, 2018.
- [243] J. Huang, J. L. MacManus-Driscoll, and H. Wang, "New epitaxy paradigm in epitaxial self-assembled oxide vertically aligned nanocomposite thin films," *J. Mater. Res.*, vol. 32, no. 21, pp. 4054–4066, 2017.
- [244] J. Huang *et al.*, "Enhanced Flux Pinning Properties of YBCO Thin Films with Various Pinning Landscapes," *IEEE Trans. Appl. Supercond.*, vol. 27, no. 4, 2017.
- [245] J. Jian *et al.*, "Continuous Tuning of Phase Transition Temperature in VO₂ Thin Films on c-Cut Sapphire Substrates via Strain Variation," *ACS Appl. Mater. Interfaces*, vol. 9, no. 6, pp. 5319–5327, 2017.
- [246] M. Fan *et al.*, "Microstructure, Magnetic, and Magnetoresistance Properties of La_{0.7}Sr_{0.3}MnO₃:CuO Nanocomposite Thin Films," *ACS Appl. Mater. Interfaces*, vol. 10, no. 6, pp. 5779–5784, 2018.
- [247] J. Huang *et al.*, "Tailorable Optical Response of Au-LiNbO₃ Hybrid Metamaterial Thin Films for Optical Waveguide Applications," *Adv. Opt. Mater.*, vol. 1800510, pp. 1–9, 2018.
- [248] M. Lambert, A. May, C. K. Akkan, N. Agarwal, and O. C. Aktas, "Ag-Al₂O₃ optical nanocomposites with narrow particle size distribution prepared by pulsed laser deposition," *Mater. Lett.*, vol. 137, pp. 405–408, 2014.
- [249] L. Gonzalez-García, I. Gonzalez-Valls, M. Lira-Cantu, A. Barranco, and A. R. Gonzalez-Elipe, "Aligned TiO₂ nanocolumnar layers prepared by PVD-GLAD for transparent dye sensitized solar cells," *Energy Environ. Sci.*, vol. 4, no. 9, pp. 3426–3435, 2011.

- [250] Y. Gaillard, V. J. Rico, E. Jimenez-Pique, and A. R. González-Elipe, “Nanoindentation of TiO₂ thin films with different microstructures,” *J. Phys. D. Appl. Phys.*, vol. 42, no. 14, 2009.
- [251] W. C. Oliver and G. M. Pharr, “An improved technique for determining hardness and elastic modulus using load and displacement sensing indentation experiments,” *J. Mater. Res.*, vol. 7, no. 6, pp. 1564–1583, 1992.
- [252] Y. He, J. Fu, and Y. Zhao, “Oblique angle deposition and its applications in plasmonics,” *Front. Phys.*, vol. 9, no. 1, pp. 47–59, 2014.
- [253] Y. He and Y. Zhao, “Advanced multi-component nanostructures designed by dynamic shadowing growth,” *Nanoscale*, vol. 3, no. 6, pp. 2361–2375, 2011.
- [254] A. K. Kar *et al.*, “Epitaxial multilayered Co/Cu ferromagnetic nanocolumns grown by oblique angle deposition,” *Nanotechnology*, vol. 18, no. 29, 2007.
- [255] L. González-García, G. Lozano, A. Barranco, H. Míguez, and A. R. González-Elipe, “TiO₂-SiO₂ one-dimensional photonic crystals of controlled porosity by glancing angle physical vapour deposition,” *J. Mater. Chem.*, vol. 20, no. 31, pp. 6408–6412, 2010.
- [256] W. Smith and Y. P. Zhao, “Superior photocatalytic performance by vertically aligned core-shell TiO₂/WO₃ nanorod arrays,” *Catal. Commun.*, vol. 10, no. 7, pp. 1117–1121, 2009.
- [257] Y. He and Y. Zhao, “Improved hydrogen storage properties of a V decorated Mg nanoblade array,” *Phys. Chem. Chem. Phys.*, vol. 11, no. 2, pp. 255–258, 2009.
- [258] J. G. Fan and Y. P. Zhao, “Gold-coated nanorod arrays as highly sensitive substrates for surface-enhanced raman spectroscopy,” *Langmuir*, vol. 24, no. 24, pp. 14172–14175, 2008.
- [259] Y. He, Y. Zhao, and J. Wu, “The effect of Ti doping on the growth of Mg nanostructures by oblique angle codeposition,” *Appl. Phys. Lett.*, vol. 92, no. 6, pp. 1–4, 2008.
- [260] C. M. Zhou, H. F. Li, and D. Gall, “Multi-component nanostructure design by atomic shadowing,” *Thin Solid Films*, vol. 517, no. 3, pp. 1214–1218, 2008.
- [261] T. Matsunaga *et al.*, “Dependence of Structural Defects in Li₂MnO₃ on Synthesis Temperature,” *Chem. Mater.*, vol. 28, no. 12, pp. 4143–4150, 2016.
- [262] Y. Xie, Y. Jin, and L. Xiang, “Understanding Mn-Based Intercalation Cathodes from Thermodynamics and Kinetics,” *Crystals*, vol. 7, no. 221, pp. 1–22, 2017.

- [263] Z. Wang, T. Zhao, J. Yao, Y. Kishikawa, and M. Takei, "Evaluation of the Electrochemical Characterizations of Lithium-Ion Battery (LIB) Slurry with 10-Parameter Electrical Equivalent Circuit (EEC)," *J. Electrochem. Soc.*, vol. 164, no. 2, pp. A8–A17, 2017.
- [264] T. Osaka, D. Mukoyama, and H. Nara, "Review—Development of Diagnostic Process for Commercially Available Batteries, Especially Lithium Ion Battery, by Electrochemical Impedance Spectroscopy," *J. Electrochem. Soc.*, vol. 162, no. 14, pp. A2529–A2537, 2015.
- [265] B. H. Stafford *et al.*, "Tilted BaHfO₃ nanorod artificial pinning centres in REBCO films on inclined substrate deposited-MgO coated conductor templates," 2017.
- [266] Y. He, C. Brown, Y. He, J. Fan, C. A. Lundgren, and Y. Zhao, "Porous three-dimensional nanorod arrays through selective chemical etching of nanocomposites," *Chem. Commun.*, vol. 48, no. 62, pp. 7741–7743, 2012.
- [267] Y. He, C. Brown, C. A. Lundgren, and Y. Zhao, "The growth of CuSi composite nanorod arrays by oblique angle co-deposition, and their structural, electrical and optical properties," *Nanotechnology*, vol. 23, no. 36, 2012.
- [268] J. Jiang *et al.*, "General synthesis of large-scale arrays of one-dimensional nanostructured Co₃O₄ directly on heterogeneous substrates," *Cryst. Growth Des.*, vol. 10, no. 1, pp. 70–75, 2010.
- [269] Umm-e-Farwa, K. S. Ahmad, Z. Hussain, and S. Majid, "Synthesis, characterization and PVD assisted thin film fabrication of the nano-structured bimetallic Ni₃S₂/MnS₂ composite," *Surfaces and Interfaces*, vol. 12, no. October 2017, pp. 190–195, 2018.
- [270] B. J. Hwang, C. Y. Wang, M. Y. Cheng, and R. Santhanam, "Structure, morphology, and electrochemical investigation of LiMn₂O₄ thin film cathodes deposited by radio frequency sputtering for lithium microbatteries," *J. Phys. Chem. C*, vol. 113, no. 26, pp. 11373–11380, 2009.
- [271] H. Otsuji, K. Kawahara, T. Ikegami, and K. Ebihara, "LiMn₂O₄ thin films prepared by pulsed laser deposition for rechargeable batteries," *Thin Solid Films*, vol. 506–507, pp. 120–122, 2006.

- [272] Y. Zeng, G. Gao, G. Wu, and H. Yang, “Nanosheet-structured vanadium pentoxide thin film as a carbon- and binder-free cathode for lithium-ion battery applications,” *J. Solid State Electrochem.*, vol. 19, no. 11, pp. 3319–3328, 2015.
- [273] J. D. Perkins, C. S. Bahn, J. M. McGraw, P. A. Parilla, and D. S. Ginley, “Pulsed Laser Deposition and Characterization of Crystalline Lithium Cobalt Dioxide (LiCoO₂) Thin Films,” *J. Electrochem. Soc.*, vol. 148, no. 12, p. A1302, 2002.
- [274] A. Chen, Q. Su, H. Han, E. Enriquez, and Q. Jia, “Metal Oxide Nanocomposites: A Perspective from Strain, Defect, and Interface,” *Adv. Mater.*, vol. 1803241, pp. 1–30, 2018.
- [275] W. Zhang, A. Chen, Z. Bi, Q. Jia, J. L. Macmanus-Driscoll, and H. Wang, “Interfacial coupling in heteroepitaxial vertically aligned nanocomposite thin films: From lateral to vertical control,” *Curr. Opin. Solid State Mater. Sci.*, vol. 18, no. 1, pp. 6–18, 2014.
- [276] Y. Gogotsi and R. M. Penner, “Energy Storage in Nanomaterials – Capacitive, Pseudocapacitive, or Battery-like?,” *ACS Nano*, vol. 12, no. 3, pp. 2081–2083, 2018.
- [277] V. Augustyn *et al.*, “High-rate electrochemical energy storage through Li⁺ intercalation pseudocapacitance,” *Nat. Mater.*, vol. 12, no. 6, pp. 518–522, 2013.